ELECTRODEPOSITED CUPROUS OXIDE SOLAR CELLS

by

KUNHEE HAN

Presented to the Faculty of the Graduate School of

The University of Texas at Arlington in Partial Fulfillment

of the Requirements

for the Degree of

DOCTOR OF PHILOSOPHY

THE UNIVERSITY OF TEXAS AT ARLINGTON

December 2009

ACKNOWLEDGEMENTS

I am really honored to have this opportunity to express my sincere appreciation to all of the people who have supported me during my Ph.D. study.

First and foremost, I would like to express my deepest gratitude to my advisor, Prof. Meng Tao, for his support, guidance, and encouragement throughout my Ph.D. work. Without his support, this research would not have been completed. What I have learned from him as a researcher and a person will lead me in becoming a capable researcher, as well as a good human being. I am also very grateful to my committee members, Prof. Weidong Zhou, Prof. Michael Jin, Prof. Michael Vasilyev, and Prof. W. Alan Davis, for their valuable suggestions, advices, and comments throughout my research.

I also want to express special thanks to past and current group members, Guanghua, Yusuf, Longcheng, Xialong, Jinggang, Jana, Guilhem, Ying, Xiaofei, Amit, and Bin, for their friendship and help in my research. Also, I would like to thank all of my dear friends whom I have met at the University of Texas at Arlington: Daewoo, Sangseok, Woonki, Youngsik, Donyun, Youngho, Jungho, Kihoon, Kungseo, Jiyong, Jonggwhan, Kihyun, Bohoon, Hyunjoo, Hyunwook, Soo, Jason, Charles, Sharia, Hongjun and Li. I am grateful for their encouragement and friendship. I also wish to acknowledge Prof. Dongchan Shin and Prof. Donggun Lim for their valuable discussion of and support in my research work. I would like to express my appreciation to the Nano-Fab staff: Nasir, Dennis, Eduardo, Chris and Fatima. I thank them for their assistance in my experimental setup and for my training in the use of various types of equipment.

My special thanks go to Mr. Ron Haker and Mrs. Jan Haker, who baptized me and introduced a different perspective of being a dedicated believer. They have always stood beside me as my parents, friends and spiritual mentors. The Christian attitude which I learned from

them changed the philosophy of my life. The Bible classes we have had together will remain in my heart as my best memory in Texas.

I would like to thank my family. My dearest wife, Boyeong has always been beside me, offering her love, sacrifice and support with great patience. I owe her more than I could ever return. It has been a great pleasure to see my son, Nathan grow up during the progress of this research. His big smile and his love have encouraged me through all of the times when I was exhausted. My parents, Dongpil and Jongbok deserve to have more thanks than anyone. With patience and understanding, they have always taken care of and believed in me. Without their consistent support and love, it would have been impossible for me to achieve my goals in research. I also would like to express special thanks to my parents-in-law, chunki and eunhee for their love and prayers.

Finally, I would like to thank my Lord Jesus Christ who always stands by me, loves me, and raises me to more than I can be.

This research has been supported by the National Science Foundation under Grant no. 0620319.

November 23, 2009

ABSTRACT

ELECTRODEPOSITED CUPROUS OXIDE

SOLAR CELLS

Kunhee Han, PhD

The University of Texas at Arlington, 2009

Supervising Professor: Meng Tao

The electrochemically deposited cuprous oxide (Cu_2O) as a photovoltaic absorber material is introduced in this work.

The electrical, structural, and optical characteristics of electrodeposited Cu_2O are well investigated. The pH of the deposition solution controls the flat band voltage of Cu_2O. The variation of the flat band voltage by solution pH is related to oxygen incorporation in the film, which is controlled by the amount of oxygen precursor, OH^-, in the solution. Hence, the high pH in the solution is preferable for producing a p-type Cu_2O with copper vacancy, while the low pH in the solution is preferable for producing an n-type Cu_2O with oxygen vacancy or copper interstitial. The resistivity of Cu_2O is controlled by the deposition solution pH. As the pH of a solution increases, the resistivity of Cu_2O decreases. The crystal orientation and the grain size have significant roles in controlling the resistivity of p-type Cu_2O. Cu_2O with a crystal orientation of (111) shows lower resistivity than Cu_2O with a crystal orientation of (100). A possible reason for this is that Cu_2O with (111) orientation grows in the solution of high pH, and it leads to a

more intrinsic point defect, i.e, Cu vacancies that determine the carrier concentration in the film. Electrodeposited Cu_2O shows a direct band gap of ~2.06 eV, which is independent of the deposition condition.

Cu_2O p-n homojunction solar cells with two different structures are successfully fabricated by a two-step electrodeposition method. The highest efficiency of 0.15% is achieved in an electrodeposited Cu_2O substrate solar cell. The solution bath pH of n-Cu_2O controls the open circuit voltage of the device. Several pin holes which were observed in the device contribute to the formation of shunt paths and cause the degradation of solar cell performance in the large superstrate solar cells. The thermal reliability test indicates that the device performance of the Cu_2O solar cell is not stable above the temperature of 150 ^oC. The Cu_2O superstrate solar cell exhibits better device performance than the Cu_2O substrate cell. The thickness of the p-Cu_2O layer influences the open circuit voltage of superstrate cells. Low efficiency of Cu_2O solar cells is mainly influenced by the high resistivity of both the p and the n-Cu_2O.

In order to control the electrical properties of Cu_2O, two different n-type doping techniques, thermal diffusion doping and electro doping, are introduced. The resistivity of Cu_2O is successfully controlled by Cu thermal diffusion. Also, the Fermi energy of Cu_2O is shifted and the n type property of Cu_2O is enhanced by Cu diffusion. This confirms that the intrinsic point defects in Cu_2O, such as copper vacancy and oxygen vacancy, are controlled by external copper diffusion. It is speculated that Cu diffusion in Cu_2O takes place mainly along grain boundaries (100) at the beginning of the annealing process, and then lattice diffusion follows along the (111) planes, due to its lower lattice distortion. N type electrodoping in Cu_2O is successfully achieved with Br ion. Br concentration plays a significant role in the crystal growth. The formation of a dendritic crystal of Cu_2O is caused by Br in the solution. It is believed that the mechanism of electrodoping is the co-deposition of the n-type dopant with Cu_2O.

TABLE OF CONTENTS

LIST OF ILLUSTRATIONS

LIST OF TABLES

CHAPTER 1

INTRODUCTION

1.1 World Energy Consumption

Energy is essential in order to maintain human society and to continue the development of planet Earth. Humans have relied mostly on fossil fuel for energy since the beginning of the civilized world. It was reported that the energy level of 15.8 TW was consumed globally in 2006 [1] and over 85 % of the total energy consumption was from fossil fuels such as oil, coal, and gas. This consumption is illustrated in Figure 1.1 [2].

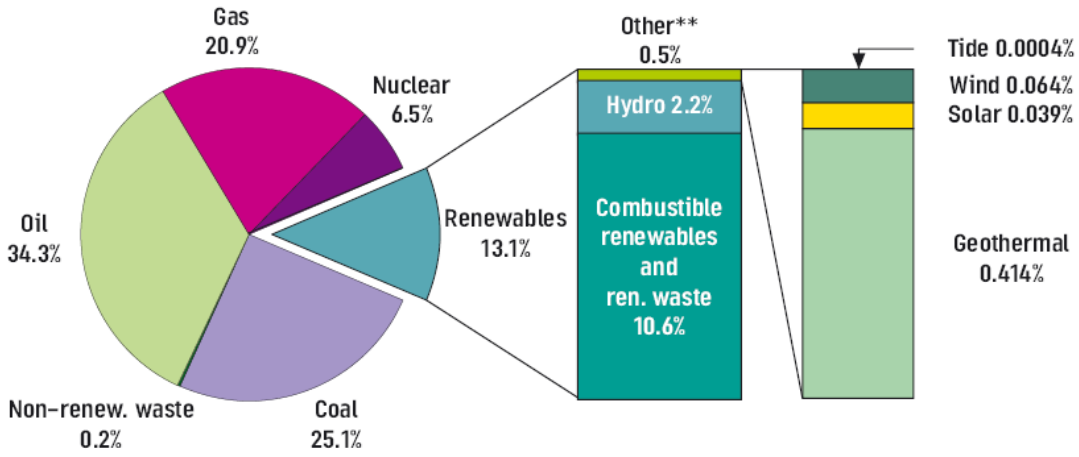

Figure1.1 2004 fuel shares of world total primary energy supply

It is expected that the global energy demand will increase to approximately 25 TW by 2030 [3]. The problem is that the reserves of fossil fuels are limited, and all fossil fuel will be depleted in the near future if the usage of this primary energy supply remains at its current level. Another concern in the use of fossil fuel is the environmental issue of carbon dioxide emission, produced by the combustion of fossil fuel. Carbon dioxide is known as one of the air pollutants and a producer of green house effect gases. The carbon dioxide emission increased from the

pre-industrial value of 280 ppm to 379 ppm in 2005 [4]. It is expected that the concentration of CO_2 will reach the value of 750 ppm by 2050, assuming the current fossil fuel usage rate remains constant in the future [5]. Hence, considerable attention has been paid to green energy, which uses renewable energy resources such as wind, biomass, solar, wave, and geothermal. Renewable energy makes it possible, not only to secure vital energy supplies, but also to keep the planet clean for the next generations.

1.2 Solar Energy

Solar energy is considered to be one of the most sustainable energy resources for future energy supplies. It has a huge potential capacity of approximately 120.000 TW, which is about 8000 times larger than the current energy consumption per year. The capacities of other renewable energy resources are limited to less than 1000 TW per year. This means that the energy the earth receives from the sun in one hour is almost the same as the total energy used for an entire year [6]. This indicates that solar energy will be the best candidate for future energy supplies in terms of potential capacity.

Basically, solar energy can be used in three different ways. First, solar energy can be converted to electricity by photo-induced charge carriers, electron and hole pairs, in semiconductor and a dye. Second, solar energy is used through the photosynthetic process to obtain solar fuels, such as liquid ethanol and hydrogen, by transfer of excited electron and hole pairs to biological or chemical molecules. The natural photosynthesis in plants produces fuel in the form of sugar and other carbohydrates, and plants themselves can be used as biomass for conversion to secondary fuels such as liquid ethanol and methane. Also, to produce fuel in the form of hydrogen, water can be split by the photosynthetic process with artificial molecular assembly. Third, solar radiation can be converted to heat energy. Sunlight over a large area can be focused to a line or spot by solar concentrators, and this absorber line or spot can be heat up as high as 3000 ^{o}C. This heat energy is transferred to a thermal storage medium, such as water, for space heating. While there are several ways to use solar energy to produce

electricity, fuel and heat, fossil fuel is a still primary resource for energy. Fossil fuels are still chosen for cost, reliability, and performance reasons at the market. In this research, solar electricity generated by light-induced voltage, i.e. photovoltaic (PV) effect will be explored.

1.3 Current PV Device Market

The current PV cell and module market is mainly based on 1st generation Si-based cells, such as single crystal and poly crystalline Si cells, which comprise around 85% of all the world's PV modules market. Although 2nd generation PV cells (thin film cells) have great advantages, such as their ease of manufacturability over large areas and less material usage, their current market share, which is listed in Table 1.1, is still much smaller than Si-based cells [7]. It is expected that single crystal and poly crystalline Si cells will continue to dominate the PV market for several more years due to their higher conversion efficiency and better durability [7].

Table 1.1 2004 world PV cell production by cell technology (MW)

Technique	US	Japan	Europe	Rest of world	Total	%
S.C & P.C Si-Wafer	99.7	504.5	273.8	133.1	1011.1	84.64
Amorphous Si	14	77.5	8.6	7.0	107.1	8.9
Ribbon Si	16	0	25	0	41	3.4
M.C Si	0	20	0	0	20	1.7
CdTe	6	0	7	0	13	1.1
CIGS	3	0	0	0	3	0.25
Total	138.7	602	314.4	140.1	1195.2	100

1.4 Cost and Material Issues in Current Solar Cells

The lowest price of Si based solar modules is approximately \$2.50/W_p today, and the price of solar electricity is approximately \$0.20/kWh, which is about four times higher than electricity from fossil fuels [8]. The high solar electricity cost is still the biggest obstacle to solar cell becoming a main energy source for individual household. In contrast with the CMOS-based semiconductor industry, a large quantity of Si material is required in the solar industry. Basically, the high price of solar electricity is caused by material cost, which is about 50% of the overall

cost of the Si-wafer module. It is hard to lower the price of the Si-wafer because several Si-wafer processes, such as the Siemens process, the Czochralski ingot growth process and the wafer slicing process, usually consume excessive energy [9].

In addition to cost issues, Si is not a perfect material for the PV device from the solid state physics point of view because of its indirect energy band gap and its low absorption coefficient. Hence, it is necessary to find a cheap, abundant and easily processed material instead of Si and to develop a low cost process suitable for large scale production in order to lower solar electricity cost.

Ideal solar cell efficiency depends on the energy band-gap of a semiconductor as shown in Figure 1.2 [10].

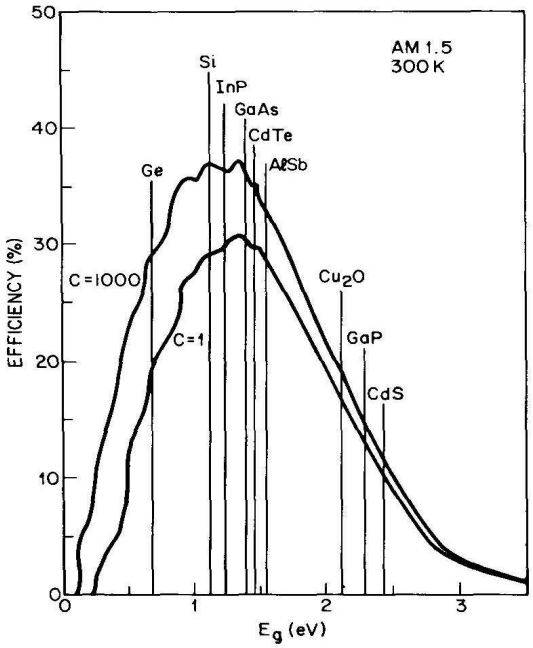

Figure 1.2 Ideal solar cell efficiency depending on energy band-gap of semiconductor

Basic requirements for the ideal solar cell material are listed below [11].

1. Band gap between 1.1 and 1.7eV
2. Direct band structure

3. Readily available and non-toxic materials
4. Easy, reproducible deposition technique, suitable for large area production
5. Good photovoltaic conversion efficiency
6. Long-term stability

1.5 Research Objective

The high cost of silicon solar cells forces the development of new photovoltaic devices utilizing cheap and non-toxic materials prepared by energy-efficient processes. Cuprous oxide (Cu_2O) has attracted attention for solar cell applications due to its direct band gap around 2 eV and its high absorption coefficient, combined with material abundance, non-toxicity and low-cost fabrication [12,13]. However, poor understanding about intrinsic point defects, difficulty in doping and absence of n-type Cu_2O have impeded the development of Cu_2O-based solar cells. Over the past three decades, Cu_2O-based solar cells have been fabricated with metal/Cu_2O Schoktty junctions and p-n heterojunctions such as, n-CdO/p-Cu_2O [14], n-ZnO/p-Cu_2O [15] and n-ITO/p-Cu_2O [16]. The highest conversion efficiency with Cu_2O as the active layer is around 2 % with a p-n heterojunction structure [16], while the theoretical efficiency for Cu_2O solar cells is about 19 % [17]. It is generally accepted that a p-n homojunction of Cu_2O is the best way to increase the efficiency of Cu_2O-based solar cells [18]. The objectives of this research are listed as follows:

1. Study electrical, structural, and optical properties of electro-deposited Cu_2O
2. Fabrication and characterization of electrochemically deposited p-n homojunction Cu_2O solar cell
3. Doping into Cu_2O to improve electrical properties of Cu_2O

CHAPTER 2

BACKGROUND

2.1 Solar Cell

2.1.1 History of Solar Cells

Solar cells are electronic devices which convert photon energy from the sunlight to electricity. The conversion process is made possible by the photovoltaic effect, i.e. light induced voltage, which was first discovered by French physicist Becquerel in 1839, as he observed a voltage between electrodes in an electrochemical cell when it was illuminated [19]. The first solar cells were demonstrated by Fritts in 1883 using Se semiconductor covered with a thin Au layer [20]. Over the next sixty years, despite continuous effort to develop solar devices with different materials including copper-cuprous oxide [21], selenium and thallous sulfide, solar cell efficiency remained at less than 1 % until revolutionary Si-technology emerged in the 1950s. The practical solar cells with efficiency of ~6 % were developed in 1954 by Chapin, Fuller and Pearson at Bell laboratories [22] and their single-crystal Si based solar cells have been the basis of the photovoltaic device until now.

2.1.2 Working Principles of Solar Cells

Solar energy is emitted primarily as electromagnetic radiation, i.e. light, which frequency lies between the ultraviolet and the radio spectral regions, 0.2 to 3 um. The main spectrum region of solar radiation is in the visible wavelength region which is illustrated in Figure 2.1 [23].

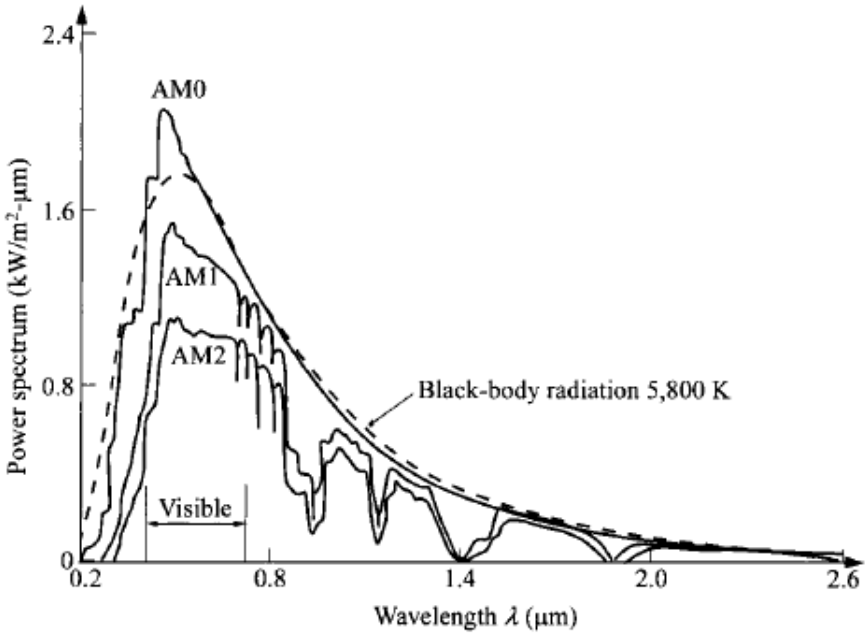

Figure 2.1 Solar spectrums at different air-mass condition

When the semiconductor is exposed to the light, i.e. photons, three unique optical phenomenons happen in the semiconductor. First, photons are not absorbed in the semiconductor and just pass through the semiconductor. This occurs if the photons have energy lower than the energy band gap (E_g) of the semiconductor, as in the case of 3 in Figure 2.2. Second, some of the photons are reflected from the surface of the semiconductor, depending on the incident angle of the photon and the surface structure of the semiconductor. In both of the above cases, there is no contribution to the generation of power in the solar cells. Third, some photons are absorbed in the semiconductor if the photons have energy greater than E_g of the semiconductor. The excess photon energy, the difference between photon energy and E_g of semiconductor, is wasted as heat through excitation of the lattice vibration, and the photon energy just greater than E_g generates electron-hole pairs in the semiconductor, as in case 1 and 2 respectively in Figure 2.2.

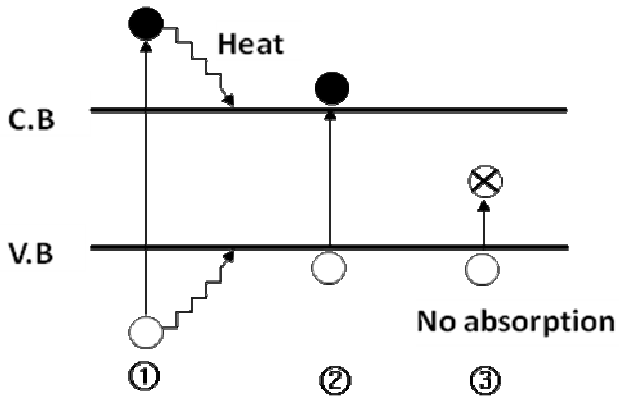

Figure 2.2 Photon absorption in a semiconductor

Interestingly, the region of the semiconductor where a photon is absorbed is dependent on the photon's wavelength. The shorter wavelength photon is absorbed in a region closer to the surface and the longer wavelength photon is absorbed in a region further away from the surface, which is illustrated in Figure 2.3. Overall, average photon absorption is the highest in the region close to the surface. The degree to which photons are absorbed in the semiconductor is related to the optical properties of the semiconductor, such as the energy band structure. The indirect band gap semiconductor like Si basically has a smaller absorption coefficient than a direct band gap semiconductor like GaAs. This means Si needs to be much thicker than GaAs in order to absorb the same amount of photons that can be absorbed in GaAs.

Practically, all conventional photovoltaic devices are based on the p-n junction. A schematic of the cross-section of a conventional p-n junction solar cell and its energy-band diagram are shown in Figure 2.3 and 2.4, respectively. Most of charge carriers, i.e. electron-hole pairs, are generated in the region close to the solar cell surface, where photon absorption is the highest. The charge carriers can be easily separated by two transport mechanisms. One is drift, induced by internal electric field in the depletion region and the other one is diffusion by carrier concentration gradient. It is more favorable to position internal electric field, which acts in role of charge carriers separation, closer to the surface rather than the bulk in order to enable a

high collection probability of charge carriers, i.e., reduce charge carriers recombination. Then, the charge carriers are finally collected at the corresponding metal contacts by diffusion.

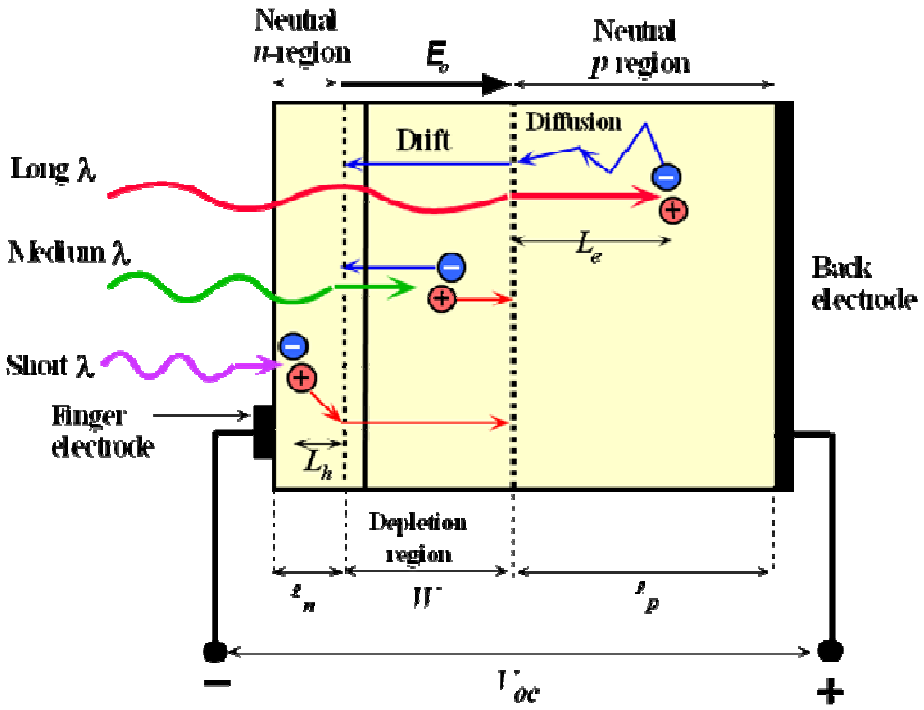

Figure 2.3 A schematic of cross-section of a conventional solar cell

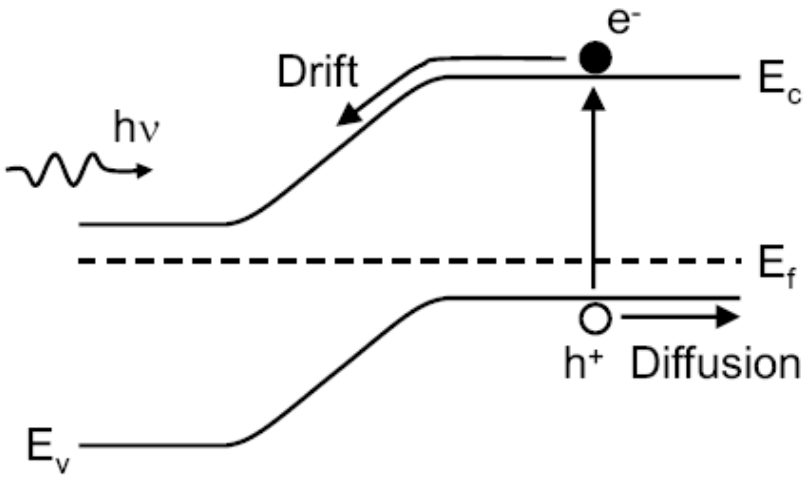

Figure 2.4 Energy-band diagram of p-n junction solar cell.

2.1.3 Important Parameters in the Solar Cells

The ideal (a) and practical (b) equivalent circuits of a solar cell are illustrated in Figure 2.5. The I-V characteristic of output load in Figure 2.5 (a) is given by

$$I = I_S \left\{ \exp\left[\frac{qV}{nkT} \right] - 1 \right\} - I_{ph} \tag{2.1}$$

where I_{ph} is the photo current which results from the excited charge carriers by light illumination, I_S is the diode saturation current, n is the diode ideality factor and k is the Boltzmann's constant. In the practical case, the I-V characteristic of output load in Figure 2.5 (b) is given by

$$I = I_S \left\{ \exp\left[\frac{q(V - IR_s)}{nkT} \right] - 1 \right\} - I_{ph} + \frac{V - IR_s}{R_{sh}} \tag{2.2}$$

where R_s and R_{sh} are the series resistance and shunt resistance in the solar cell, respectively.

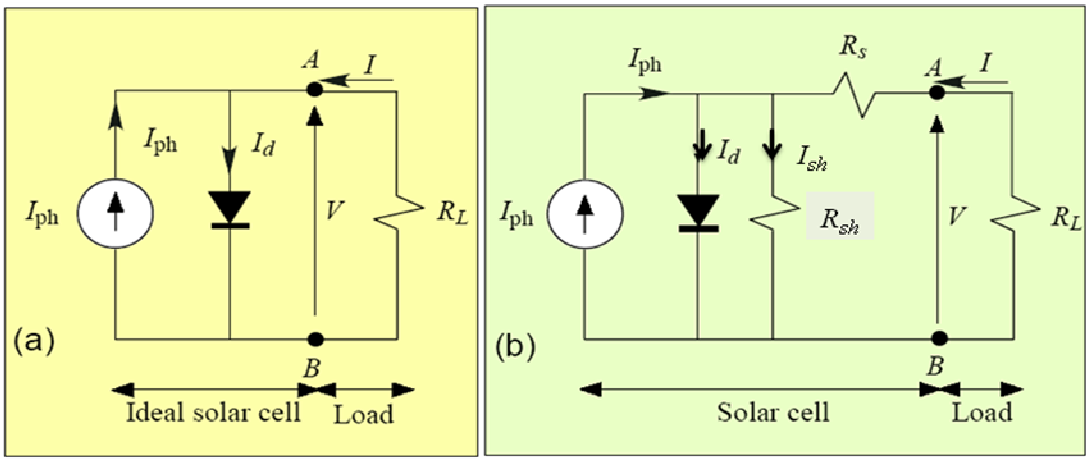

Figure 2.5 The equivalent circuit of a solar cell in (a) ideal case and (b) practical case with series resistance (R_s) and shunt resistance (R_{sh}).

The typical I-V characteristic of solar cell under illumination is shown in Figure 2.6. The performance of this device can be simply demonstrated by a few solar cell parameters including short-circuit current (I_{sc}), open-circuit voltage (V_{oc}), fill factor (FF), and conversion efficiency (η).

The ideal short circuit current I_{SC}, i.e. I_{ph} is generated by light with many different wavelengths. Hence, the total photo-generated current can be obtained by integrating the

contributions of photons to the current from excitation at each wavelength. The ideal short-circuit photocurrent, I_{sc}, is given by

$$I_L = qA \int_{E=E_g}^{\infty} I_S(E) \cdot QY(E) dE \tag{2.3}$$

where q is electron's charge, A is the active surface area of solar cell, I_S is the solar photon flux, QY the quantum yield, and E is the photon energy [17]. The short-circuit current can be experimentally obtained by shorting two terminals of load. The short-circuit current is usually lower than photo-generated current, I_{ph}, due to series resistance caused by the bulk resistance of the semiconductor and by the contact resistance between the semiconductor and metal. The low shunt resistance caused by poor formation of the p-n junction decrease I_{sc} as well.

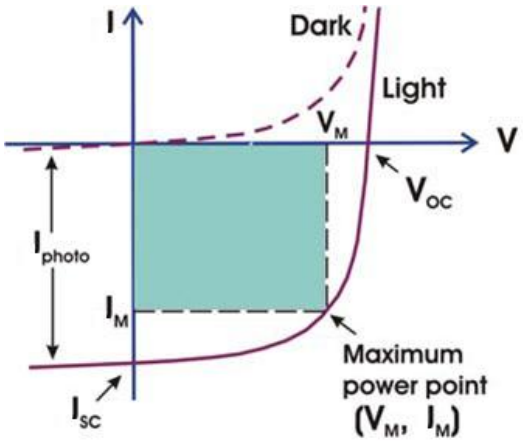

Figure 2.6 Current- voltage characteristic of a solar cell under illumination

When a cell is operated in open-circuit, i.e. load in Figure 2.5 is open, there is no current flow in the circuit. The voltage between two terminals of load is called open-circuit voltage, V_{OC}. In the case of ideal device, V_{OC} can be expressed by setting I = 0 in Equation 2.1 to

$$V_{OC} = \frac{kT}{q} \ln\left(\frac{I_{ph}}{I_S} + 1\right) \tag{2.4}$$

By reducing the saturation current, I_S, in the p-n junction, open-circuit voltage can be increased.

Another term defining the overall performance of the solar cell is the fill factor, the ratio of the maximum power of the cell to the product of I_{SC} and V_{OC}, given by

$$FF = \frac{I_M V_M}{I_{SC} V_{OC}} \tag{2.5}$$

where I_M and V_M are the current and voltage corresponding to the maximum output power P_M under illumination, which is the rectangle area shown in Figure 2.6. The maximum FF value is limited to 0.83 by the diode equation itself, and it is also directly affected by series and shunt resistance in the cell. It is necessary to have low series resistance and high shunt resistance in order for solar cell to have a higher FF, i.e., efficiency [10].

Finally, the conversion efficiency η is defined by

$$\eta = \frac{I_M \cdot V_M}{P_{in}} = \frac{FF \cdot I_{SC} \cdot V_{OC}}{P_{in}} \tag{2.6}$$

$$P_{in} = \int_0^\infty P(\lambda) d\lambda \tag{2.7}$$

where P_{in} is the power of the incident light and P(λ) is the solar power density at wavelength λ and measured in standard test conditions (STC) which represents a temperature of 25 ºC and an irradiance of 1000 W/m^2 with an air mass 1.5 (AM1.5) spectrums.

2.1.4 Theoretical Scheme for High Efficiency

In this part, the theoretical scheme to increase device efficiency will be briefly discussed with four different physics point of view.

First, more photon absorption is advantageous in generating more charge carriers, which contribute to increased photo-current. Usually, light loss (reflectance) takes place on the surface of solar cell devices, corresponding to part 1 and 2 in Figure 2.7. It can be reduced by applying an antireflective coating with proper refractive index on the top surface of the solar cells [24], by texturizing a device surface with assistance of wet and dry etching [25], and by

designing efficient top electrode to minimize the shadow effect by itself. Another way to increase photon absorption is to increase photon reflection from the bottom electrode by using a back reflector [26].

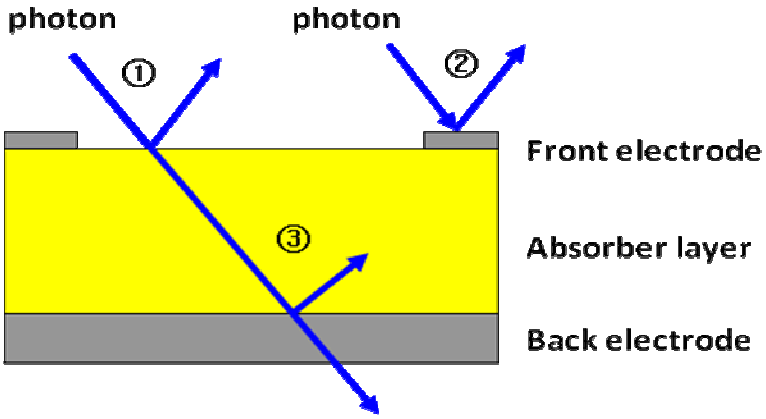

Figure 2.7 light absorption and loss in the solar cell

Second, it is always beneficial to absorb all photon energy with different wave lengths in order to more efficiently generate charge carriers. As mentioned in 2.1.2, the excess photon energy, the difference between photon energy and E_g of a semiconductor, is wasted as heat, and the photon with energy less than E_g is not absorbed. The excess photon energy loss can be reduced by multiple junctions composed of semiconductors with different energy band-gaps [27] and by hot carrier extraction before its relaxation to conduction band [28]. By placing an intermediate energy state induced by impurity into the middle of an energy band-gap, a photon with energy less than E_g can be absorbed and can contribute to generate charge carriers [29].

Third, more efficient charge separation without recombination is key to the increase in efficiency of the solar cell. Usually, the semiconductor's surface and the grain boundary (GB) have a higher energy state than bulk, and these places act as recombination centers for charge carriers. The probability of electron-hole recombination can be reduced by surface passivation and GB etching [30].

Fourth, more efficient carrier harvest can be achieved by reducing series resistance and increasing parallel resistance in the solar cell. Contact resistance, one of series resistance factors, between the metal and the absorber layer can be reduced by proper metallization and metal firing processes. Also, the parallel resistance in a solar cell can be increased by proper edge cutting processes, usually done by laser in industry.

2.2 Electrochemical Deposition Method for Semiconductors

An Electrodeposition is well known for depositing metals and metallic alloys at the industrial level, such as Zn electroplating for surface treatment, Cu interconnect deposition on electronic chips, and Ni-Fe alloy for magnetic heads. However, an electrodeposition of a semiconductor is still an open challenge. Semiconducting properties are much more difficult to obtain than metallic properties since they control minority carriers at the ppm level, which is a priori much more difficult to achieve from solution processes than from vacuum ones. Nevertheless researches have been devoted for long time to apply electrodeposition to the synthesis of semiconductors such as CdTe [31-34], CIGS [35-37], and other metal oxide [38-42] because of its unique advantages of low cost, low temperature, easy control over parameters, and large area deposition.

An electro-deposition is carried out by passing an electric current between two or more electrodes separated by an electrolyte. This deposition takes place at the electrode-electrolyte interface, which has the electrical double layer with a high potential gradient of 10^5 Vcm^{-1}. In general, the overall electrochemical reaction taking place in a cell is composed of two independent half-reactions. Each half-reaction responds to the interfacial potential difference at the corresponding electrode. Most of the time, one is interested in only one of these reactions, and the electrode at which it occurs is called the working electrode (WE). To focus on it, the other half of the cell is standardized by using an electrode made up of phases having essentially constant composition, which is called the reference electrode (RE) [43].

The internationally accepted primary reference electrode is the standard hydrogen electrode (SHE) or normal hydrogen electrode (NHE) composed of $Pt/H_2/H^+$ (aqueous). However, in the scientific experiment, the saturated calomel electrode, $Hg/Hg_2Cl_2/KCl$ (saturated in water) and the silver-silver chloride electrode, Ag/AgCl//KCl (saturated in water) are commonly used as reference electrodes due to SHE's inconvenience in experimental applications. Since the reference electrode has a constant makeup, its potential is fixed. Hence, any potential changes in the cell can be described by the working electrode.

Fig. 2.8 shows how electrochemical reactions are carried out by the potential applied to the working electrode. By applying negative voltage to the working electrode, the energy of the electron in the working electrode is raised. When the energy of the electron in the working electrode is higher than the vacant electronic energy states on species in the electrolyte, an electron in the working electrode moves into the electrolyte. Hence, the cathodic current will be generated, and it will cause the reduction of the species in the solution at the surface of the working electrode. Similarly, the energy of the electron in the working electrode is lowered by applying positive voltage to the working electrode. When the energy of the electron in the working-electrode is lower than the occupied electronic energy states on species in the electrolyte, an electron in solution species moves into the electrode. Hence, the anodic current will be generated, and it will cause the oxidation of the species in the solution. The critical potential, at which these processes take place, is called the standard potential (E_0) for the related species in the solution.

The key of an electrochemical reaction is a proper choice of a number of reaction parameters shown in Figure 2.9. It should be noted that an electrode reaction will not be only controlled by a single parameter but by many other factors, which lead a large number of trials to optimize the process, keeping in view the product quality.

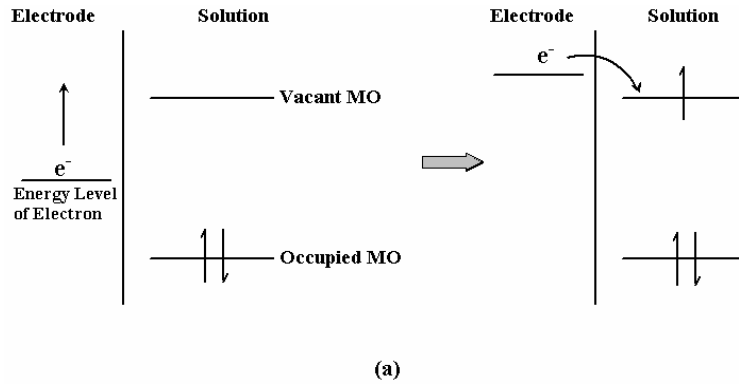

Figure 2.8 Representation of (a) reduction and (b) oxidation process of a species in solution [43]

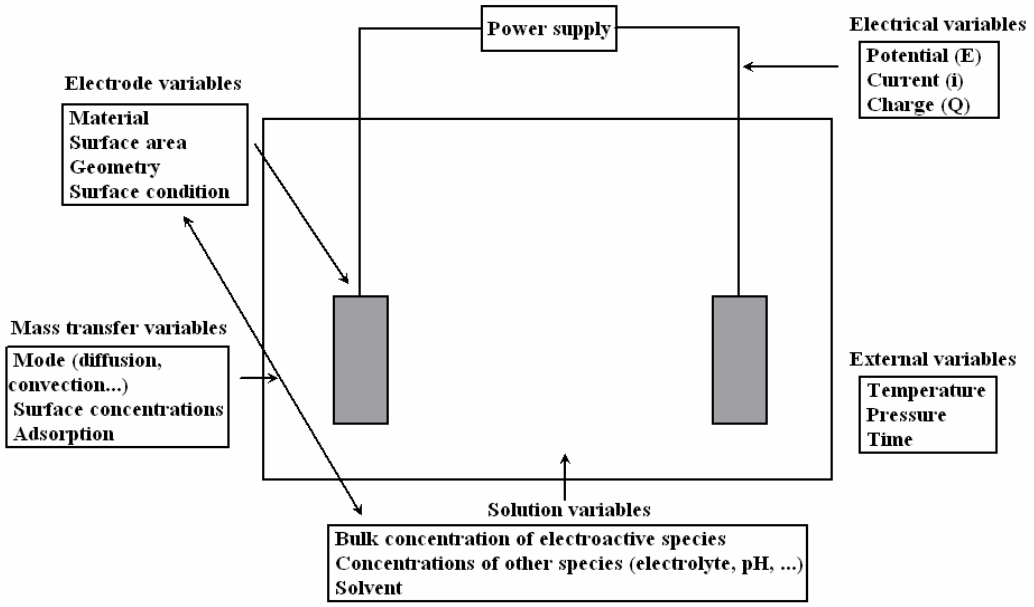

Figure 2.9 Electrodeposition process variables affecting the rate of an electrode reaction [43]

In a typical electrodeposition, the reactant, which is dissolved in the electrolyte, is deposited as a solid product. Consequently, the activity of the reactant decreases as the reaction proceeds. The two important parameters to determine the route of electrochemical reaction are the deposition current and the cell potential. In the galvanostatic mode, the reaction is controlled by applied current leading to deposits with good adhesion and a controlled morphology. However, the cell potential drifts as the reactant activity decreases, leading to multiplicity of products. In the potentiostatic mode, the reaction is carried out by desired cell potential with respect to a reference electrode. Usually, the cell current decreases rapidly as the reaction proceeds due to low rates of diffusion of the reactant molecules to electrode as well as decrease in activity of the reactant. However, the reaction tends to produce a pure single-phase product by the properly chosen potential.

Today, a three-electrode cell is commonly used instead of a two electrode cell (WE and RE) because of its accuracy for large scale cells with high resistive electrolytes. In this arrangement, a counter (or auxiliary) electrode (CE) is placed into the cell, and the current flows between the working electrode and the counter electrode (instead of the reference electrode in the case of the two-electrode cells). In order to avoid an interfering reaction at the working electrode, any convenient one, which does not produce substances by electrolysis, is chosen for the counter electrode. The reference electrode should be placed near the working electrode surface to minimize a loss of voltage drop in electrolyte between the working electrode and the reference electrode. The device used to observe the potential difference between a working electrode and a reference electrode generally has very high input impedance, so a negligible current flows through the reference electrode. Hence, its potential will remain constant and be equal to its open-circuit value.

2.3 Literature Review of Cuprous Oxide (Cu_2O)

2.3.1 Basic Material Properties of Cu_2O

There are several reasons cuprous oxides (Cu_2O) have been researched as potential material for photovoltaic applications. First, Cu_2O has the theoretical solar cell efficiency approximately 19% from only the energy band gap point of view as shown in Figure 1.2. Second, source materials are abundant and non-toxic. Third, Cu_2O can be prepared with simple methods at very low cost. Fourth, Cu_2O has reasonable energy band-gap of about 2.0 eV.

Cu_2O is a complete ionic solid with a density of 6.0 g/cm^3, melting point of 1235 ºC, and thermal expansion coefficient of 3.5× 10^{-6} ºC^{-1} [44]. It is also known as a non-stoichiometric semiconductor [45-48]. The deviation of stoichiometry, δ in $Cu_{2-\delta}O$ is caused by point defects such as copper vacancy, which make the cuprous oxide to a p-type semiconductor [49-53]. It has a direct energy band-gap of about 2.0 eV [54-59] and an electron affinity of 2.9 eV [60].

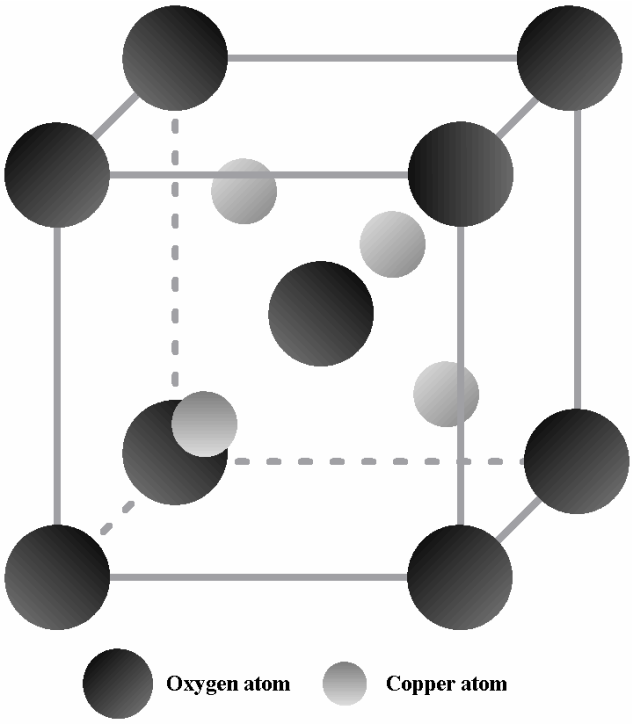

Figure 2.10 Crystal structure of cuprous oxide (Cu_2O)

The crystal structure of Cu_2O is based on a cubic system as shown in Figure 2.10. The unit cell of Cu_2O with a lattice constant of 0.427 nm is composed of a body centered cubic lattice of oxygen ions, in which each oxygen ion occupies the center of a tetrahedron formed by copper ions [61]. Cu_2O appears to be brownish in color and is not soluble in the water.

Cu_2O can be prepared by many methods, including thermal oxidation, anodic oxidation, sputtering, and electrochemical deposition. The thermal oxidation of Cu [49, 62] and floating zone technique [63] can produce single crystalline Cu_2O, while anodic oxidation [64], sputtering [65], and electro-deposition usually make polycrystalline Cu_2O [66-73].

Electrical properties of Cu_2O, such as carrier mobility, carrier concentration, and resistivity are very dependent on preparation methods. It has been reported that the thermal oxidation process normally shows high carrier concentration and low resistivity.

2.3.2 History of Cu_2O Based Devices

The first interest in Cu_2O for device application was initiated by L. O. Grondahl, who fabricated a back-wall Cu_2O rectifier in 1920 [21]. Over the next decade he continued to research the Cu_2O rectifier to elucidate the characteristic of the device. In the 1940s, the research of Cu_2O based device was shifted to the Bell laboratory, and basic understanding of the Cu_2O rectifier was developed by Bardeen, Brattain and Shockley [74]. During the same time period, as Si emerged as a new semiconducting material, most of the interest was shifted to Si. After 1950, for two decades no additional work on Cu_2O was done.

In the 1970s, Cu_2O was in the spot light again due to its potential application in the photovoltaic device. Most of the Cu_2O based PV research was achieved by two research groups, namely Wayne State University and the Joint Center for Graduate Study (JCGS). The metal-Cu_2O Schottky junction solar cell was investigated during this time and the highest efficiency of 1.8 % was achieved at JCGS [18].

Since the 1980s, low temperature methods, such as sputtering, anodic oxidation, and electrochemical deposition, have been introduced for Cu_2O deposition. The electrochemical

method revealed several advantages, such as easy control on film quality and low temperature deposition (<100 ºC). Siripala et al was the first to report n-type behavior of Cu_2O prepared by electrochemical deposition [75].

CHAPER 3

ELECTRICAL, STRUCTURAL, AND OPTICAL PROPERTIES OF ELECTRODEPOSITED CUPROUS OXIDE

3.1 Introduction

Cuprous oxide (Cu_2O) has attracted attention for solar cell applications as the p-type active layer due to its direct band gap of around 2.0 eV [54-59] and its high absorption coefficient, combined with material abundance, non-toxicity, and low-cost fabrication [12,13]. The invention of n-type Cu_2O makes it feasible to fabricate a p-n homojunction Cu_2O solar cell [75], considered to be the best way to increase the efficiency of the Cu_2O based solar cell [18].

The optical and electrical properties of absorber materials in solar cells are key parameters which determine the performance of solar cells. Hence, it is necessary to tune these properties properly for high efficient device. It was reported that structural properties, especially the crystal orientation of electro-deposited Cu_2O, were affected by bath pH, such that Cu_2O oriented to the (100) plane was produced at bath pH ~9.0, and one oriented to the (111) was produced at bath pH ~11.0 [76]. However, the dependency of electrical and optical properties of electro-deposited Cu_2O on deposition conditions has not been clearly explained as of yet.

In this chapter, the dependence of the electrical properties of p- and n-type Cu_2O on several deposition conditions, such as solution pH, deposition potential and temperature, are investigated. The reason why resistivity of Cu_2O is changed depending on its deposition condition is explained by using the structural analysis of Cu_2O. Also, optical characteristics of Cu_2O deposited in various deposition conditions are examined. Additionally, the experimental set up and background are explained in order to better understand material property analysis.

3.2 Experimental

3.2.1 Sample Preparation

The electro-deposition of Cu_2O was performed in a typical 3-electrode cell, as illustrated in Figure 3.1. The deposition of Cu_2O was potentiostatically carried out using a Princeton Applied Research Versastat II potentiostat without stirring. The temperature of the bath was controlled by using a Precision 280 water bath.

Two different substrates were used as the working electrodes for the electro-deposition of Cu_2O. One was ITO (indium tin oxide) on glass substrate with a sheet resistance of 20 ohm/□ for optical characterization. The other one was Cu thin film with a thickness of 200 nm, which was thermally evaporated on a glass substrate for electrical characterization. The sizes of both working electrodes were 1 cm × 4 cm. The Ag/AgCl/sat. NaCl and Pt foil were used as the reference and counter electrode, respectively, for all electro-deposition. Before deposition, ITO/glass and Cu thin film/glass were degreased in ultrasonicated aceton for 10 minutes, etched in 1M nitric acid, and finally rinsed in deionized water.

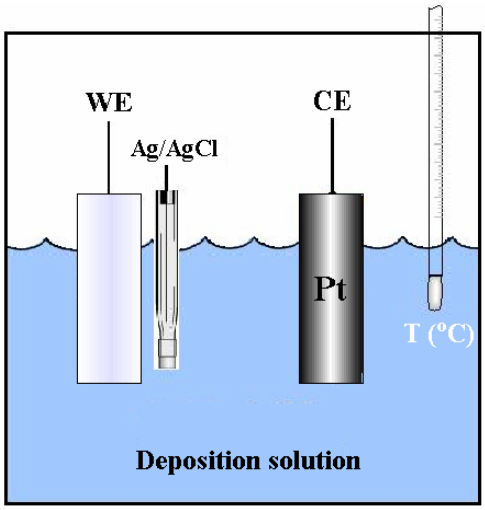

Figure 3.1 Arrangement of a 3-electrode cell for electro-deposition

Two different electrolyte solutions were used for p-type and n-type Cu_2O electro-deposition. For p-type Cu_2O, the aqueous solution contained 0.4 M copper sulfate and either

1.8 M or 3 M sodium lactate. Sodium lactate works as the stabilizer for Cu^{2+} ion at the pH above 9.0. The solution for n-type Cu_2O contained 0.01 M copper acetate and 0.1 M sodium acetate.

In order to examine the dependence of the electrical and optical properties of p-type Cu_2O films on several deposition conditions, the solution pH was varied from 9.0 to 13.0 by adding different amounts of NaOH. The deposition potential was controlled from -0.2 to -0.6 V versus the Ag/AgCl/sat. NaCl reference electrode. The deposition temperature was adjusted from 40 to 80 ℃. In the case of n-type Cu_2O, the solution pH was controlled from 5.2 to 6.4 with different amounts of acetic acid, the deposition potential was fixed at -0.1 V, and the temperature was 60 ℃.

X-ray diffraction patterns of Cu_2O were obtained by a Siemens D-500 powder diffractometer using Cu K_α radiation. A Zeiss Supra 55 scanning electron microscopy were used to characterize surface morphology and grain size of Cu_2O.

3.2.2 Cyclic Voltammetry (CV)

Cyclic voltammetry (CV) is a potentiodynamic electrochemical measurement used for the mechanistic study of redox systems in the electro-chemical cell [43]. In CV, the voltage is linearly applied to the electrode with a given scan rate (V/sec.). During the negative (forward) scan, the current in the electrochemical cell increases when any solute in the electro-chemical cell is reduced and reaches the peak, corresponding to the reduction potential of a given solute. Then the current decreases as the concentration of the solute is depleted close to the electrode surface. If the redox couple is reversible, the product formed in the reduction process can be oxidized when the applied potential is reversed (backward). The reverse scan also produces a current peak, corresponding to the oxidation potential. The oxidation peak normally has a similar shape to the reduction peak and an opposite polarity to the reduction peak. As a result, information about the redox potential and the electrochemical reaction rates of the compounds can be obtained by CV.

The redox couple in the solution for Cu_2O deposition is not reversible. Hence, only the negative scan, called linear voltammetry, was performed. Figure 3.2 shows typical voltammogram of the solution for (a) n-Cu_2O and (b) p-Cu_2O deposition. The solution for Figure 3.2 (a) contained 0.01 M copper acetate and 0.1 M sodium acetate. The temperature of the solution was kept at 60°C. pH of the solution was 6.4, controlled by acetic acid. Two reduction reactions were observed due to the presence of cupric ions in the electrolyte. The first reduction that took place between -0.05 and -0.12 V (vs. Ag/AgCl/saturated NaCl) contributes to the formation of Cu_2O by the following reaction.

$$2Cu^{2+} + H_2O + 2e^- \rightarrow Cu_2O \downarrow + 2H^+ \quad (3.1)$$

The second reduction that occurred after -0.2 V contributes to the formation of Cu by the following reaction.

$$Cu^{2+} + 2e^- \rightarrow Cu \downarrow \quad (3.2)$$

The potential window for the Cu_2O deposition in acetate bath is very narrow, so a constant potential of -0.1 V was used for all depositions of n-type Cu_2O.

The solution for Figure 3.2 (b) contained 0.4 M copper sulfate and 3 M sodium lactate. The temperature of the solution was kept at 60 °C. The pH of the solution was 9.0, controlled by NaOH. In contrast to the solution for n-Cu_2O, the first reduction took place in the wide range between -0.17 to -0.6 V (vs. Ag/AgCl/saturated NaCl). That reduction contributes to the formation of Cu_2O by the following reaction.

$$Cu^{2+} + e^- \rightarrow Cu^+ \quad (3.3)$$

$$2Cu^+ + 2OH^- \rightarrow Cu_2O \downarrow + H_2O \quad (3.4)$$

The second reduction that occurred after -0.9 V contributes to the formation of Cu. Therefore, the samples of p-Cu_2O were deposited at the different voltages between -0.2 to -0.6 V in order to check the dependency of the electrical properties of p-Cu_2O on applied potential.

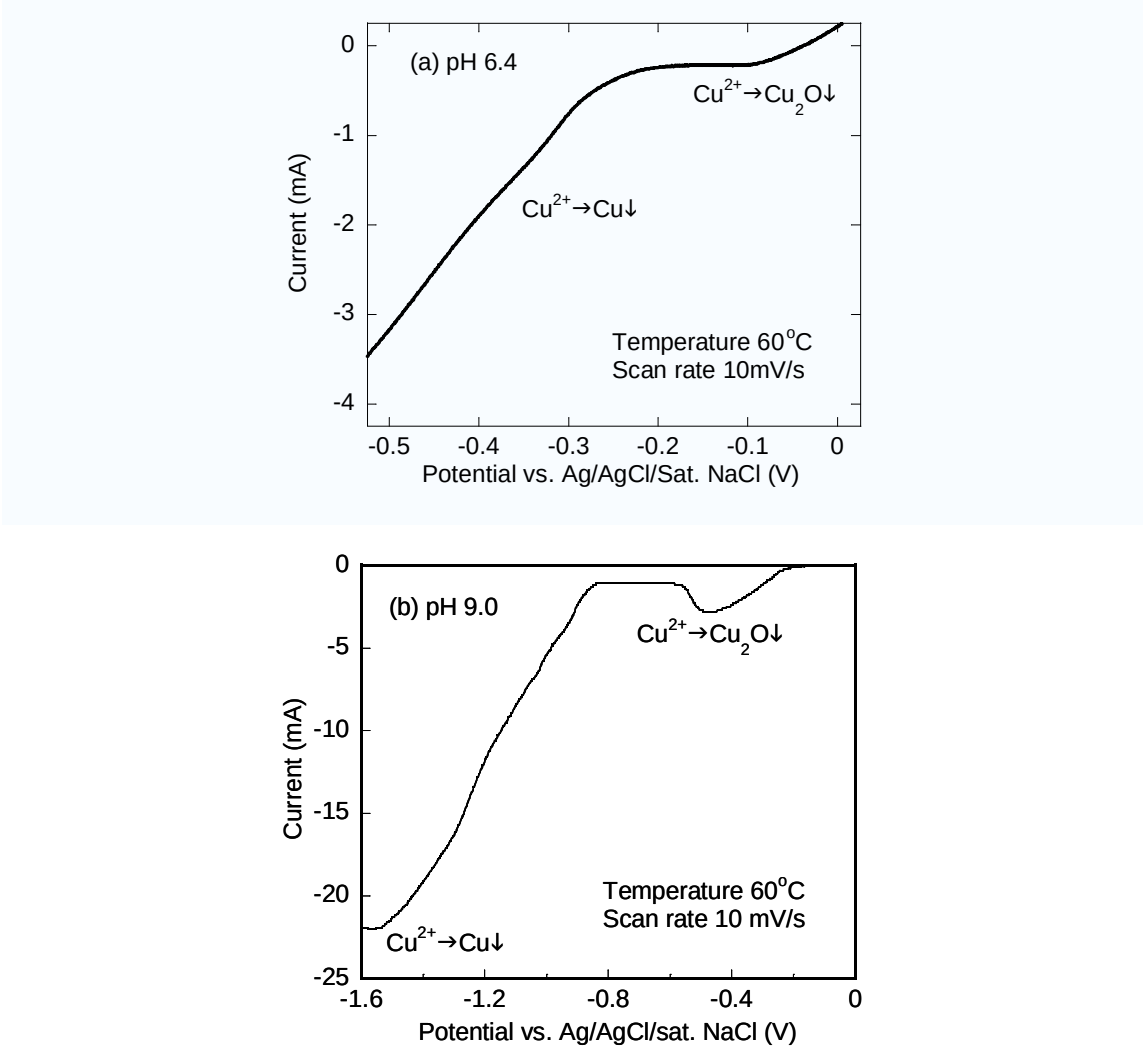

Figure 3.2 Linear voltammograms of solutions for (a) n-Cu_2O, and (b) p-Cu_2O deposition

3.3 Electrical and Structural Properties of Electrodeposited Cuprous Oxide

3.3.1 Photovoltammogram of Cu_2O

When a semiconductor is immersed in a redox electrolyte, the equilibrium of the interface between the semiconductor surface and the electrolyte is achieved by the flowing of the charges from one phase to the other. The charge flowing contributes to the formation of the depletion layer and the band-bending in the semiconductor phase. If light illuminates the interface between the semiconductor surface and the electrolyte, electron-hole pairs are

generated in the semiconductor. These charge carriers can move either to the semiconductor bulk or to the electrolyte by the internal electric field, which is built in the depletion layer. It is called photocurrent. The photocurrent is normally dependent on light wavelength, electrode potential, and electrolyte composition.

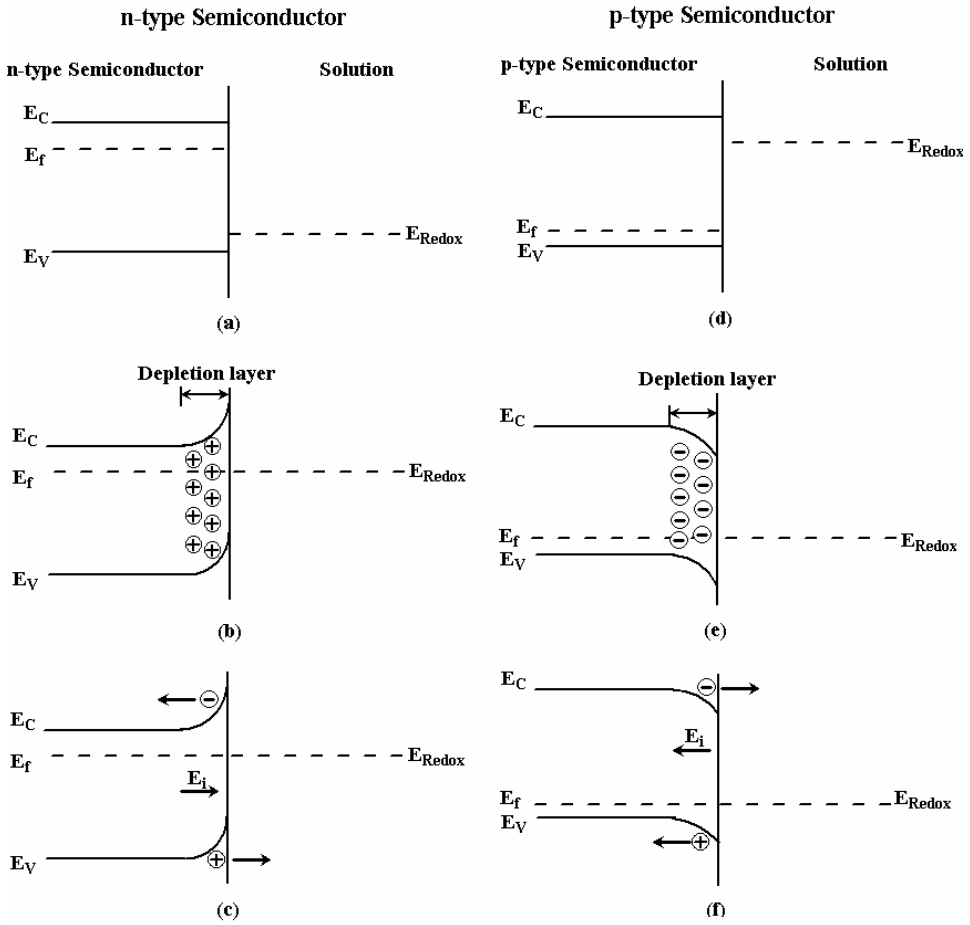

Figure 3.3 Junction characteristics between the n-type and p-type semiconductors, and the electrolyte containing redox couple (a,d) before contact, (b,e) after contact, and (c,f) under irradiation

Figure 3.3 illustrates the junction formation between the n- and p-semiconductors and the electrolyte. In the case of an n-type semiconductor, the positive space charge region (depletion layer) is formed due to its Fermi-level, originally higher than the redox potential of the electrolyte before contact, corresponding to Figure 3.3 (a) and (b). As shown in Figure 3.3 (c),

under irradiation, the photon, which has energy greater than the energy band-gap of the semiconductor, generates electron-hole pairs. By the built-in electric field, the electrons move to the bulk of the semiconductor, and the holes move to the electrolyte, which is defined as anodic photocurrent. In the case of a p-type semiconductor, the negative space charge region is formed, so the holes move to the bulk of the semiconductor, and the electrons move to the electrolyte under irradiation, which is defined as cathodic photocurrent, as illustrated in Figure 3.3 (d, e, and f).

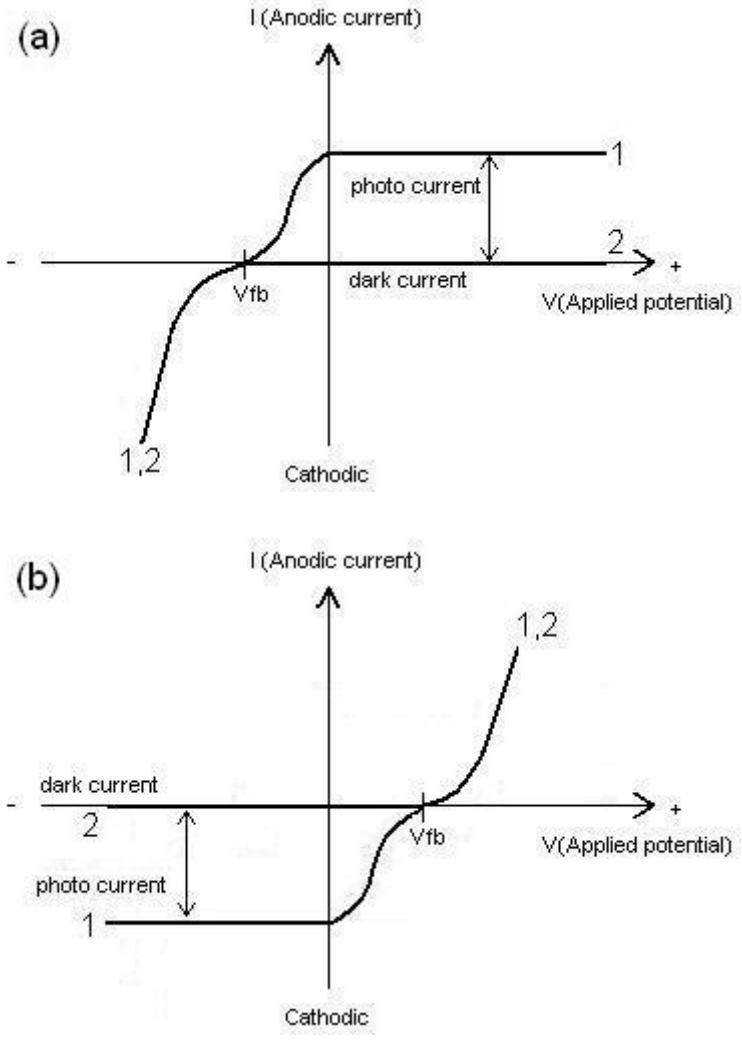

Figure 3.4 Typical characteristics of the (1) photocurrent, and the (2) dark current of (a) n-type, and (b) p-type semiconductor in the electrolyte

Typical photovoltammogram curves of an (a) n-type, and a (b) p-type semiconductor are shown in Figure 3.4 [43]. For an n-type semiconductor in the darkness, there is no current flow when the potential, more positive than the flat band potential (V_{fb}), is applied to the electrode, because the potential barrier between the semiconductor surface and the electrolyte does not allow the carriers to flow, as is shown by curve 2 in Figure 3.4 (a). However, under irradiation, photocurrents are generated by the photo-induced electron-hole pairs. The photocurrent is distinguished from the dark current when the applied potential to the electrode is more positive than the flat band potential (V_{fb}), as is shown by curve 1 in the Figure 3.4 (a). For a p-type semiconductor, the photocurrent is distinguished from the dark current when the applied potential to the electrode is more negative than the flat band potential (V_{fb}), shown in the Figure 3.4 (b). The V_{fb} can be obtained by observing the potential at which photocurrent is distinguished. It is used to characterize the electrical properties of the semiconductor electrode.

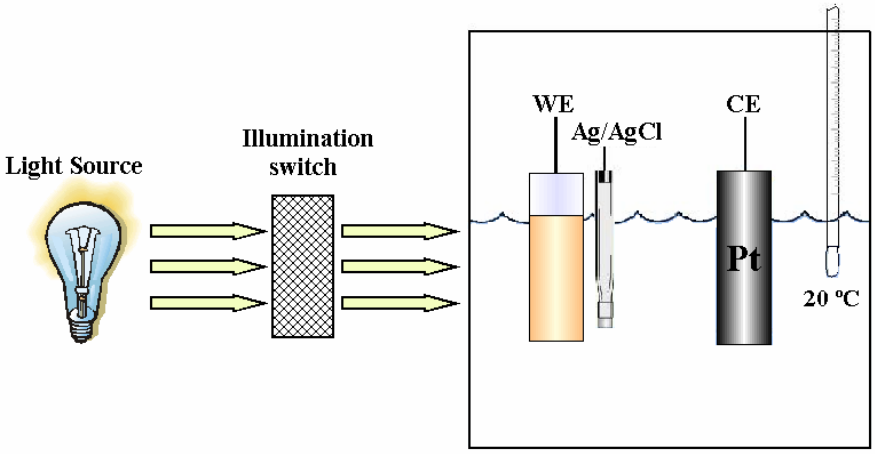

Figure 3.5 Arrangement of a photocurrent characterization system.

Photocurrent characterization was performed in a custom-built system, including a light source, an illumination switch, and a three-electrode electrochemical cell, as illustrated in the Figure 3.5. The light source was a 150-W Schott ACE halogen lamp with broad spectrum. The illumination switch was controlled manually to chop the light in certain time intervals. In the three-electrode cell, the working electrode was as-deposited Cu_2O films facing on the light

source, the counter electrode was a platinum wire, and the reference electrode was Ag/AgCl/sat. NaCl. The electrolyte was an aqueous solution of 0.1 M sodium acetate.

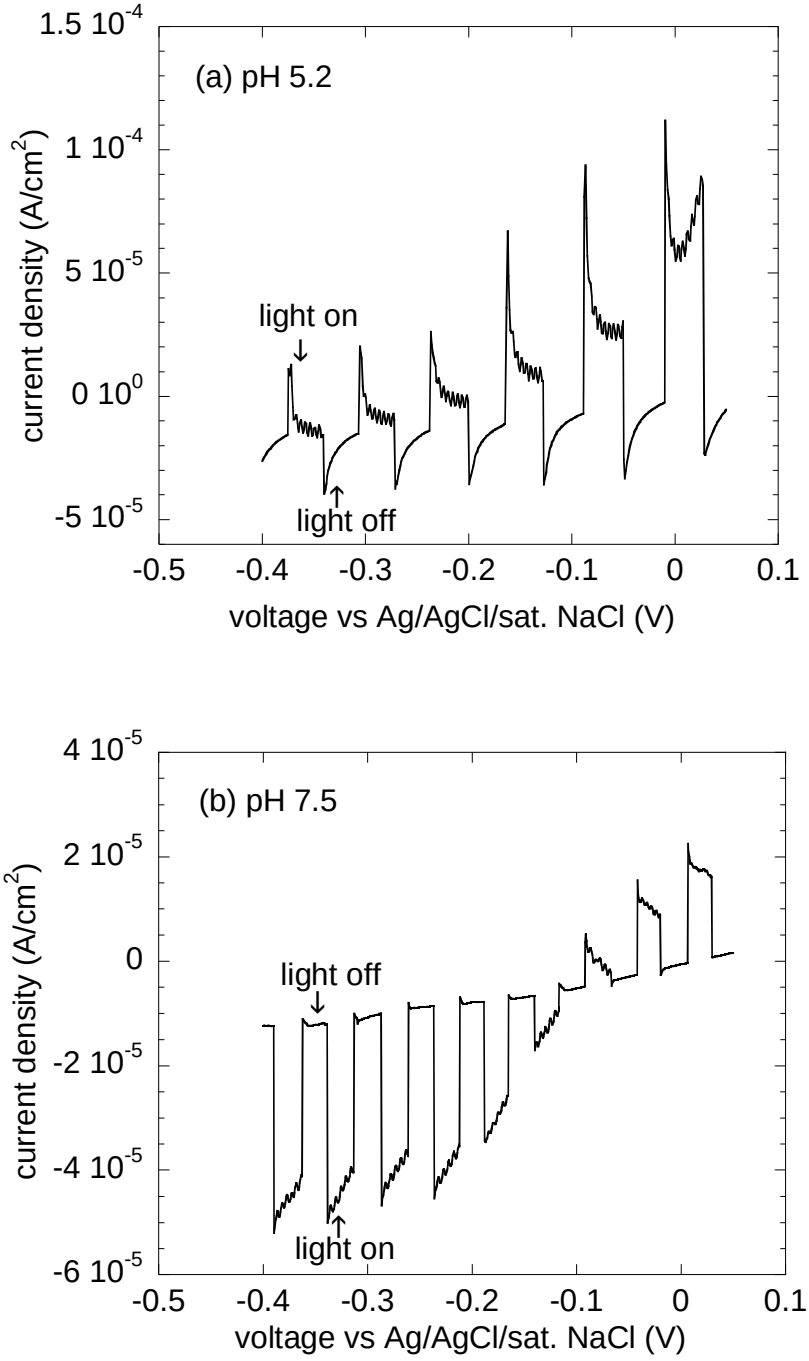

Figure 3.6 Photovoltammogram under interrupted illumination of Cu_2O deposited at different solution pH (a) 5.2, (b) 7.5

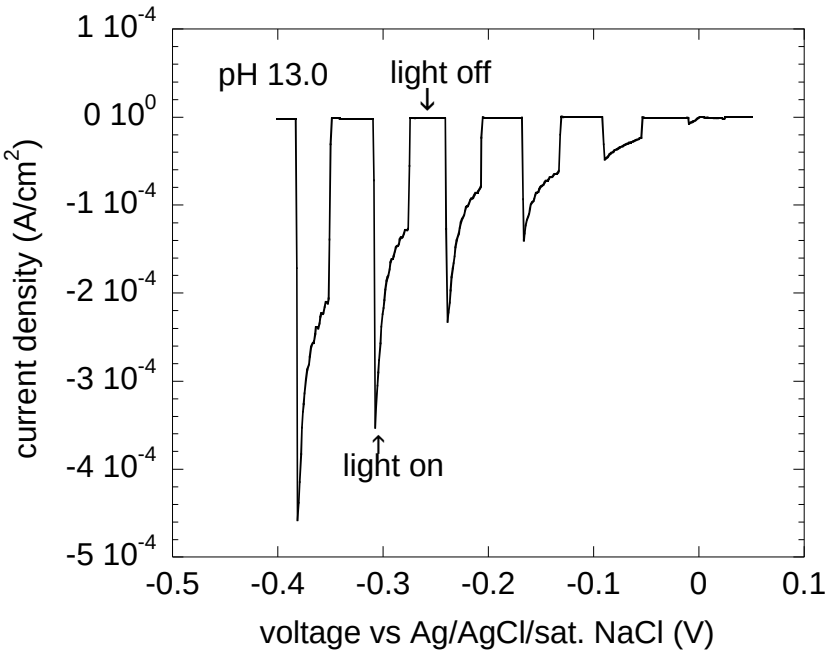

Figure 3.7 Photovoltammogram under interrupted illumination of Cu_2O deposited at solution pH 13.0

Figure 3.6 (a) shows the photocurrent of Cu_2O, deposited at solution pH 5.2 in an aqueous solution containing 0.01 M copper acetate and 0.1 M sodium acetate. It generated only an anodic photocurrent in the voltage range from the -0.4 to 0.05 V, which represents the typical behavior of the n-type semiconductor. The flat band voltage of -0.46 V was obtained from the sample. The photocurrent of Cu_2O, deposited at solution pH 13.0 in an aqueous solution containing 0.4 M copper sulfate and 3 M sodium lactate, is shown in figure 3.7. It generated only a cathodic photocurrent in the same voltage range, which represents the typical behavior of the p-type semiconductor. The flat band voltage of 0.05 V was obtained from the sample. Interestingly, As shown in Figure 3.6 (b), the Cu_2O, deposited at pH 7.5 in an aqueous solution containing 0.4 M copper sulfate and 3 M sodium lactate, showed the flat band voltage of -0.11 V, which is in the middle range between the flat band voltage of Cu_2O deposited at pH 13.0 and

the flat band voltage of Cu_2O deposited at pH 5.2. As a result, the flat band voltage of Cu_2O increased positively as the pH of the deposition solution increased.

It has been known that a p-type property of Cu_2O is caused by point defect, copper vacancy, which means there is stoichiometrically more oxygen than copper in the film [45-48]. If the incorporation of oxygen in the film can be controlled, it will be possible to control the amount of copper vacancy and even to change the type of point defect to oxygen vacancy. It is believed that the oxygen incorporation in the film can be controlled by the amount of oxygen precursor, OH^-, in the solution. As a result, the high pH in the solution is more preferable in producing a p-type behavior such as copper vacancy, in Cu_2O, while the low pH in the solution is more preferable in producing an n-type behavior such as oxygen vacancy or copper interstitial, in Cu_2O [77].

3.3.2 Electrical and Structural Properties of Cu_2O

Four-point probe and Hall measurements are the standard and reliable methods used in characterizing electrical properties of thin semiconductor films. However, it is difficult to characterize the electrical properties of electrochemically-deposited semiconductor films with these methods because of the highly-conductive substrate required for electrochemical deposition. Even though a two-layer model is available for Hall measurements, it is difficult to characterize highly-resistive semiconductor films due to the small Hall voltage [78].

In this study we adopted a simple current-voltage method to characterize the electrical properties of both p- and n-type Cu_2O films. Circular Cu electrodes with an area of 2.2×10^{-3} cm^2 were deposited on the top surfaces of both p- and n-type Cu_2O by thermal evaporation. A voltage was applied between the substrate and the top electrode, and the current was measured at room temperature with a HP 4145A semiconductor parameter analyzer. From the slope of the current-voltage (I-V) relation, the area of Cu top electrode, and the thickness of the Cu_2O film, the resistivity was determined. The schematic for 2-probes resistivity measurement is shown in Figure 3.8.

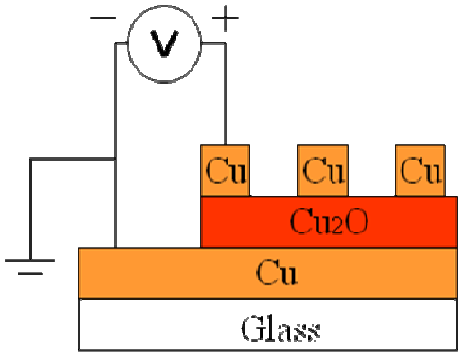

Figure 3.8 Sample structure for resistivity measurement

When I-V measurements were performed to determine the resistivity of both p- and n-type Cu_2O films, none displayed a linear I-V behavior, due to the Schottky barrier between Cu and Cu_2O [18]. The resistivity of Cu_2O films was thus determined by the linearization of the forward current between 1.7 and 2 V, and it showed a similar order of magnitude to values reported by a different method [79], thus indicating the validity of the measurement. These resistivity values were enough to evaluate the dependence of resistivity of electrochemically-deposited Cu_2O on different deposition conditions.

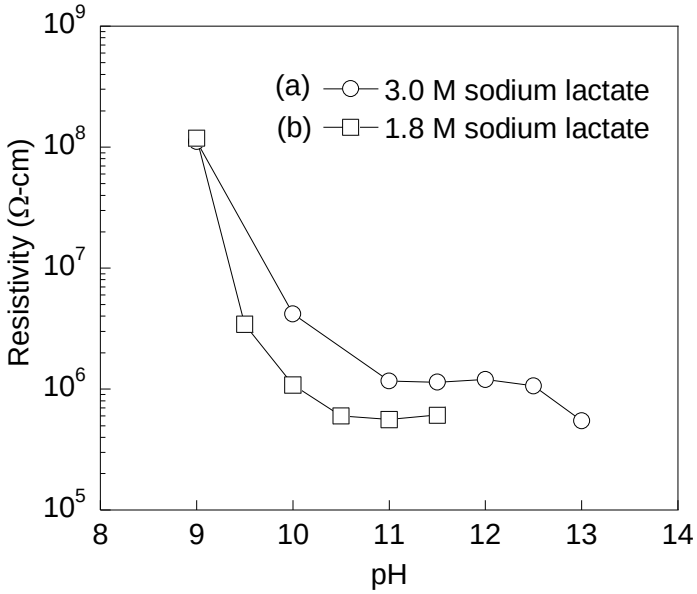

Figure 3.9 Resistivity of p-type Cu_2O films as a function of solution pH and sodium lactate molarity: The deposition was performed at -0.4 V and 60 ℃

P-type Cu_2O films of 2.5 um in thickness were prepared in basic solutions under various conditions. Figure 3.9 shows the resistivity of p-type Cu_2O deposited at different pH solutions and sodium lactate concentrations. As the pH of the solution increased, the resistivity of p-type Cu_2O decreased. The p-type Cu_2O film prepared with 3 M sodium lactate at pH 13 showed the smallest resistivity, which is over two orders of magnitude smaller than that of the film deposited at pH 9. Figure 3.10 shows the XRD spectra of p-type Cu_2O films deposited with 3 M sodium lactate at pH of solutions of 9 and 13, respectively. Cu_2O deposited at solution pH 13 has preferential orientation of (111), while Cu_2O prepared at solution pH 9 has a preferred orientation of (100).

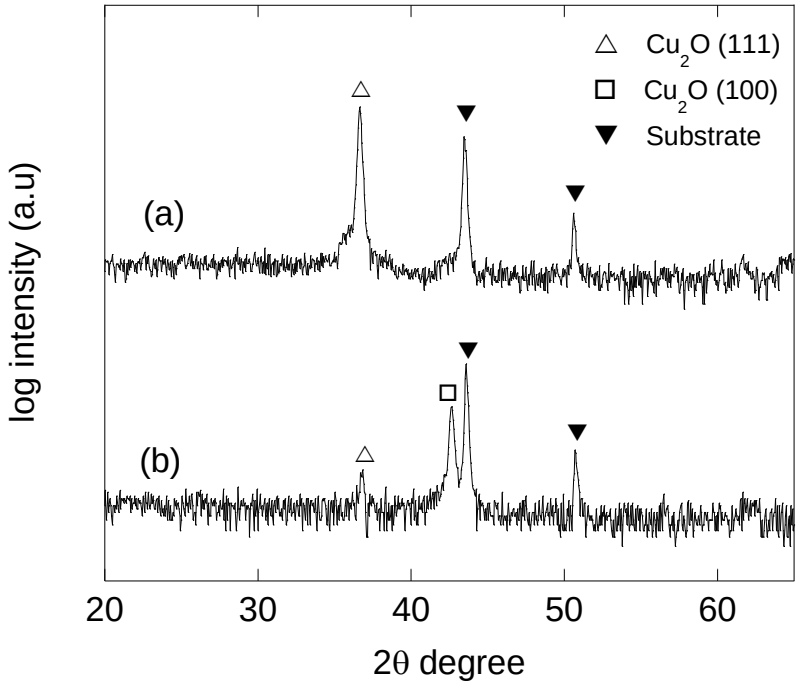

Figure 3.10 XRD spectra of p-type Cu_2O films deposited at -0.4 V, 60 ℃ and 3 M sodium lactate on Cu/glass substrates with solution pH (a) 13 and (b) 9

It is known that solution pH significantly influences crystal orientation and surface morphology [66]. Also, the photocurrent measurement revealed that pH can control the amount of point defect, and even the type of point defect. It is suggested that the low resistivity of Cu_2O deposited at a high solution pH is related to its (111) orientation. Crystal grains with (111)

orientation may have more intrinsic point defects, i.e. Cu vacancies that determine the carrier concentration than crystal grains with (100) orientation.

The resistivity of Cu_2O films deposited with 1.8 M sodium lactate was lower than that of Cu_2O prepared with 3.0 M sodium lactate at a solution pH of between 9 and 11.5. It was found that the surface morphology of Cu_2O deposited with 1.8 M sodium lactate was different from that prepared with 3 M sodium lactate at the same solution pH and deposition potential. As shown in Figure 3.11, Cu_2O deposited with 1.8 M sodium lactate at solution pH 11 has more uniform grains with (111) orientation, while Cu_2O prepared with 3 M sodium lactate at the same solution pH has grains of various sizes with prism shapes oriented towards (110). It appears that the (111) orientation is more favorable for low resistivity than the (110) orientation in p-type Cu_2O.

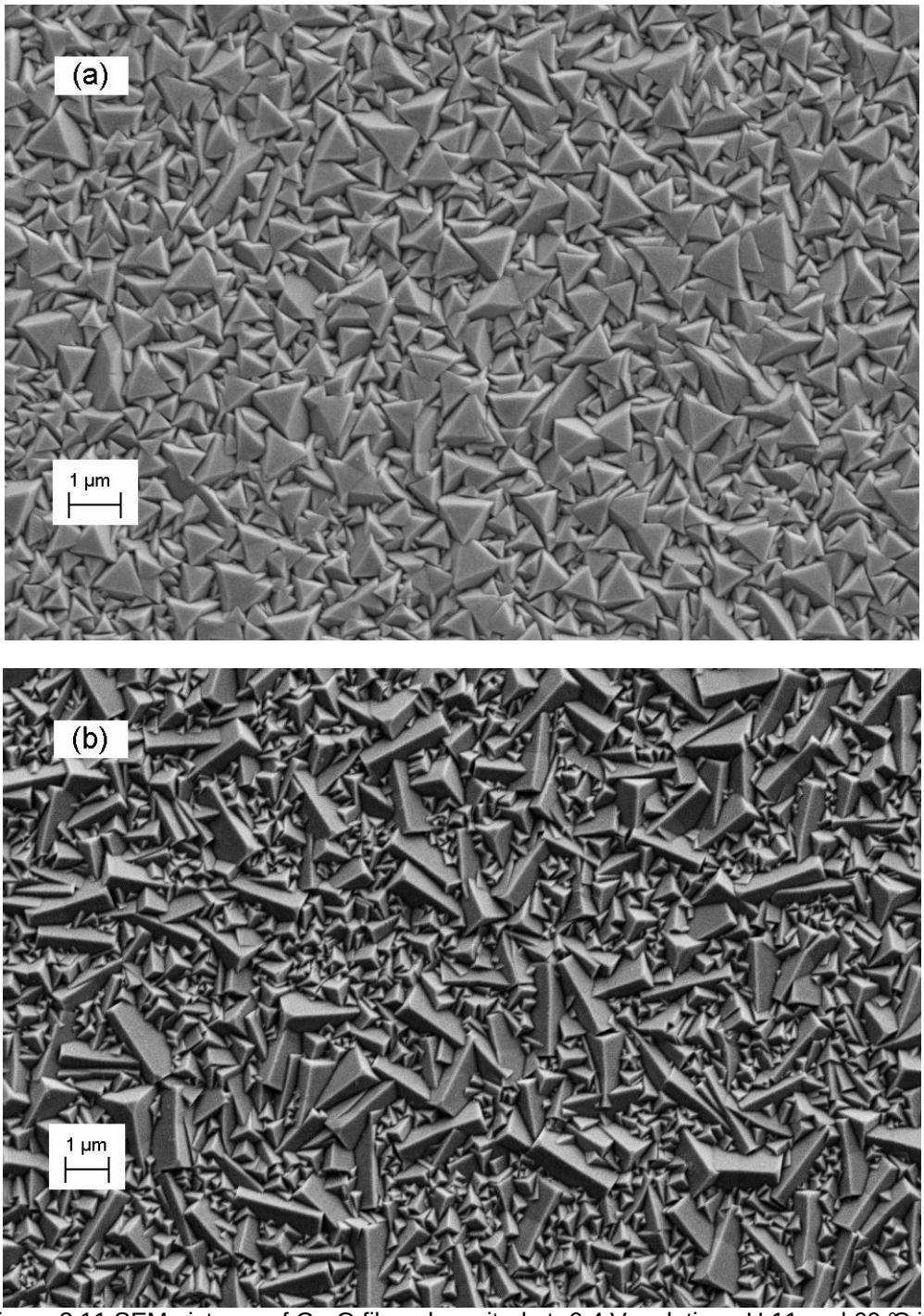

Figure 3.11 SEM pictures of Cu_2O films deposited at -0.4 V, solution pH 11 and 60 ℃ in solutions containing (a) 1.8 M and (b) 3 M sodium lactate.

Figure 3.12 shows the dependence of resistivity of p-type Cu_2O deposited at solution pH 13 as a function of deposition potential and temperature, respectively. The variations of resistivity depending on these parameters are not as sensitive as in the case of the solution pH as shown in Figure 3.9. The resistivity of p-type Cu_2O decreases as the deposition temperature increases and the deposition potential decreases. From the SEM pictures in Figure 3.13, it is suggested that the variations in resistivity are due to a change in grain size.

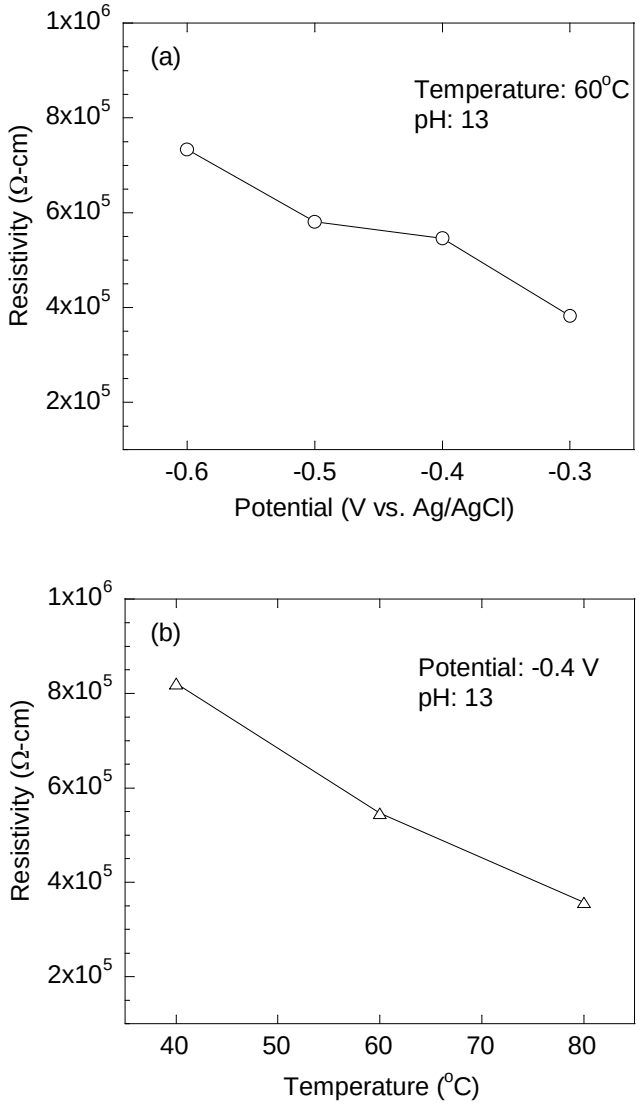

Figure 3.12 Resistivity of p-type Cu_2O films deposited at solution pH 13 and (a) potential from -0.3 to -0.6 V at 60 ℃ and (b) temperature from 40 to 80 ℃ at -0.4 V

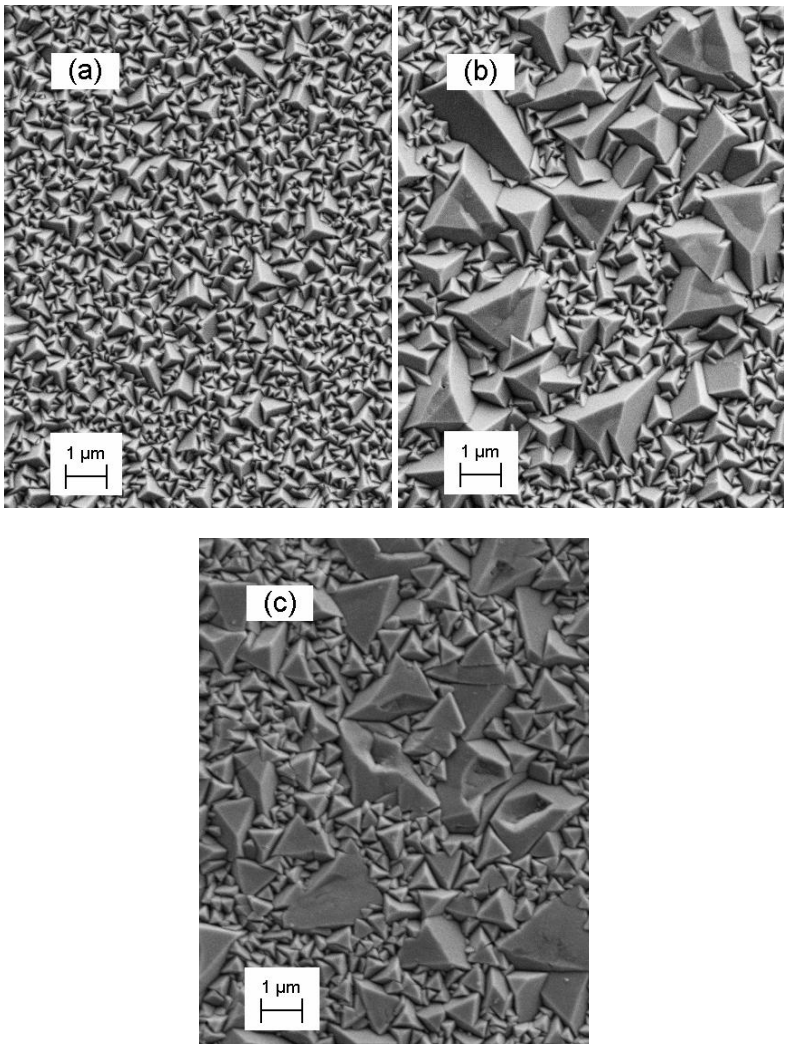

Figure 3.13 SEM pictures of Cu_2O films deposited at solution pH 13 and (a) -0.4 V and 60 ℃; (b) -0.3V and 60 ℃ and (c) -0.4 V and 80 ℃.

The I-V measurement was also executed to characterize 2-um n-type Cu_2O films deposited at solution pH from 5.2 to 6.4 on Cu/glass substrates. The resistivity of n-type Cu_2O deposited at different pH solutions is shown in Figure 3.14. It also tended to slightly decrease as the solution pH increased. N-type Cu_2O exhibited higher resistivity by at least two orders of magnitude than did p-type Cu_2O deposited at pH 13. The lowest resistivity of 5×10^7 ohm-cm was obtained at pH 6.4 for n-type Cu_2O.

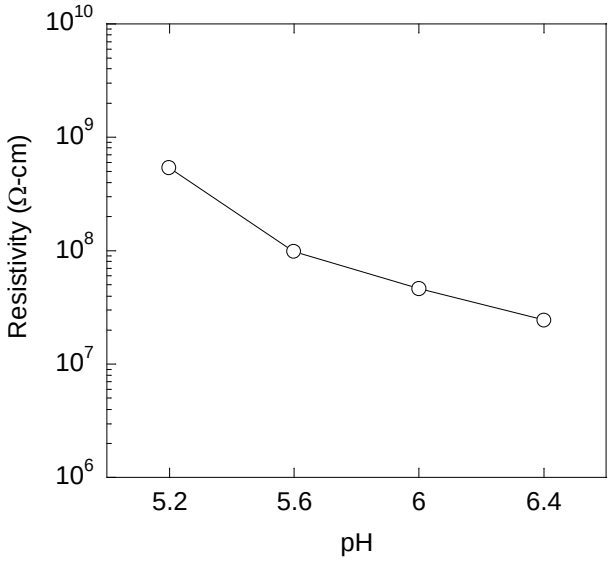

Figure 3.14 Resistivity of n-type Cu_2O films deposited at -0.1 V and 60 ℃ in solutions with different pH.

3.4 Optical Properties of Electrodeposited Cuprous Oxide

3.4.1 Determination of Band Gap

The band gap is the difference in energy between the lowest conduction band edge and the highest valence band edge. Electrons in a valence band can be excited to the conduction band, where they become mobile by photon absorption as shown in Figure 3.15. The most common method for determination of band gap for a given material is optical absorption analysis.

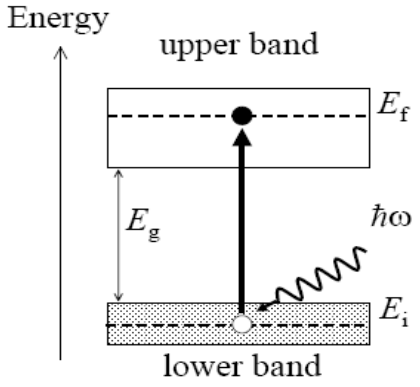

Figure 3.15 Electron transition from valence band to conduction band by photon absorption

There are two types of electron transition processes from valence band to conduction band. One is the direct transition process, and the other one is the indirect transition process.

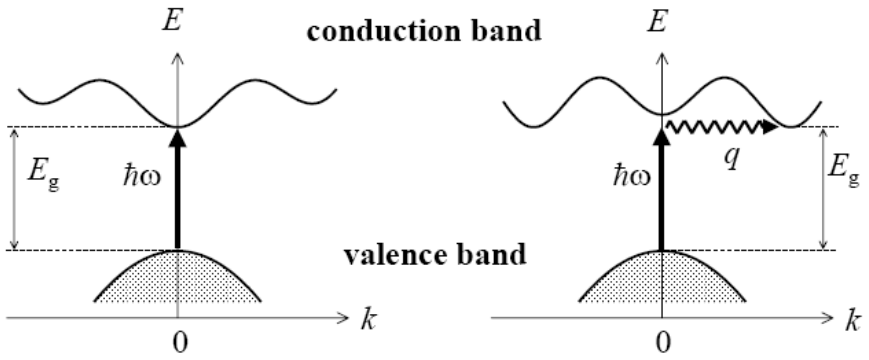

(a) Direct band gap (b) Indirect band gap

Figure 3.16 Comparison between the direct absorption and the indirect absorption

In the case of direct band-gap material, as shown in Fig 3.16 (a), the lowest conduction band edge has same wave vector k as the highest valence band edge. Therefore, direct optical transition happens vertically with no significant change of k by photon energy, and the threshold photon frequency ω determines the energy band gap $E_g = \eta\omega$ for direct transition process. Usually direct band gap materials show abrupt increase of absorption coefficient from this threshold photon frequency.

However, in the case of indirect band gap material, the lowest conduction band edge has a different wave vector k value with that of the highest valence band edge. The direct photon transition between these minimum band edges can not satisfy the requirement of wave vector conservation, because photon wave vector ($2\pi/\lambda \sim 10^7 m^{-1}$) is usually negligible compared to Brillouin zone size ($\pi/a \sim 10^{10} m^{-1}$) . Therefore phonon energy (ηq) having wave vector (Δk) should be involved in electron transition from the highest valence band edge to the lowest conduction band edge for momentum conservation, as illustrated in Fig 3.16 (b). So photon energy ($\eta\omega$) as well as phonon energy (ηq) are needed for electron transition in an

indirect band structure. The indirect transition process is a 2nd order process, having three particle interactions between an electron, a photon, and a phonon. Hence, this indirect transition process can occur much less frequently than a direct transition process from the transition probability point of view. The photon absorption around the threshold frequency of an indirect transition process is weaker than that of a direct transition process.

The absorption of light by an optical medium is quantified by its absorption coefficient, α. To calculate the magnitude of the absorption coefficient, α**,** associated with an optical transition, a calculation of quantum mechanical perturbation must be carried out in which the effect of the light is treated as a perturbation in the basic Schrödinger equation.

For a direct transition, the transition probability depends only on the square of the matrix element involving the interaction of the light with the electrons, and this is hence a first order process. The final result of α as function of photon energy, $\eta\omega \geq E_g$ in direct transition is given by

$$\alpha\eta\omega \propto (\eta\omega - E_g)^{1/2} \tag{3.5}$$

so that a plot of $(\alpha\eta\omega)^2$ vs $\eta\omega$ gives a straight line with the intercept of E_g [80].

For indirect transition, the transition probability is proportional to the product of the square of the matrix element for photon-electron interaction and the square of the matrix element for phonon-electron interaction. The actual form of α is given by

$$\alpha\eta\omega \propto \langle n\rangle\left(\eta\omega + E_{pn} - E_g\right)^2 + \left(1+\langle n\rangle\right)\left(\eta\omega - E_{pn} - E_g\right)^2 \tag{3.6}$$

where $\langle n\rangle = \left[\exp\left(E_{pn}/kT\right)-1\right]^{-1}$ is the Bose-Einstein distribution. The first term in equation (3.6) means optical absorption with the absorption of phonon, and the second term means optical absorption with the emission of phonon. Therefore, a plot of $(\alpha\eta\omega)^{1/2}$ vs $\eta\omega$ gives two straight lines. If these two straight lines intersect the $\eta\omega$ axis at $\eta\omega_1 = (E_g - E_{pn})$ and

$\eta\omega_2$ = ($E_g + E_{pn}$) with $\eta\omega_1 < \eta\omega_2$, the band-gap energy, E_g is $(\eta\omega_1 + \eta\omega_2)/2$, and the phonon energy, E_{pn} is $(\eta\omega_2 - \eta\omega_1)/2$. Usually, this phonon energy is much smaller than band gap energy,so that the energy difference between E_g and E_{pn} at $\eta\omega$ axis can be negligible. Hence, a plot of $\alpha\eta\omega^{1/2}$ vs $\eta\omega$ gives a straight line with the intercept of E_g for the indirect absorption process [80].

Experimentally, the absorption coefficient, α, can be obtained by using Beer's law as shown in equation 3.7

$$I(z) = I_0 e^{-\alpha z} \tag{3.7}$$

where I_0 is the optical intensity at Z=0. The equation 3.7 can be translated to a different form,

$$\alpha = \frac{1}{t}\ln(\frac{1}{T}) \tag{3.8}$$

where t is a thickness of the medium and T is transmissivity. Hence, the absorption coefficient, α, can be calculated by using experimental values of thickness and transmissivity of the medim [81].

3.4.2 Optical Properties of Cu_2O

In order to investigate the optical properties of electro-deposited Cu_2O, the electro-deposition of Cu_2O was performed on transparent indium tin oxide (ITO) glass with a sheet resistance of 20 ohm/□ as the working electrode. Ag/AgCl/sat. NaCl and platinum foil were used as the reference and counter electrode, respectively.

By controlling the deposition time, all Cu_2O samples for optical characterization were grown to have thickness of 2.5 um, as measured by an Alpha-Step IQ profilometer. The optical characterization was performed with a Jasco V570 spectrophotometer.

The optical process in Cu_2O film/ITO/glass substrate for transmittance measurement is shown in Fig. 3.17. The final transmittance of this sample cannot be considered as transmittance of only Cu_2O, because some amount of light transmitted through the Cu_2O layer

is reflected at the interface between the Cu_2O and the ITO and absorbed in the ITO/glass substrate. This situation is quantitatively described in equation 3.9.

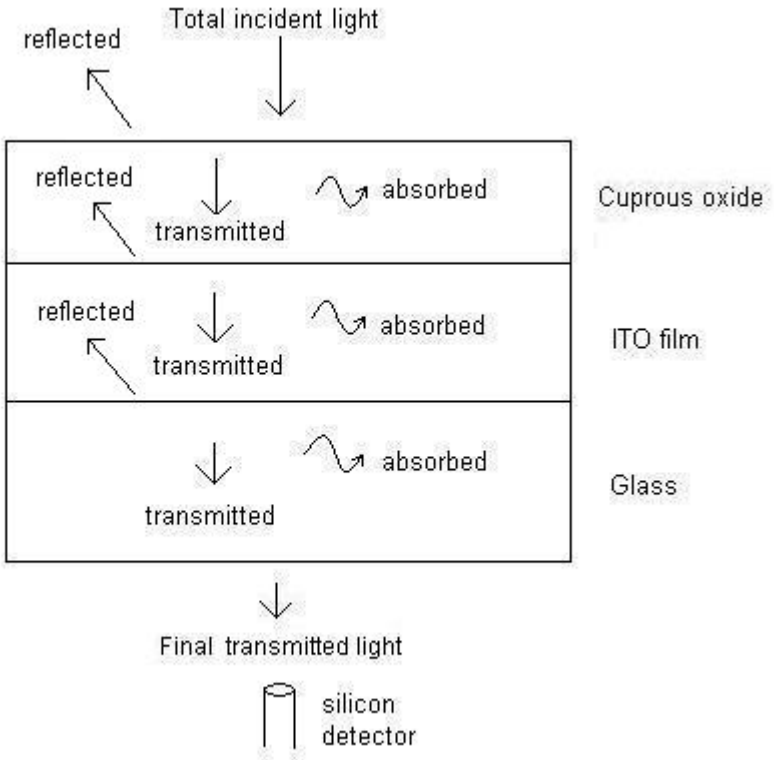

Figure 3.17 Schematic of transmittance measurement.

The final transmittance (T) = total incident light $\times$ *T of* Cu_2O *film* $\times$ *T of ITO/glass* (3.9)

Hence, the transmittance of ITO/glass substrate was characterized in advance and the transmittance of only Cu_2O was obtained by using equation 3.9.

The transmittance spectrum of Cu_2O deposited at different pH values is shown in figure 3.18. The Cu_2O deposited at pH 12.0 showed larger variation of interference fringes in its transmittance spectrum than did the Cu_2O deposited at pH 9.0. These interference fringes are normally caused by the interference of light reflected from the front and rear surfaces. It was observed that the Cu_2O with a thickness of 2.5 um, deposited at pH 12.0, had a flat surface morphology, while the Cu_2O with same thickness, deposited at pH 9.0, had a very sharp surface

morphology of a 4-sided pyramid shape. As a result, the Cu_2O deposited at pH 12.0 had more light reflection than the Cu_2O deposited at pH 9.0 at the surface, which attributed a larger variation of interference fringe.

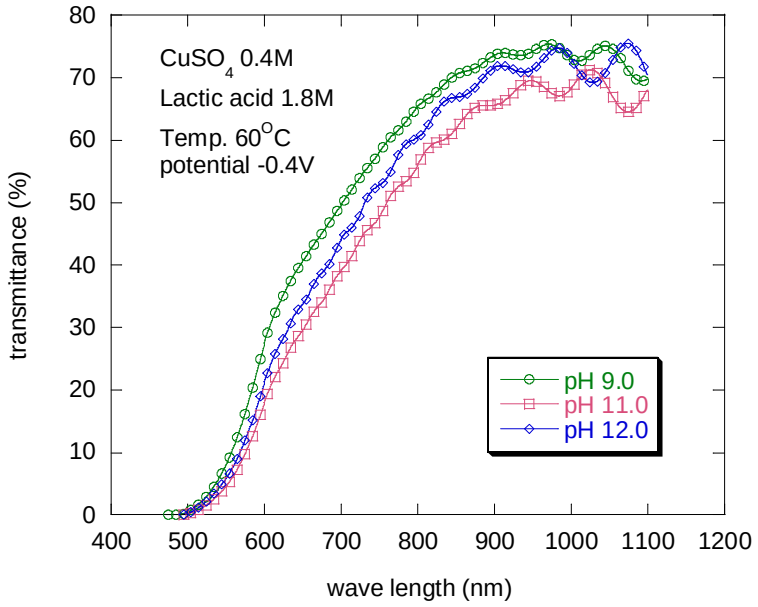

Figure 3.18 Transmittance of Cu_2O deposited at different pH values

The energy band-gap of Cu_2O was determined by extrapolation from the plot of $(ahv)^2$ versus hv. The absorption coefficient, α was calculated by equation 3.8. The potential error range where transmittance is below 3% was excluded in the calculation of absorption coefficient, α.

The energy band-gap of Cu_2O, deposited at the different pH solutions, is shown in Figure 3.19. The energy band-gaps of 2.101, 2.064, and 2.061eV were obtained at solution pH of 9.0, 11.0, and 12.0 respectively. These values are consistent with the reported band-gap value of Cu_2O [54-59]. It was found that at solution pH above 9.0, the energy band-gap of Cu_2O slightly decreased as the solution pH increased. However, at pH below 9.0, the energy band-gap of Cu_2O was constant to 2.1 eV.

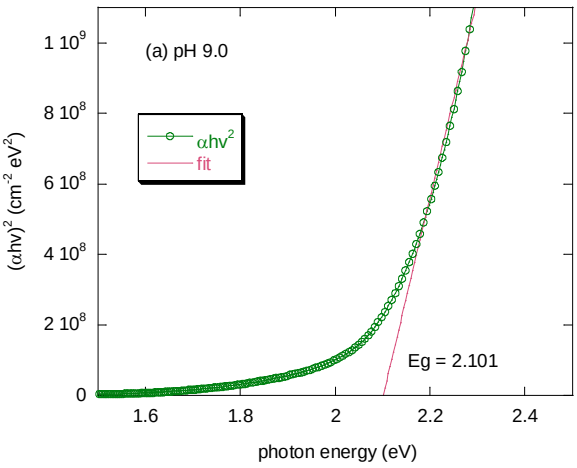

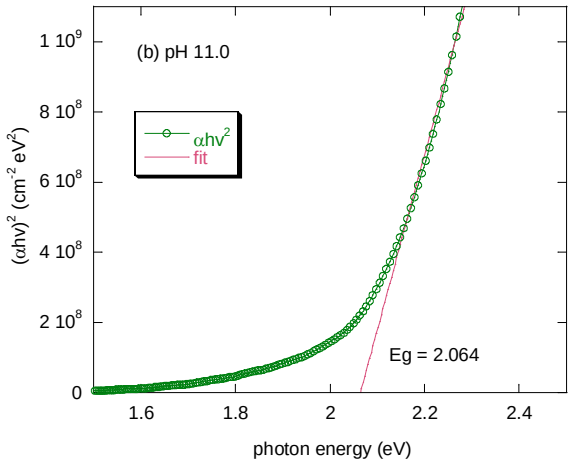

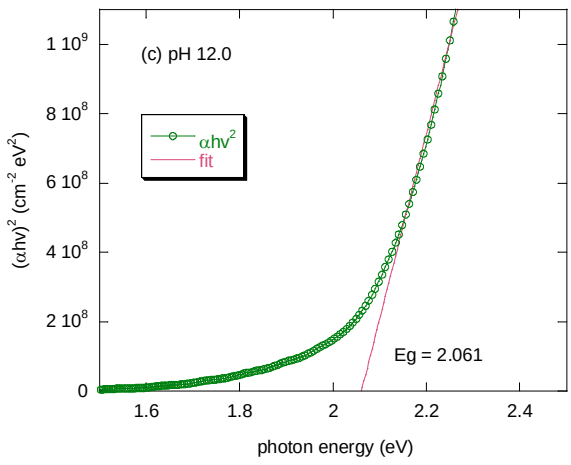

Figure 3.19 Dependency of energy band-gap of Cu_2O on deposition solution pH

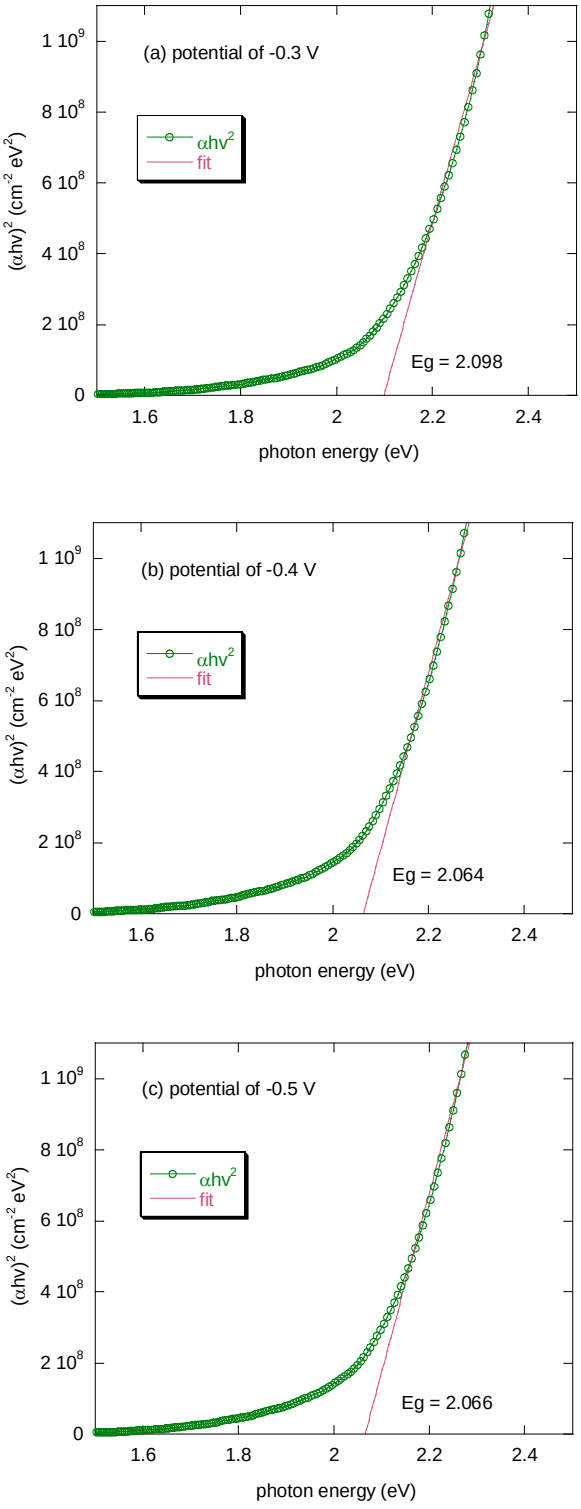

Figure 3.20 Dependency of energy band-gap of Cu_2O on deposition potential

The dependence of the energy band gap of Cu_2O on the deposition voltage is shown in Figure 3.20. It was found that the energy band-gap slightly decreased as the potential increased. It should be noted that the determination of the energy band gap is seriously affected by the fitted range of the photon axis in this method.

3.5 Summary

In this chapter, the electrical and optical properties of Cu_2O, depending on deposition conditions, such as solution pH, solute concentration, deposition potential, and temperature, was discussed.

It was found that the solution pH controls the flat band voltage, which determines the conduction type of Cu_2O. Flat band voltage of the Cu_2O increases positively as the pH of the deposition solution increases. It seems that the variation of the flat band voltage by solution pH is related to oxygen incorporation in the film, which is controlled by the amount of oxygen precursor, OH^-, in the solution. Hence, the high pH in the solution is more preferable in producing a p-type Cu_2O with copper vacancy, while the low pH in the solution is more preferable in producing an n-type Cu_2O with oxygen vacancy or copper interstitial.

Polycrystalline p-type Cu_2O cathodically deposited in an aqueous solution containing 0.4 M copper sulfate and 3 M sodium lactic shows resistivity between 3.2×10^5 ohm-cm and 2×10^8 ohm-cm, depending on deposition conditions. The crystal orientation and grain size are suggested to have significant roles in controlling the resistivity of p-type Cu_2O. N-type Cu_2O deposited in a solution containing 0.01 M copper acetate and 0.1 M sodium acetate exhibits higher resistivity than p-type Cu_2O deposited at pH 13 by two orders of magnitude. The lowest resistivity of 5×10^7 ohm-cm is obtained at solution pH 6.4.

It was also found that the band gap of Cu_2O is not sensitive to the deposition conditions such as solution pH and deposition voltage. It is believed that controlling of the band gap in Cu_2O is made possible by the change of the lattice constant by putting a different type of atom in the lattice.

CHAPTER 4

FABRICATION AND CHARACTERIZATION OF ELECTRODEPOSITED CUPROUS OXIDE P-N HOMOJUNCTION SOLAR CELLS

4.1 Introduction

The high cost of silicon solar cells forces the development of new photovoltaic devices utilizing cheap and non-toxic materials prepared by energy-efficient processes [82]. Cuprous oxide (Cu_2O) is potentially attractive for solar cell applications as the absorber layer due to its direct band gap of around 2 eV, high absorption coefficient, material abundance, non-toxicity and low-cost fabrication. However, our poor understanding about intrinsic point defects, difficulty in doping, and the absence of n-type Cu_2O have impeded the development of Cu_2O-based solar cells. Over the past three decades, Cu_2O-based solar cells have been fabricated with metal-Cu_2O Schoktty junctions and p-n heterojunctions such as n-CdO/p-Cu_2O, n-ZnO/p-Cu_2O, and ITO/p-Cu_2O. The highest conversion efficiency with Cu_2O as the active layer is around 2% with a p-n heterojunction structure, while the theoretical efficiency for Cu_2O solar cells is about 19%. It is generally accepted that a p-n homojunction of Cu_2O is the best way to increase the efficiency of Cu_2O-based solar cells.

From the previous chapter, it was found that solution pH can control the flat band voltage, which determines the conduction type of electrochemically deposited Cu_2O, and the crystal orientation and grain size have important roles in controlling the resistivity of Cu_2O. Hence, it is suggested that consecutive electro-deposition of p- on n- Cu_2O or n- on p- Cu_2O for the formation of a p-n junction is made possible by controlling the deposition solution pH.

In this chapter, the material properties of indium tin oxide (ITO) as transparent conductive oxide (TCO) layer are examined first, because ITO was used as the window layer in a Cu_2O solar cell. With the optimized deposition conditions for ITO and Cu_2O, p-n homojunction

Cu_2O solar cells with two different structures, substrate and superstrate were fabricated by an inexpensive two-step electrochemical deposition process. Also, the device thermal reliability and the key factors which affect device performance were investigated.

4.2 Indium Tin Oxide (ITO) Deposition

Indium tin oxide (ITO) is an n-type oxide semiconductor with a wide band gap around 3.5 eV. It has a resistivity of the order of 10^{-4}ohm-cm and a high transmittance of over 80% in the visible range [83, 84].

ITO thin films have been widely used as one of the transparent conductive oxides (TCO) in the field of optoelectronic devices such as solar cells, electroluminescence, and liquid crystal displays (LCDs) [85, 86] because of its high transparency and its low resistivity. Especially in a solar cell, ITO works as a transparent window layer, which means it allows light to pass through it to the active light-absorbing material beneath. Also, it works as an electrical contact layer, which serves as an ohmic contact to harvest photo-generated charge carriers from the light-absorbing material. Hence, the high transmittance and the low resistivity of ITO are required for the highly efficient solar cells.

To date, many techniques, such as evaporation [87], DC/RF sputtering [88], CVD [89], and spray pyrolysis [90] have been developed to deposit ITO films. In many cases the ITO layer in thin film solar cells are deposited by magnetron sputtering, which is a fast deposition technique easily scalable to large areas.

In the fabrication of a Cu_2O solar cell, ITO was used as the window layer to increase the probability of carrier collection. In the case of the substrate structure cell, ITO was deposited on the top of the n-Cu_2O layer as the window layer, while n-Cu_2O was deposited on the top of the ITO/glass substrate in the case of the superstrate structure cell. Hence, it was necessary to characterize the material property of ITO and to tune the deposition condition before the real device fabrication for high efficient devices. Dependency of the transmittance and resistivity on deposition condition will be mainly discussed here.

The AJA RF-sputter machine was used for the deposition of the ITO film. A Target for the ITO deposition was purchased from Kurt J. Lesker. It was composed of 90 % In_2O_3 and 10 % SnO_2 by weight. Argon and Oxygen were used as a working and a reactant gas, respectively. The gas flow rate, the RF power, the working pressure, and the deposition time were mainly used as deposition parameters and controlled by an automatic computer-programmed system. The ITO films prepared by the RF sputtering were characterized by a Vecco four-point probe for the sheet resistance measurement and with a Jasco spectrophotometer for transmittance measurement.

Table 4.1 shows the deposition rate and the electrical characteristics of as-grown ITO films deposited at various deposition conditions. It was found that the deposition rate of ITO films decreased as the flow rate of the reactant oxygen gas increased, and the sheet resistance of ITO increased dramatically as the flow rate of oxygen increased. At the oxygen flow rate above 1sccm, the sheet resistance measurement was impossible, due to the high resistivity of as-deposited ITO films.

Table 4.1 Electrical characteristic of as-grown ITO films depending on various sputtering deposition conditions: The deposition pressure was fixed to 5 mtorr

Sample #	RF power (W)	Ar flow (sccm)	O_2 flow (sccm)	Deposition time (minutes)	Thickness (nm)	Sheet resistance (Ω/□)	Resistivity (Ω-cm)
1	100	30	6	40	115	Non measurable	
2	100	30	3	40	175	Non measurable	
3	100	30	1	40	213	23300	0.496
4	100	30	0.5	25	150	400	0.006
5	100	30	None	40	230	57.6	0.001
6	120	30	0.5	34	245	145	0.003

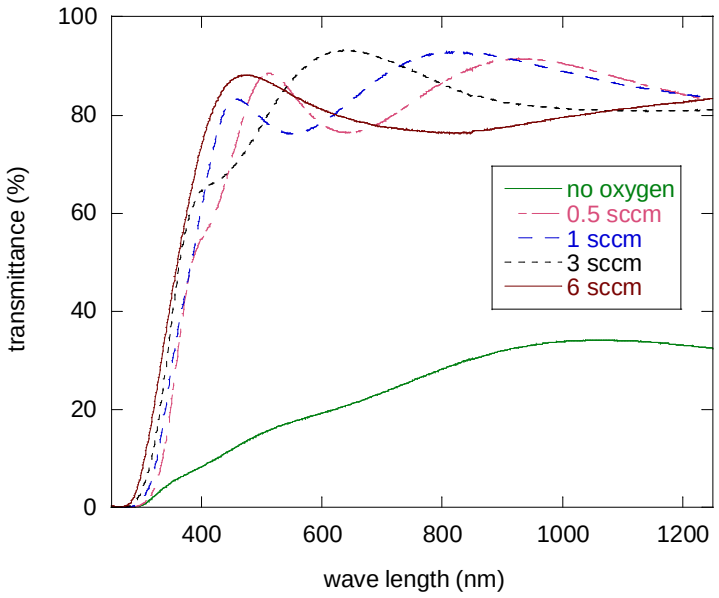

Figure 4.1 Dependency of transmittance of ITO on oxygen flow rate during sputtering deposition

The variation of transmittance of ITO films deposited at different oxygen flow rates is shown in Figure 4.1. As the oxygen flow rate increases, the onset point of transmittance of ITO shifts to the lower wavelength region. In the case of ITO deposited at the oxygen flow rate 0.5 sccm, the onset point of transmittance was 305 nm, while the onset point of transmittance was 282 nm in the case of ITO deposited at the oxygen flow rate 6 sccm. This indicates that the band gap of ITO increases as the oxygen flow rate increases. This result was confirmed by the change of the color in the ITO film depending on the oxygen flow rate. As the oxygen flow rate decreased, the color of the ITO film became darker, which indicated that the energy band-gap of ITO decreased.

The variation of sheet resistance of ITO film, sample #3 in table 4.1, annealed at different temperatures is shown in Figure 4.2. The annealing of ITO films was performed in a vacuum atmosphere under 10^{-5} torr in our home-built thermal chamber at a temperature range from 200 ^{o}C to 400 ^{o}C, and the annealing duration at each temperature was 20 minutes. It was found that the sheet resistance of 23300 Ω/□ of as-grown ITO film dropped down to 28 Ω/□ after

the annealing process at 400 ^{o}C

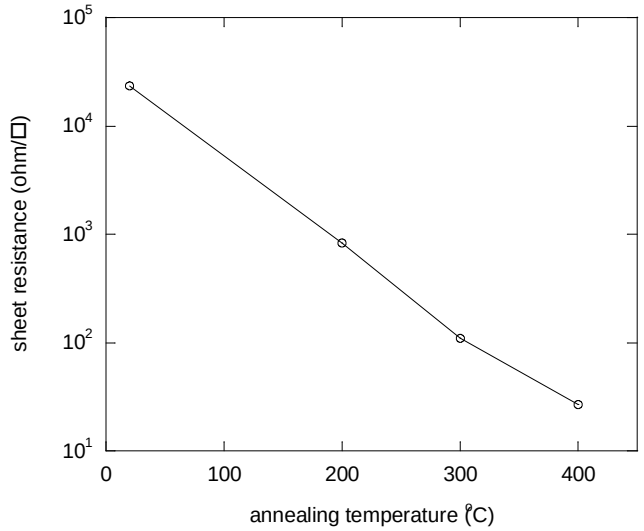

Figure 4.2 Dependency of sheet resistance of ITO film on annealing temperature

Based on electrical and optical characteristics of ITO depending on deposition condition, the oxygen flow rate of 0.5 sccm was chosen for the ITO deposition as the window layer in Cu_2O solar cells. Also, the thermal annealing of ITO was performed to obtain the best quality of ITO thin films only in the superstrate Cu_2O solar cell.

4.3 Electrochemically Deposited Cu_2O p-n Homojunction Solar Cell with Substrate Structure

4.3.1 Experimental

The deposition of p- and n-type Cu_2O was potentiostatically carried out without stirring. A traditional three-electrode electrochemical cell was used, where the counter electrode was a Pt foil and the reference electrode was Ag/AgCl/sat. NaCl. The working electrode for cell fabrication was 100 nm Au/ 75 nm Cr/glass substrate. The Cr layer was used as the adhesion layer for Au. Both the Au and Cr layers were deposited by an AJA e-beam evaporator. The size of the working electrode was 1.2×3.7 cm^2. Prior to deposition, the Au/Cr/glass substrate was ultrasonicated in acetone for 15 minutes and then rinsed in deionized water.

To make a p-n homojunction, p- and n-type Cu_2O films were sequentially deposited in two different electrolyte solutions. A 2 um p-type Cu_2O film was first electrochemically deposited

on a Au-coated Cr/glass substrate in an aqueous solution containing 0.4 M copper sulfate and 3 M sodium lactate at a solution pH 13.0, a deposition potential of -0.3 V, and a deposition temperature of 70 ℃. A 0.5 um n-type Cu_2O film was directly deposited on a p-type Cu_2O in an aqueous solution containing 0.01 M copper acetate and 0.1 M sodium acetate at a solution pH range from 5.2 to 6.4, a deposition potential of -0.1 V, and a deposition temperature of 60 ℃. The size of the deposited Cu_2O layer was 1.2×2.5 cm^2.

For window layer deposition, 100 nm ITO was deposited on the n-type Cu_2O by reactive RF sputtering. The RF power and the deposition pressure were 100 W and 5 mtorr, respectively. The flow rate of oxygen, a reactive gas, was 0.5 sccm in the chamber during the deposition. The device fabrication was finished by DC sputtering of Al for top contact. The finished devices were 1×1 mm^2 and 4×10 mm^2 in size. The performance of the devices was investigated with a newport solar simulator calibrated at AM 1.5. The I-V data was obtained with a Keithley 2601 SourceMeter.

4.3.2 Characteristics of Cu_2O p-n Homojunction Solar Cell with Substrate Structure

The prepared Cu_2O p-n homo junction solar cell with substrate structure is shown in Figure 4.3. There are three junctions formed in this structure: (1) hetero-junction between the ITO and n-Cu_2O, (2) p-n homojunction between the n-Cu_2O and the p-Cu_2O, and (3) Schottky junction between the p-Cu_2O and the Au.

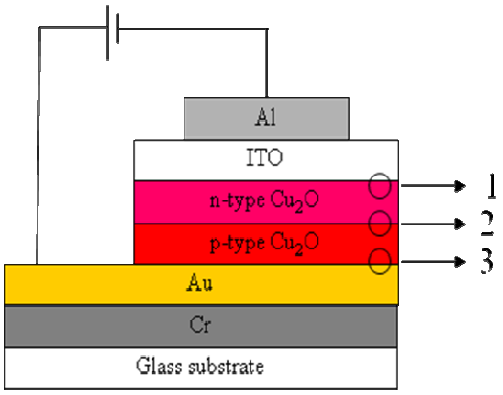

Figure 4.3 Sample structure of electro-deposited p-n homojunction Cu_2O solar cell with substrate structure

Before I-V characterization of the solar cells, the behavior of junction 1, 3 were investigated in advance to confirm the formation of a Cu_2O p-n junction. In order to check the junction 1, a different sample with Au/ p-Cu_2O/ Au structure, shown in Figure 4.4, was prepared. Circular Au electrodes with areas of 2.2×10^{-3} cm^2 were thermally deposited on the top surface of p-type Cu_2O. I-V measurements were performed between two Au electrodes. As shown in Figure 4.5, the interface between Au and p-type Cu_2O shows nice ohmic behavior.

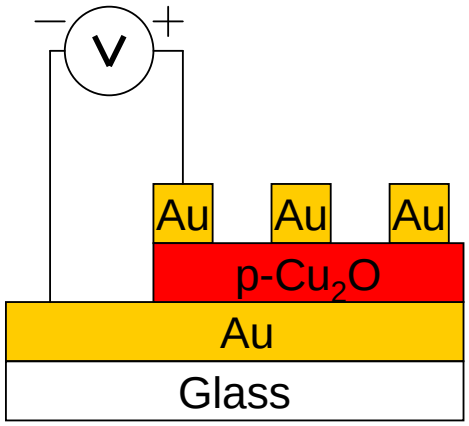

Figure 4.4 Sample structure for the analysis of junction between the Au and the p-Cu_2O

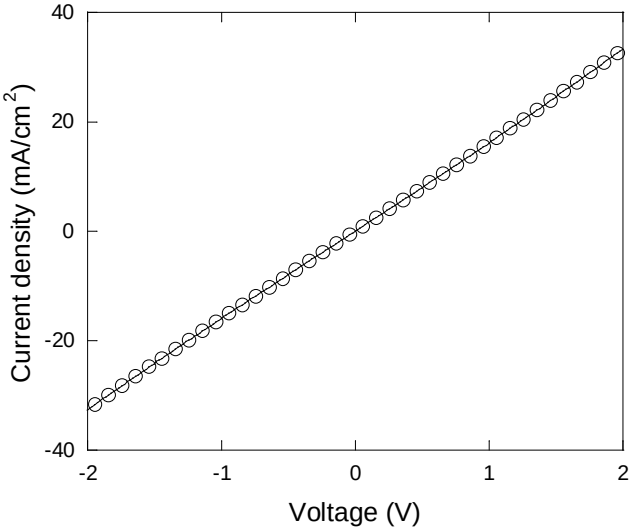

Figure 4.5 I-V Characteristic between the Au and the p-Cu_2O

In order to examine the interface between n-type Cu_2O and ITO, another sample with an ITO/ n-Cu_2O/ ITO structure, shown in Figure 4.6 was prepared. The bottom ITO film was prepared by RF sputtering on a glass substrate and then n-type Cu_2O was electrochemically deposited on the ITO-coated substrate at the deposition potential of -0.1 V, the deposition temperature of 60 ℃, and the solution pH of 5.2. T op ITO pads with an area of 0.25 cm^2 were deposited on n-type Cu_2O by RF sputtering. Finally, Al dots with sizes of 2.2×10^{-3} cm^2 were evaporated on both top and bottom ITO films for electrical contacts. As shown in Figure 4.7, the interface between n-type Cu_2O and ITO also shows ohmic nature. Therefore, any rectification in I-V characteristics from the structure in Figure 4.3 should come from the p-n homojunction in Cu_2O.

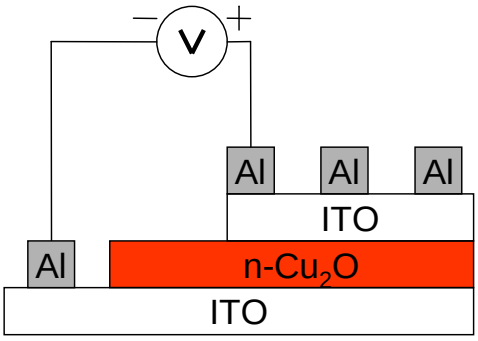

Figure 4.6 Sample structure for the analysis of junction between the ITO and the n-Cu_2O

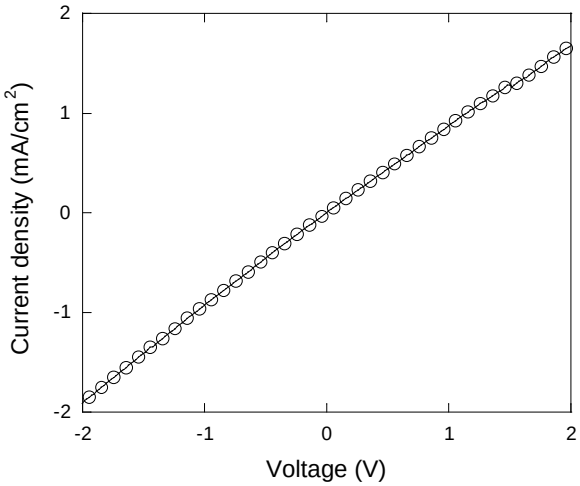

Figure 4.7 I-V characteristic between the ITO and the n-Cu_2O

Dark I-V characteristics of Cu_2O p-n homojunction substrate solar cells with areas of 1×1 mm^2 are shown in Figure 4.8. P-Cu_2O and n-Cu_2O were deposited in solutions of pH 13.0 and pH 5.2, respectively. This shows a typical rectification effect of a p-n junction. It represents the successful formation of a p-n homojunction in the device. The photovoltaic performance of a p-n homojunction Cu_2O solar cell is shown in Figure 4.9. The short-circuit current, open-circuit voltage, fill factor, and conversion efficiency are determined to be 1.23 mA/cm^2, 0.32 V, 0.353, and 0.102 % respectively under AM1.0.

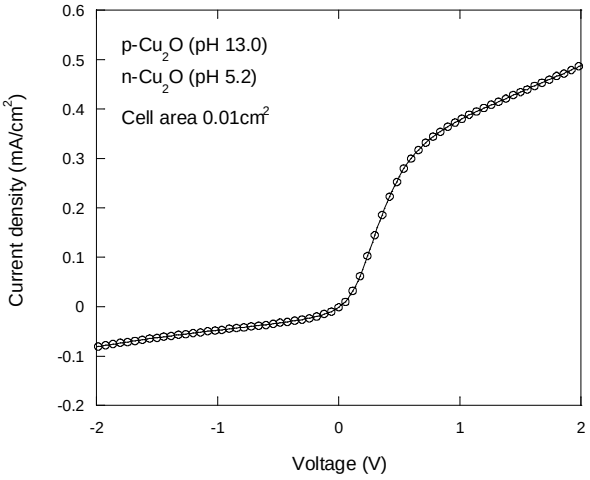

Figure 4.8 Dark I-V characteristic of Cu_2O p-n homojunction substrate solar cell with area of 0.01cm^2

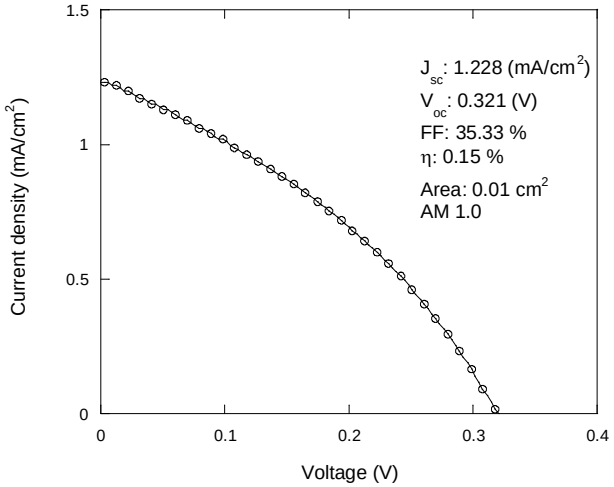

Figure 4.9 Photo I-V characteristic of Cu_2O p-n homojunction substrate solar cells with area of 0.01cm^2

From the photocurrent measurement, already discussed in chapter 3.3.2, it was found that the flat band voltage (V_{fb}) of p-Cu_2O deposited at solution pH 13.0 was 0.05 V and V_{fb} of n-Cu_2O deposited at solution pH 5.2 was -0.46 V. The difference between these two V_{fb}, 0.51 V, times the electron charge, *e*, is equal to the Fermi-energy difference between the p-type Cu_2O and the n-Cu_2O. The Fermi-energy difference is equally shown as built-in potential, eV_{bi} in the p-n homojunction. In the solar cell, open circuit voltage, V_{oc}, can be as high as built-in potential, V_{bi}. However, it is normally smaller than the built-in potential, due to several parasitic series and shunt resistances. Therefore, the open circuit voltage, 0.32 V, is a reasonable value. Nonetheless, it should be pointed out that some of the shunt paths exist in the Cu_2O p-n homojunction solar cell. The obtained open-circuit voltage is slightly higher than reported that of an n-ZnO/p-Cu_2O heterojunction cell [15].

Dark I-V characteristics of Cu_2O p-n homojunction solar cells, in which p-Cu_2O and n-Cu_2O were deposited at solution pH 13.O and pH 6.4 respectively are shown in Figure 4.10. It shows a lower rectification ratio than a Cu_2O solar cell, in which n-Cu_2O was deposited at solution pH 5.2.

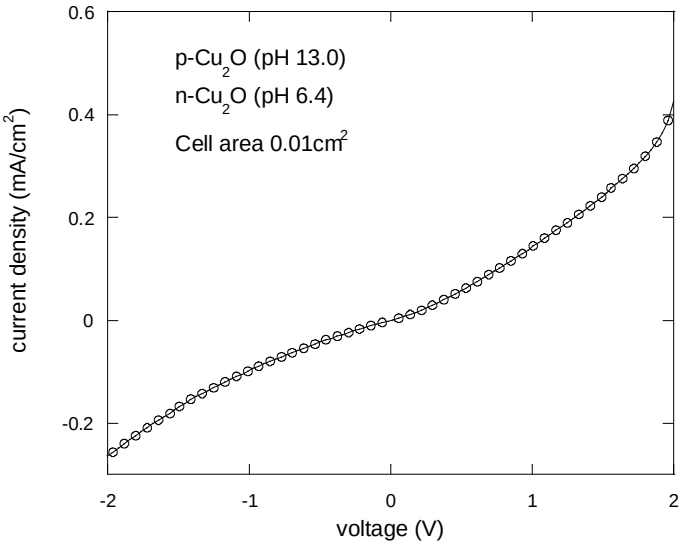

Figure 4.10 Dark I-V characteristic of Cu_2O p-n homojunction solar cells, which have n-Cu_2O deposited at a solution pH 6.4

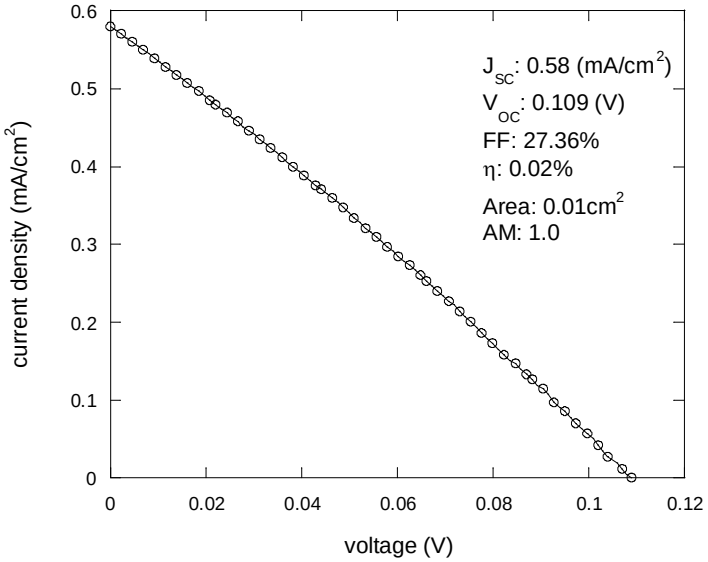

Figure 4.11 Photo I-V characteristic of Cu_2O p-n homojunction solar cells, which have n-Cu_2O deposited at a solution pH 6.4

The photovoltaic performance of this cell is shown in Figure 4.11. The short-circuit current, open-circuit voltage, fill factor, and conversion efficiency are determined to be 0.58 mA/cm^2, 0.109 V, 0.273, and 0.02%, respectively under AM 1.0. From the photocurrent measurement, it was found that V_{fb} of Cu_2O is significantly affected by deposition solution pH. It is speculated that the decreased V_{oc} in the cell is caused by change of the n-Cu_2O material property due to increased solution pH 6.4.

After the successful fabrication of a Cu_2O homojunction substrate solar cell, it was realized that the cell size should be increased in order to check the scale-up feasibility of the Cu_2O solar cell. Cu_2O solar cells with areas of 0.4 cm^2 as compared to the previous cell with area of 0.01 cm^2 were fabricated with the same deposition method and condition, as described in 4.3.1. The top view of this cell, with an Al top electrode in the shape of three fingers, is shown in Figure 4. 12.

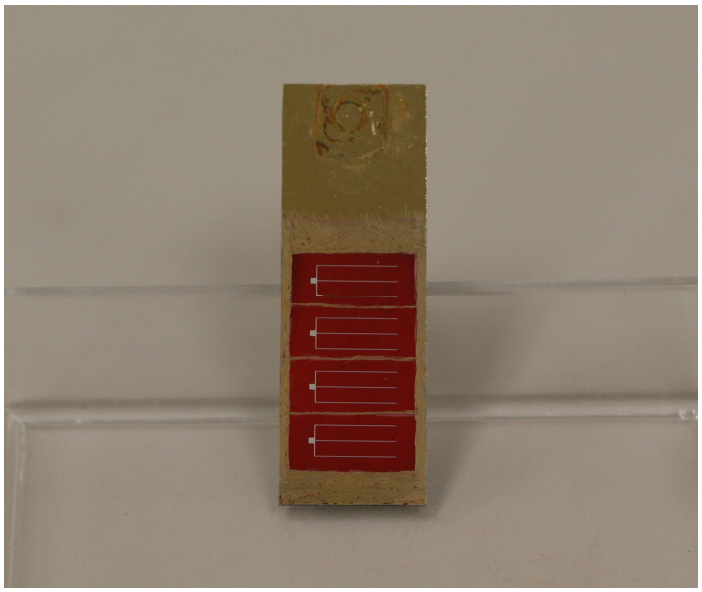

Figure 4.12 Real top view of the Cu_2O p-n homojunction substrate solar cell with area of 0.4 cm^2: four individual cells are shown

The dark I-V characteristic of an enlarged Cu_2O cell with area of 0.4 cm^2 is shown in Figure 4.13. Dark current density was higher than in the small cell, due to top electrode and cell size. The figure also shows the rectification effect and the current rectification ratio, around 1 to 3, was obtained at voltages between the -2 V and the 2 V.

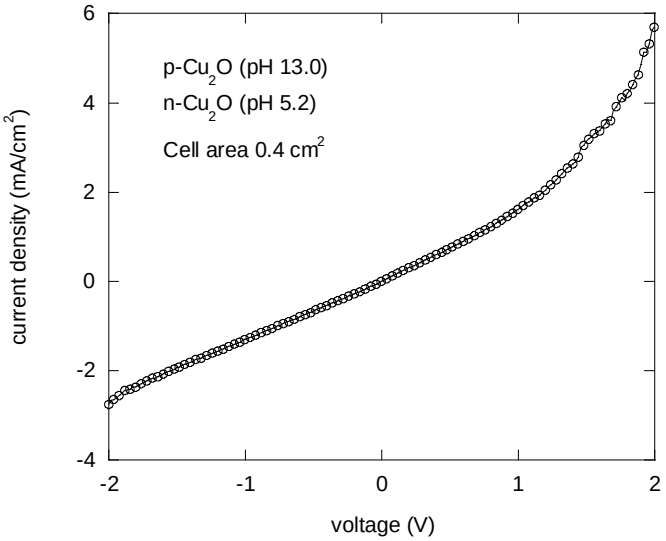

Figure 4.13 Dark I-V characteristic of Cu_2O p-n homojunction substrate solar cell with area of 0.4 cm^2

The performance of an enlarged solar cell is shown in Figure 4.14. It showed that its efficiency was 10 times lower than that of the small cell with area of 0.01 cm^2. It also showed that V_{oc} decreased dramatically.

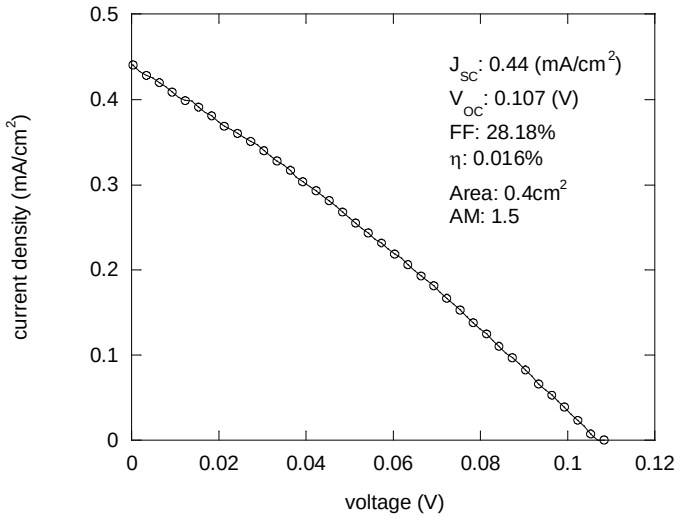

Figure 4.14 Photo I-V characteristic of Cu_2O p-n homojunction substrate solar cell with area of 0.4 cm^2

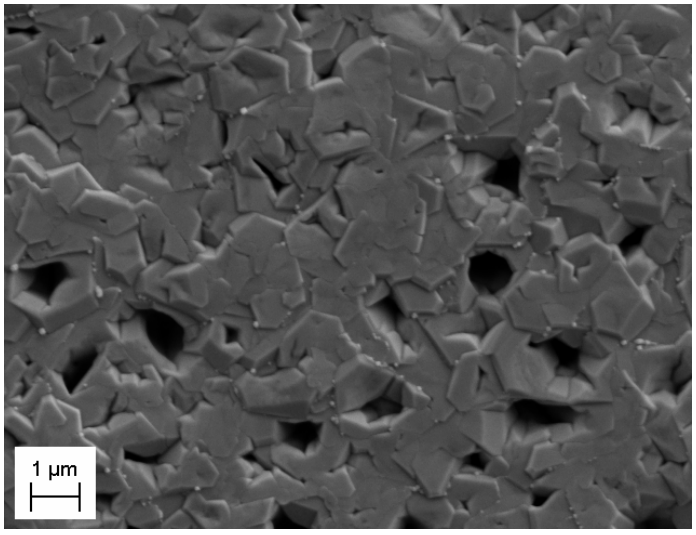

Figure 4.15 SEM surface image of the 0.5 um n-Cu_2O layer after deposition on 2 um p-Cu_2O/Au

Before the ITO deposition, the surface morphology of as grown n-Cu_2O on p-Cu_2O/Au stack was examined by SEM. It was found that several pin-holes were formed in n-Cu_2O during electrodeposition, as shown in Figure 4.15. It is believed that ITO deposition into these pin holes produced a shunt path in the device, and this deteriorated the device performance in the enlarged cell.

A thermal reliability test was performed on the enlarged Cu_2O substrate solar cell, shown in Figure 4.14. The cell was annealed in the air at 150 ^oC and 300 ^oC for 20 minutes in each step. The open circuit voltage decreased from the 107 mv to 74 mv, and the short circuit current also decreased from the 0.44 mA to 0.36 mA at annealing temperature 150 ^oC, as shown in Figure 4.16. At 300 ^oC there was no photovoltaic effect in the cell. It is believed that point defects of different types in each type of Cu_2O diffused each other at temperatures below 150 ^oC, and then this annihilated the formation of p-n junction.

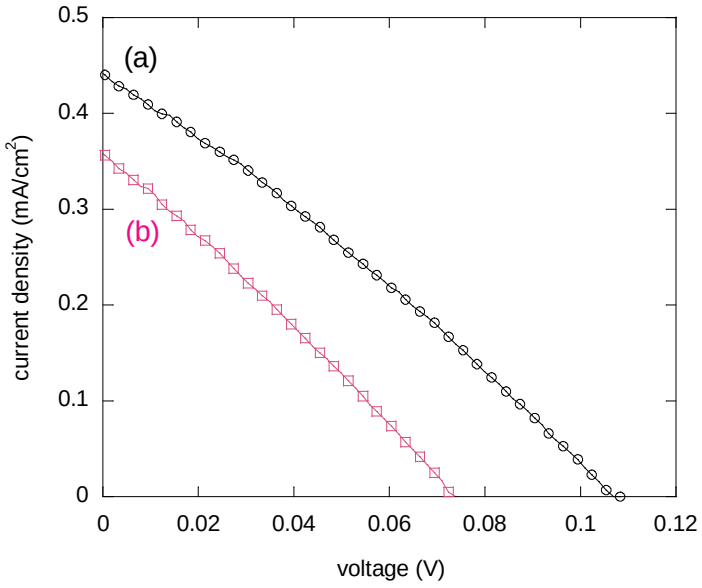

Figure 4.16 Performance change of Cu_2O substrate solar cell with area of 0.4 cm^2 after thermal treatment at (a) room temperature and (b) 150 ^oC in air for 20 minutes

The overall low short-circuit current and the low conversion efficiency in the Cu_2O substrate solar cell are attributed primarily to the high resistivity of both p- and n-type Cu_2O, as

well as to the non-optimized device structure. Hence, a different structure, called a superstrate structure, of a Cu_2O p-n homojunction solar cell was introduced. It will be discussed in following section.

4.4 Electrochemically Deposited Cu_2O p-n Homojunction Solar Cell with Superstrate Structure

4.4.1 Experimental

300 nm ITO on a glass substrate was used as a working electrode in the electrodeposition for the fabrication of the Cu_2O solar cell with superstrate structure. Prior to ITO deposition, the glass substrate was ultrasonicated in acetone for 15 minutes, and then it was rinsed in deionized water. ITO was deposited on the glass substrate by reactive RF sputtering. The RF power and the deposition pressure were 100 W and 5 mtorr, respectively. The flow rate of oxygen, a reactive gas, was 0.5 sccm in the chamber during the deposition. After sputtering deposition, as-grown ITO films were annealed in a vacuum atmosphere of under 10^{-5} torr at 400 ^{o}C for 40 minutes to achieve the minimum sheet resistance of around 30 Ω/□. The counter electrode was a Pt foil, and the reference electrode was Ag/AgCl/sat. NaCl in a traditional three-electrode chemical cell. The deposition of n- and p-type Cu_2O was potentiostatically carried out without stirring.

To make a p-n homojunction, n- and p-type Cu_2O films were sequentially deposited in two different electrolyte solutions. 0.8 um n-type Cu_2O films were first electrochemically deposited on a ITO/glass substrate in an aqueous solution containing 0.01 M copper acetate and 0.1 M sodium acetate at the solution pH 5.2, the deposition potential -0.1 V, and the deposition temperature of 60 ℃. Then p-Cu_2O films with different thickness were directly deposited on n-Cu_2O in an aqueous solution containing 0.4 M copper sulfate and 3 M sodium lactate at the solution pH 13.0, the deposition potential -0.5 V, and the deposition temperature of 60 ℃. The size of the deposited Cu_2O layer was 1.2×2.5 cm^2.

For the back contact, which acts as the reflector layer as well, 100 nm Au was deposited on the p-type Cu_2O by thermal evaporator. The back Au electrode was a round

shaped dot with a 0.6 cm diameter, which determines the cell size of 0.282 cm^2. Then copper wire was bonded on the Au electrode as an electrical contact.

The performance of the devices was investigated with a Newport solar simulator calibrated at AM 1.5. The I-V data was obtained with a Keithley 2601 SourceMeter.

4.4.2 Characteristics of Cu_2O p-n Homojunction Solar Cell with Superstrate Structure

The term superstrate refers to a solar cell configuration where the glass substrate is not only used as the supporting structure, but also as a window for the illumination and as part of the encapsulation. In the structure, the actual solar cell materials are deposited above the glass. In the finished device, there is no need for a second glass plate for the encapsulation, while there is such a need in the case of the substrate solar cells. Calculations of solar cell production costs showed that the electronic materials and the glass plates are roughly the same cost [91]. Thus, superstrate solar cells have the potential of lower production cost compared to substrate solar cells.

The side view and top view of the fabricated Cu_2O superstrate solar cell are shown in Figure 4.17 and Figure 4.18, respectively.

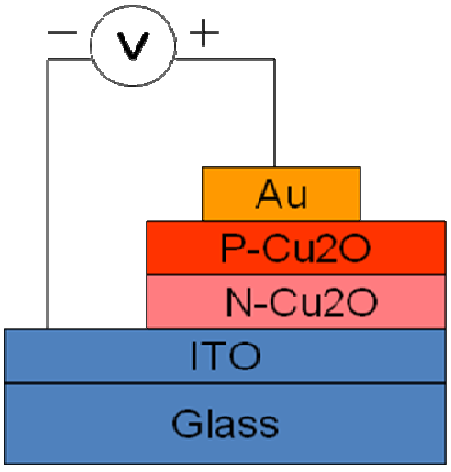

Figure 4.17 Structure of the fabricated Cu_2O superstrate p-n homojunction solar cell

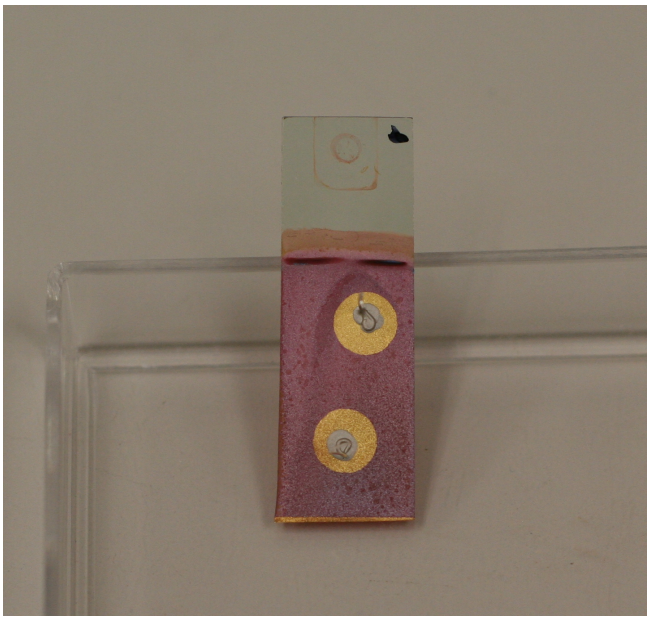

Figure 4.18 Top view of the fabricated Cu_2O superstrate p-n homojunction solar cell: two individual cells are shown

The first advantage of the superstrate structure of the Cu_2O solar cell is that there is no light loss by metal electrode shadow, while there is such a loss in the case of substrate solar cells. This structure normally results in more photocurrent in the device. Another advantage of the superstrate structure of the Cu_2O solar cell is that thermal annealing of ITO film can be performed before Cu_2O deposition to obtain low sheet resistance and high transparency, which affect the cell performance. From the thermal reliability test of the Cu_2O substrate solar cell, it was found that the efficiency of the cell droped down from the annealing temperature of 150 ℃. Therefore, thermal annealing of the ITO layer at 400 ℃ to obtain the lowest sheet resistance was impossible in the substrate structure.

In the superstrate Cu_2O solar cell, the thickness of n-Cu_2O was increased to 0.8 um by controlling deposition time in order to obtain better uniformity of the n-Cu_2O layer on ITO. The Dark I-V characteristic of the Cu_2O superstrate solar cell, which has 3 um p-Cu_2O on 0.8 um n-Cu_2O, is shown in Figure 4.19. The rectification ratio was almost two times higher than that of the Cu_2O substrate cell with a size of 0.4 cm^2.

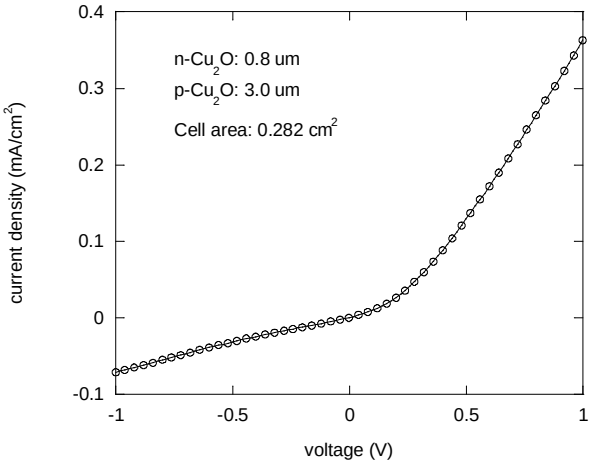

Figure 4.19 Dark I-V characteristic of Cu_2O p-n homojunction superstrate solar cell with area of 0.282 cm^2

The solarcell performance of the superstrate Cu_2O cell is shown in Figure 4.20. Compared to the Cu_2O substrate cell, the overall solar cell performance was improved. Especially, V_{oc} was improved the most, and the highest V_{oc} of 185 mV was obtained in the superstrate cell with 3um p-Cu_2O. It is believed that shunt paths in the Cu_2O superstrate cell are less than the substrate cell, resulting in higher V_{oc} in the superstrate cell. The reduced I_{sc} in the superstrate cell was caused by the increased thickness, 0.8 nm, of the high resistive n-Cu_2O layer.

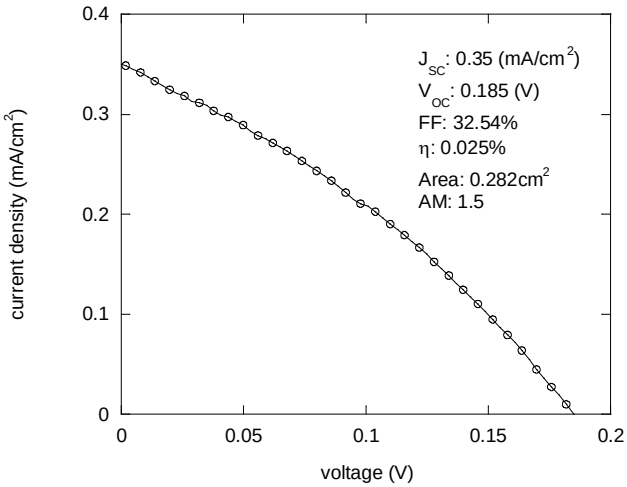

Figure 4.20 Photo I-V characteristic of Cu_2O p-n homojunction superstrate solar cell with an area of 0.282 cm^2

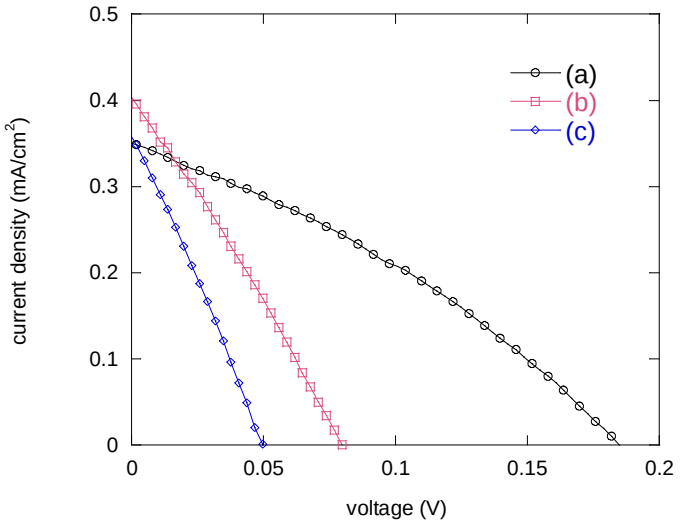

Figure 4.21 Performances of the superstrate Cu_2O solar cell, which has (a) 3.0 um p-Cu_2O, (b) 1.5 um p-Cu_2O, and (c) 0.8 um p-Cu_2O as the absorber layer: n- Cu_2O is fixed to 0.8 um

The superstrate Cu_2O solar cells, which have different thickness, 3.0, 1.5, and 0.8 um of p-Cu_2O, were prepared to observe the effect of p-Cu_2O thickness on device performance. The thickness of n- Cu_2O was fixed to 0.8 um. The open circuit voltage of the superstrate cell linearly increased as the thickness of the p-Cu_2O layer increased, while the short circuit current remained similar, as shown in Figure 4.21. This is a typical case of shunt effect. It was found that surface roughness of the superstrate cell was larger than the substrate cell, probably caused by a thicker n-Cu_2O layer in the superstrate cell. It is speculated that on the rough surface of n-Cu_2O, more shunt paths, such as non-covered n-Cu_2O, will be more likely to be formed as the thickness of p-Cu_2O decreases. It was noticed that around 3 um thick p-Cu_2O was necessary to form good quality of junction in the superstrate structure cell.

4.5 Summary

In this chapter, the fabrication and characteristics of electrochemically deposited Cu_2O p-n homojunction solar cells are discussed. Based on the theory that bath pH can control the conduction type and the amount of native point defects in electrodeposited Cu_2O, the sequential

electrodeposition of n on p-Cu_2O and p on n-Cu_2O were proposed, and two different structures of a Cu_2O p-n homojunction solar cell were successfully fabricated from a two-step electrodeposition.

In the Cu_2O substrate solar cell with size of 0.01 cm^2, the highest efficiency of 0.15 % was achieved. It showed an open circuit voltage of 321 mV, a short circuit current of 1.228 mA, and a fill factor of 35.33 %. It was found that the open circuit voltage of the device was related to the bath pH of n-Cu_2O. More effort has been made to increase the cell size, and there was success in fabricating a larger Cu_2O substrate solar cell with a size of 0.4cm^2. It showed an efficiency of 0.016 % and a open circuit voltage of 107 mV. The lowed open circuit voltage of the cell indicates that more shunt paths exist in the larger device, and several pin holes in n-Cu_2O are considered as main contributors to the formation of shunt paths. The thermal reliability test shows that the device performance of the Cu_2O solar cell is not stable above the temperature of 150 ^oC.

Overall, the Cu_2O superstrate solar cell shows better device performance than the Cu_2O substrate cell with a size of 0.4 cm^2. The efficiency of 0.025 % was obtained from the superstrate Cu_2O solar cell, which has 3 um p-Cu_2O and 0.8 um n-Cu_2O. It was found that the efficiency of the superstrate cell is proportional to the thickness of the p-layer, and 3 um p-Cu_2O is required to minimize shunt effect.

Generally, the low short-circuit current and the low conversion efficiency in the Cu_2O solar cell are primary caused by the high resistivity of both p- and n-type Cu_2O. Hence, doping in both p- and n-Cu_2O to reduce their resistivities is necessary for better efficiency. To our knowledge, this is the first report of success in fabricating a p-n homojunction Cu_2O solar cell.

CHAPTER 5

N-TYPE DOPING IN ELECTRODEPOSITED CUPROUS OXIDE

5.1 Introduction

Cuprous oxide (Cu_2O) is a promising material for low-cost solar cells. The source materials for Cu_2O are naturally abundant. It can be deposited with inexpensive solution-based techniques such as dip coating and electrodeposition. Its direct band gap of 2.0 eV, ease of material preparation, and environmentally friendly material properties have attracted much attention in fabricating Cu_2O based photovoltaic devices since the 1920's.

Cu_2O is known as a defect semiconductor with p-type conductivity due to Cu vacancies. Therefore, previous photovoltaic devices based on Cu_2O as the absorber layer have been metal/Cu_2O Schottky junctions or p-n heterojunctions. Recently, the n-type behavior in electrodeposited Cu_2O was reported. The invention of n-type Cu_2O makes it feasible to fabricate a p-n homojunction Cu_2O solar cell, considered to be the best way to increase the efficiency of the Cu_2O -based solar cell.

As discussed in chapter 4, the conduction type of Cu_2O and the amount of point defect in Cu_2O was controlled by solution pH. The consecutive electrodeposition of n-Cu_2O on p-Cu_2O and p-Cu_2O on n-Cu_2O was achieved from the each different deposition solution with different pH. Finally, p-n homojuction Cu_2O solar cells were newly fabricated.

The conversion efficiency of the p-n homojunction Cu_2O solar cells was low at ~0.15%, which was attributed to the high resistances of both n-type and p-type Cu_2O. Therefore, doping in both n-type and p-type Cu_2O is required to improve the efficiency. Some doping attempts in Cu_2O were reported in the past, such as Cl [92)] and N [93] as p-type dopants. It was also reported that Cl can be used as an n-type dopant in Cu_2O by co-precipitation during electrodeposition [94].

In this chapter, two n-type doping techniques, thermal diffusion doping and electrodoping, are introduced, and their effects on electrical and structural properties of Cu_2O are mainly discussed.

5.2 N-Type Doping in Electrodeposited Cu_2O by Cu Diffusion

5.2.1 Experimental

300 nm Cu films were thermally deposited on glass substrates by thermal evaporation as the working electrode for the electrodeposition of Cu_2O and as the source for Cu diffusion. Prior to electrodeposition, the Cu/glass substrates were sonicated in acetone and rinsed in deionized water for cleaning.

Electrodeposition of Cu_2O was conducted in an aqueous solution containing 0.4 M copper sulfate and 3 M sodium lactate. The pH of the solution was adjusted to 7.5 by adding 4 M sodium hydroxide. A traditional three-electrode electrochemical cell was used, where the counter electrode was a Pt foil and the reference electrode was Ag/AgCl/sat. NaCl. The working electrode was Cu-coated glass substrate. The deposition temperature was kept at 60 ℃, and a constant voltage of -0.2 V vs. Ag/AgCl/sat. NaCl was applied for 1 hour. The thickness of the deposited Cu_2O films was measured by an Alpha Step IQ surface profiler and was found to be around 320 nm. All the chemicals used were reagent grade.

After Cu_2O deposition, the diffusion annealing of the Cu_2O/Cu stack was performed under a vacuum of 10^{-5} torr at temperatures of 100~400 ℃ for 10 minutes. The sample temperature was controlled by a Heat Wave Labs temperature control unit. The sample heating rate was 1.5 ℃/sec, while the cooling rate was 0.2 ℃/sec. The resistivity of annealed Cu_2O films was measured by a simple two-probe method. Before resistivity measurements, Cu dots of 220 um in diameter were deposited on annealed Cu_2O/Cu samples by thermal evaporation. A voltage was applied between the Cu film on the substrate and the Cu dot on the Cu_2O film, and the current was recorded with an Agilent 4155C semiconductor parameter analyzer at room

temperature. The resistivity of annealed Cu_2O films was extracted from the slope of the current-voltage relation, i.e. the resistance, the area of Cu dot, and the thickness of the Cu_2O film.

Photocurrent measurements of the annealed Cu_2O/Cu samples were performed in a three-electrode cell, where the counter electrode was a Pt wire, the reference electrode was Ag/AgCl/saturated NaCl, and the working electrode was a Cu_2O/Cu sample facing to the incident light. An aqueous solution of 0.5 M Na sulfate was used as the electrolyte. The light source was a 150-W Schott ACE broad-spectrum halogen lamp. The crystallinity of the annealed Cu_2O/Cu samples was examined with a Siemens D-500 powder diffractometer using Cu K_α radiation. The surface morphology of the samples was determined by a Zeiss Supra 55 scanning electron microscope with a beam voltage of 5 kV.

5.2.2 Material Characteristics of Cu Doped Cu_2O Films

Our motivation in this study was based on the idea that the concentrations of native point defects in Cu_2O, such as Cu interstitials or O vacancies, can be changed by Cu diffusion as a point defect source under vacuum, and the change in the nature and concentration of native point defects will change the electrical properties of Cu_2O.

Thermodynamically, Cu_2O is decomposed into cupric oxide (CuO) above 300 °C in air [95]. In order to avoid CuO formation and to examine Cu diffusion into Cu_2O, all the samples were annealed under a vacuum of 10^{-5} torr. Figure 5.1 shows the XRD spectra of electrodeposited Cu_2O on Cu which were exposed to thermal annealing at temperatures of 100 ~ 400 ℃ for 10 minutes. All the XRD spectra indicated that only pure Cu_2O existed in the annealed samples and the annealed Cu_2O films had a preferred crystal orientation of (111) with a weak (220) orientation. It was noticed that the XRD spectra for all samples do not show differences in peak position. However, the intensities of the Cu_2O peaks slightly increased as the annealing temperature increased.

The average grain size of the annealed Cu_2O/Cu samples at temperatures of 100~400 ℃ was estimated by the Debye-Scherrer formula,

$$d = \lambda / (L \cdot \cos\theta) \tag{5.1}$$

where λ is the wavelength (1.54 Å for Cu K_α line), L is the angular line width at half maximum intensity, and θ is the Bragg angle. The calculation shows that the average grain sizes of as-grown Cu_2O/Cu samples and annealed Cu_2O/Cu samples at 400 ℃ are 24.4 nm and 36.6 nm, respectively, which were confirmed by SEM measurements.

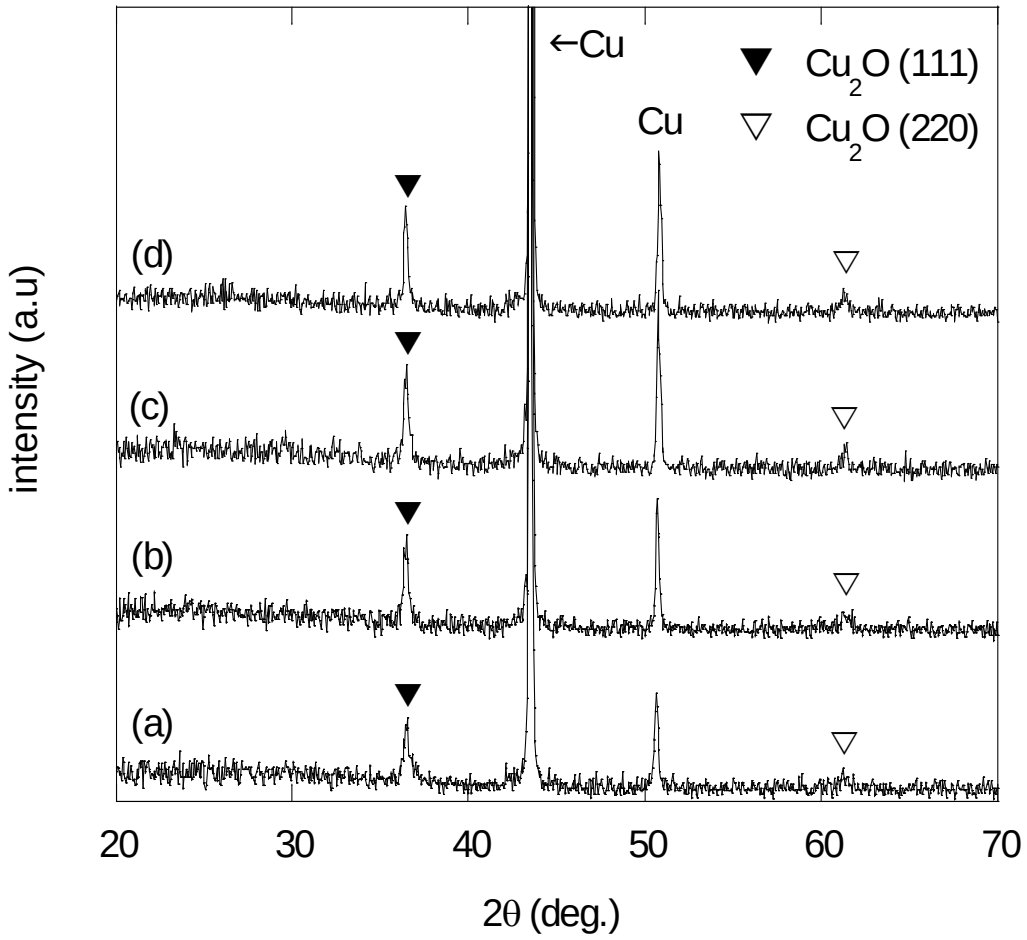

Figure 5.1 X-ray diffraction patterns of the Cu_2O/Cu stack exposed to thermal annealing at (a) as grown, (b) 150 ℃, (c) 250 ℃ and (d) 400 ℃.

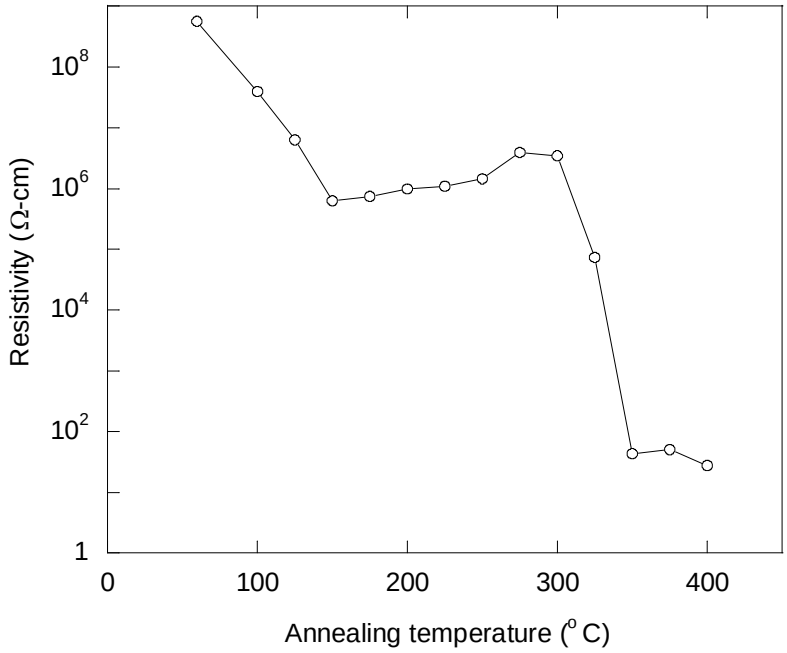

Figure 5.2 Resistivity of annealed Cu_2O samples on Cu as function of annealing temperature. Resistivity at 60 ℃ is given by the as-grown sample.

Figure 5.2 shows the resistivity of the annealed Cu_2O films on Cu at temperatures from 100 to 400 ℃. It is noticed that the resistivity of annealed Cu_2O gradually decreases at low temperatures and is then more or less stable between 150 and 300 ℃. Above 300 ℃, the resistivity suddenly decreases again, which may correspond to the onset of Cu diffusion into Cu_2O. The lowest resistivity of 28 Ω-cm is obtained at 400 ℃. It is believed that Cu diffusion into Cu_2O is the main cause for the resistivity to drop over 6 orders of magnitude, even though the enlarged grain size of Cu_2O by thermal annealing may affect the electrical properties of Cu_2O as well.

It is known that diffusion of impurities in polycrystalline materials takes place along two channels. One is the grain boundary where the diffusion probability of an impurity is much higher than in the lattice, and thus diffusion occurs at low temperatures. The other is the lattice where diffusion occurs at relatively high temperatures and at much slower rate [96]. It is speculated that Cu diffusion in Cu_2O occurs mainly along the grain boundary. This is because

the annealing temperatures of 100~400 ℃ are relati vely low compared to the melting point of Cu_2O, 1235 ℃.

The diffusion direction of an impurity in a lattice is largely determined by the lattice distortion caused by the impurity atom, which constitutes a barrier to impurity atoms coming into the lattice [96]. The lattice distortion in Cu_2O is different along different crystal planes, because the each group of crystal planes, (100), (110) and (111) in Cu_2O, has a different plane distance of 0.427, 0.603 and 0.738 nm, respectively. Hence, it is believed that grain boundary diffusion is dominant at the beginning of the annealing process along the (100) plane, and then lattice diffusion is followed along the (111) plane.

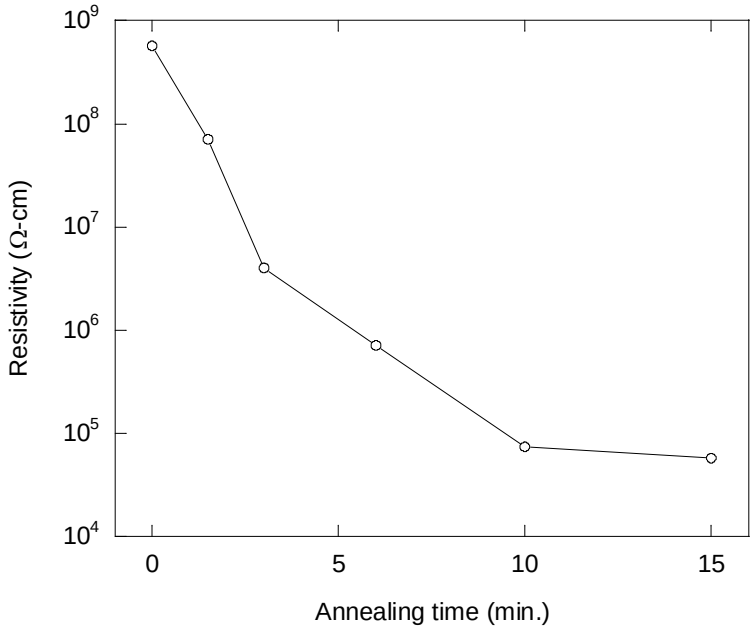

Figure 5.3 Dependency of resistivity of annealed Cu_2O samples on annealing time at annealing temperature of 325 ℃

The resistivity of Cu_2O annealed at 300 ℃ as a function of annealing tim e is presented in Figure 5.3. It is noticed that the resistivity of Cu_2O rapidly decreases at the beginning and then is saturated after 10 min. The following equation was used for the estimation of the effective diffusion coefficient of Cu in Cu_2O [97],

$$\frac{R(t)-R(0)}{R(\infty)-R(0)}=\frac{C(t)-C(0)}{C(\infty)-C(0)}=1-\frac{8}{\pi^2}\sum_{n=0}^{\infty}\frac{1}{(2n+1)^2}\exp\left[\frac{-(2n+1)^2\pi^2 Dt}{l^2}\right] \quad (5.2)$$

where C(t) and R(t) are the concentration of diffused Cu into Cu_2O and the resistance of the Cu_2O film as a function of annealing time t, and C(∞) and R(∞) are the final concentration of diffused Cu into Cu_2O and the final resistance of the Cu_2O film after a long annealing. R(0) is the initial resistance of the Cu_2O film. *l* is the thickness of the Cu_2O film. The diffusion coefficient of Cu in Cu_2O at 325 ℃ was estimated to be 1.91×10^{-16} m^2 / sec for n = 0~5 and R(∞) = R(15min) by the above equation. It has been reported that the diffusion coefficient of O in Cu is 3.53×10^{-31} m^2/sec at 325 ℃ [98]. The calculated O diffusion len gth into Cu for 10 minutes is 1.78×10^{-5} nm, while the Cu diffusion length into Cu_2O for same duration is 340 nm. Therefore, it is suggested that the change in Cu_2O resistivity is mainly due to Cu diffusion into Cu_2O rather than O diffusion from Cu_2O into Cu substrate.

In order to confirm the conduction type of the Cu-diffused Cu_2O samples, photocurrent measurements were performed. Figure 5.4 shows the photo and dark currents of an as-grown Cu_2O sample (a) and a Cu-diffused Cu_2O sample annealed at 400 ℃ (b). In the case of the as-grown sample, both anodic and cathodic photocurrents appear in the voltage range from -0.3 to 0.05 V. The flat band voltage (V_{fb}) of -0.11 V was obtained.

However, in case of the Cu-diffused Cu_2O sample, only anodic photocurrent is observed in the same voltage range, and the V_{fb} of -0.29 V was obtained. This indicates that Cu-diffused Cu_2O samples are n-type, and the Fermi energy of Cu_2O is lowered by 0.18 eV. It is speculated that Cu diffused into Cu_2O acts as n-type dopant and contributes to the n-type conductivity by forming n-type point defects such as Cu interstitials or O vacancies in Cu_2O. In addition, the photocurrent of p-Cu_2O is always cathodic in this same voltage range [99].

(a)

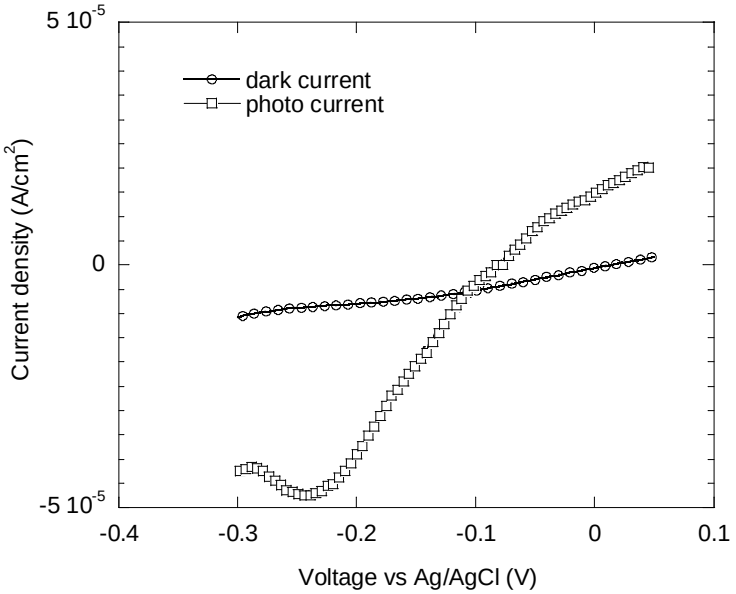

(b)

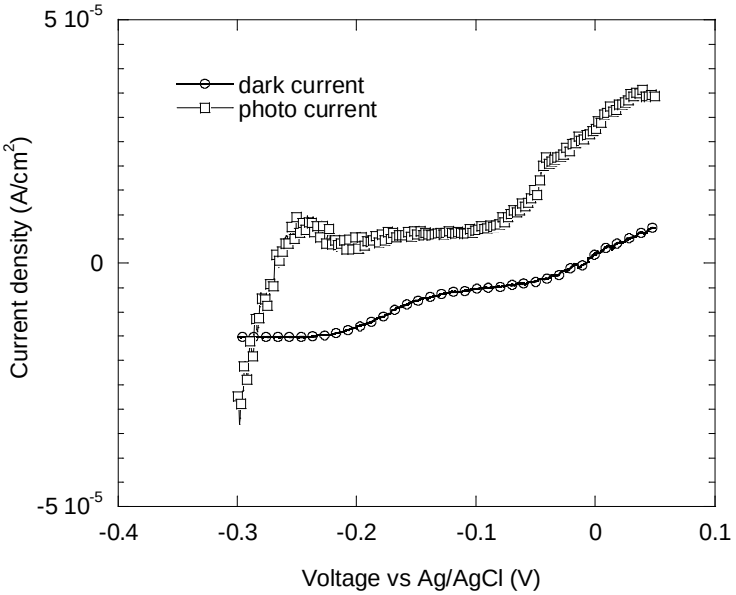

Figure 5.4 Photo and dark currents of (a) as-grown Cu_2O and (b) Cu_2O on Cu annealed at 400 ℃

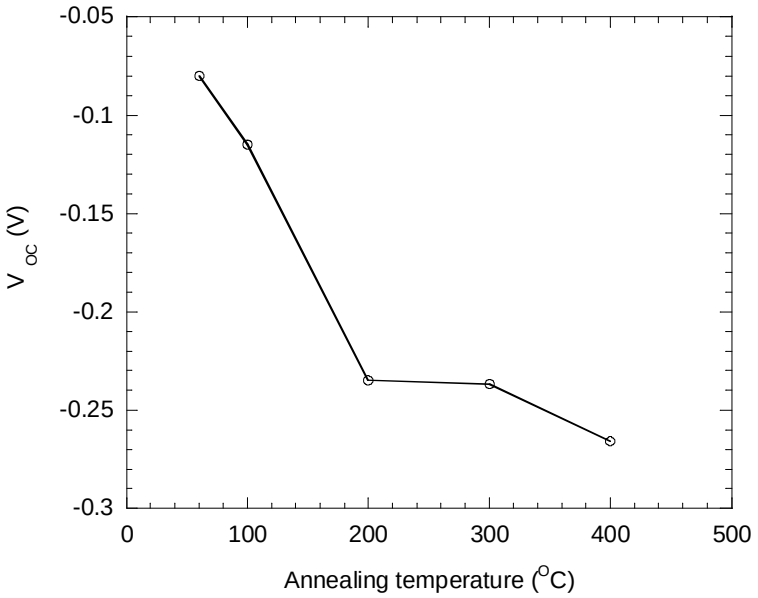

Figure 5.5 Open-circuit voltages of Cu-diffused Cu_2O as a function of annealing temperature. V_{OC} at 60 ℃ is given by the as-grown sample

Figure 5.5 shows the open-circuit voltage (V_{OC}) of the annealed Cu_2O samples on Cu at temperatures of 100~400 ℃. The V_{OC} means the potential when there is no output current under light illumination. It was measured in a standard three-electrode cell with an aqueous solution containing 0.5 M Na sulfate under broad-spectrum light illumination. The V_{OC} negatively increases as the annealing temperature increases, indicating that the n-type property of Cu_2O is improved by Cu diffusion.

5.3 Electrochemical n-type doping in Cu_2O

Doping is a common way to control the electrical properties of a semiconductor. Generally, doping in a semiconductor is accomplished by one of the following methods:

1) Thermal diffusion of a dopant into the semiconductor at high temperatures

2) Ion implantation of a dopant into the semiconductor

3) Co-deposition of a dopant with the semiconductor during vapor deposition

All of these methods are performed at high temperatures of around ~1,000 ºC and in vacuum systems in order to produce high quality of materials. Thus, these methods are energy-intensive and high-cost. One approach to reduce the cost of these doping processes is the use of a solution based process.

In this chapter, two solution-based doping methods are introduced in order to achieve n-type Cu_2O and to control its resistivity. The doping mechanism is believed to be the co-deposition of the n-type dopant with Cu_2O.

In the electrodoping in Cu_2O, a substitutional dopant can go into either Cu sites or O sites. Since Cu has one valence electron and O has six valence electrons in Cu_2O, potential n-type dopants can be group VII elements for the O sites and group II elements for the Cu sites.

First, Zn in the group II elements was selected as a potential n-type dopant for cation substitution, because the ionic radii of Zn^{2+} is 0.74 Å, which is well matched to the Cu^{2+} ionic radii of 0.72 Å. Also, Zn electronegativity of 1.65 in the Pauling scale is close to the Cu electronegativity of 1.90. The down side of Zn as a dopant is the different crystal structure of its oxide form. Cu_2O has a cubic crystal, while ZnO has a hexagonal one.

Second, Br in the group VII elements was chosen as an n-type dopant for anion substitution because of its ionic radii as well as the low solubility of CuBr in water. This will be discussed later.

5.3.1 Preliminary Study about N-type Electrochemical Doping in Cu_2O with Zn

The Zn doping experiment was performed in a traditional three-electrode chemical cell. The three-electrode electrochemical cell included a Pt counter electrode, a Ag/AgCl/saturated NaCl reference electrode, and a ITO coated glass substrate as the working electrode with a typical dimension of 1×4 cm^2. Prior to electrodeposition, the ITO coated glass substrates were sonicated in acetone for 15 minutes and then rinsed with deionized water.

The basic plating solution contained 5 mM copper sulfate and 100 mM zinc sulfate. The deposition bath temperature was maintained at 60 ^{o}C. All electrodeposition baths were sparged

with ultrapure O_2 for 30 minutes prior to use, and an O_2 overpressure was maintained during film deposition. In some cases, N_2-saturated media were also used. All the chemicals used were reagent grade. The films were grown by the potentiostatic deposition method. The deposition potential was controlled from 0 to -0.4 V versus the Ag/AgCl/saturated NaCl reference electrode and the deposition duration was 30 minutes.

X-ray diffraction patterns of the samples were obtained by a Siemens D-500 powder diffractometer using Cu K_α radiation. A Zeiss Supra 55 scanning electron microscopy was used to characterize surface morphology and grain size of the samples.

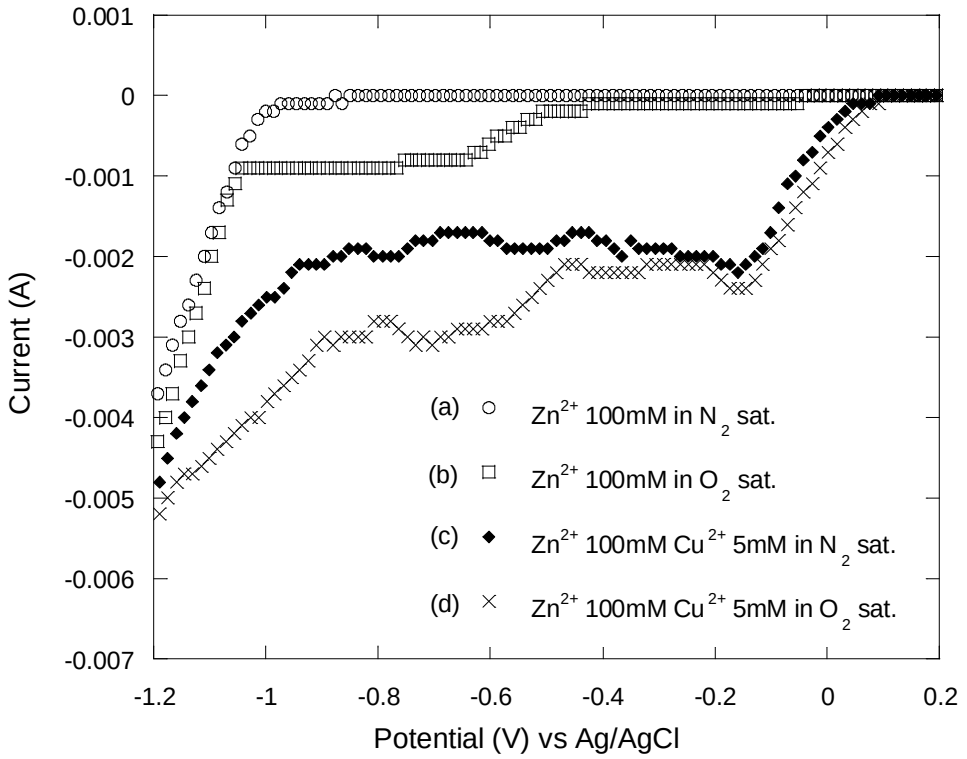

Figure 5.6 Voltammograms of solution compositions as shown on ITO working electrode

The linear voltametric curves of the given solution are shown in Figure 5.6. Considering Figure 5.6 (a) in the presence of Zn^{2+} and N_2, large cathodic current flow was obtained at around -970 mV, which is assigned to the deposition of metallic Zn. In the presence of dissolved

O_2 in the electrolyte, the deposition potential for metallic zinc shifts to a more negative value of -1050 mV, as shown in Figure 5.6 (b).

The effect of O_2 saturation of the electrolyte medium is shown in Figure 5.6 (b). In the presence of dissolved O_2 in the electrolyte, a cathodic curve is observed with an onset at -50 mV, assigned to the reduction of O_2 and the electrogeneration of OH^-

In Figure 5.6 (c), it was observed that the 1st cathodic current at a voltage of from 100 mV to -150 mV is related to Cu_2O deposition by reaction (5.3). However, the cathodic potential for the generation of OH^- by reaction (5.4) and the generation of Cu by reaction (5.5) were not clearly shown in Figure 5.6 (d). Nevertheless, the produced OH^- ions caused the formation of $Zn(OH)_2$ and Cu_2O by reactions (5.6) and (5.7).

$$2Cu^{2+} + H_2O + 2e^- \rightarrow Cu_2O \downarrow +2H^+ \quad (5.3)$$

$$\frac{1}{2}O_2 + H_2O + 2e^- \rightarrow 2OH^- \quad (5.4)$$

$$Cu^{2+} + 2e^- \rightarrow Cu \downarrow \quad (5.5)$$

$$Zn^{2+} + 2OH^- \rightarrow Zn(OH)_2 \downarrow \quad (5.6)$$

$$Cu^{2+} + 2OH^- \rightarrow Cu_2O \downarrow +H_2O \quad (5.7)$$

Electo-deposition was performed in the solution, shown in Figure 5.6 (d). The XRD measurement indicated that only Cu_2O was produced from 0 to -100 mV, shown in Figure 5.7 (a). The grain size of the Cu_2O larger than 2um was obtained in this condition, shown in Figure 5.8 (a). When the deposition potential was between -150 mV and -300 mV, the XRD spectrum showed that metallic Cu was produced and co-deposited with Cu_2O on the ITO substrate, shown in Figure 5.7 (b). This indicates that the reduction of Cu^{2+} to Cu took place before the reduction of O_2 to OH^- in the given solution. At the applied potential above -300 mV, $Zn(OH)_2$ was produced. This indicates that the reduction of O_2 to OH^- starts from -300 mV in a given solution. As a result, multi-phase thin films of Cu_2O, $Zn(OH)_2$ and Cu on the ITO substrate were

produced from a potential above -300 mV in Figure 5.8 (c). It was found that the reduction of Cu^{2+} to Cu always took place before the reduction of O_2 to OH^- regardless of the molarity of the solute, the deposition temperature, or the O_2 sparging time.

This preliminary study suggests that our goal of producing Zn-doped n-type Cu_2O may be difficult to accomplish by cathodic electrodeposition from an O_2 saturated aqueous 5 mM $CuSO_4$ and an 100 mM $ZnSO_4$ solution. Instead, multi-phase thin films comprising Cu_2O, Cu, and $Zn(OH)_2$ are obtained. Depending on the deposition potential, either Cu_2O, a mixture of Cu and Cu_2O, or a mixture of Cu_2O, Cu and $Zn(OH)_2$ can be obtained.

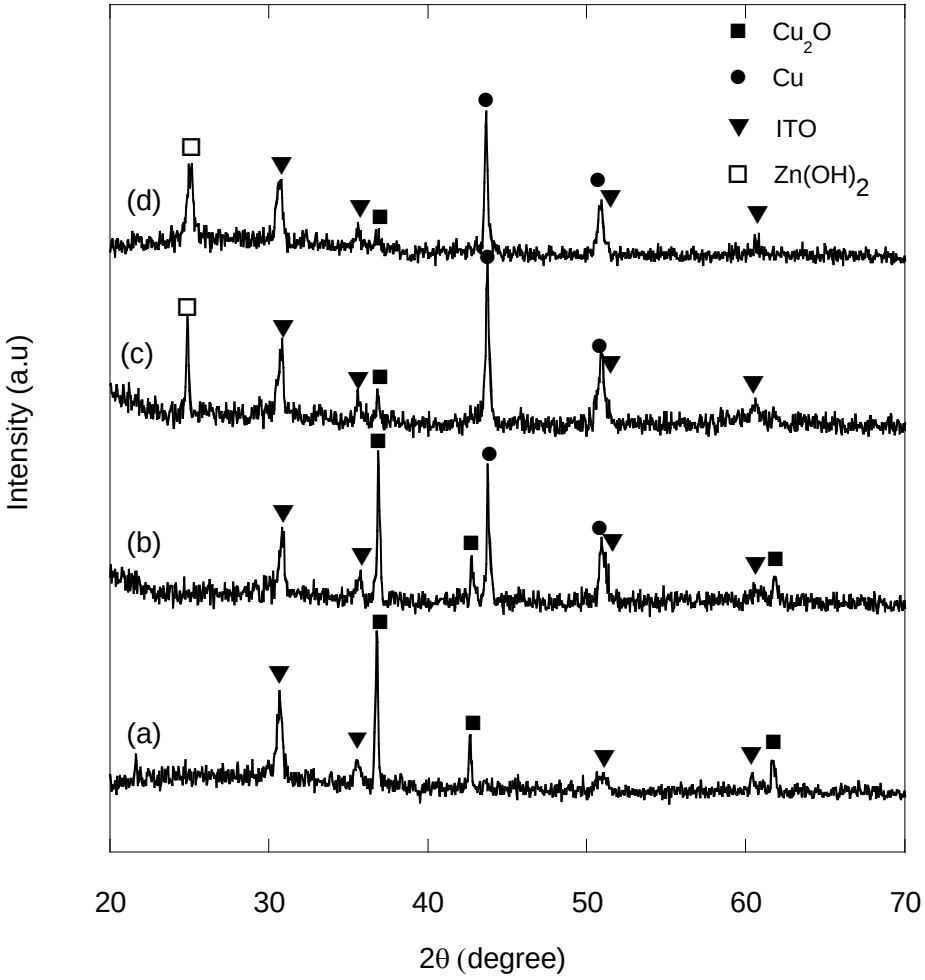

Figure 5.7 XRD spectra of films deposited on ITO substrate at potential (a) -100 mV vs Ag/AgCl/sat. KCl, (b) -200 mV, (c) -300 mV, and (d) -400 mV

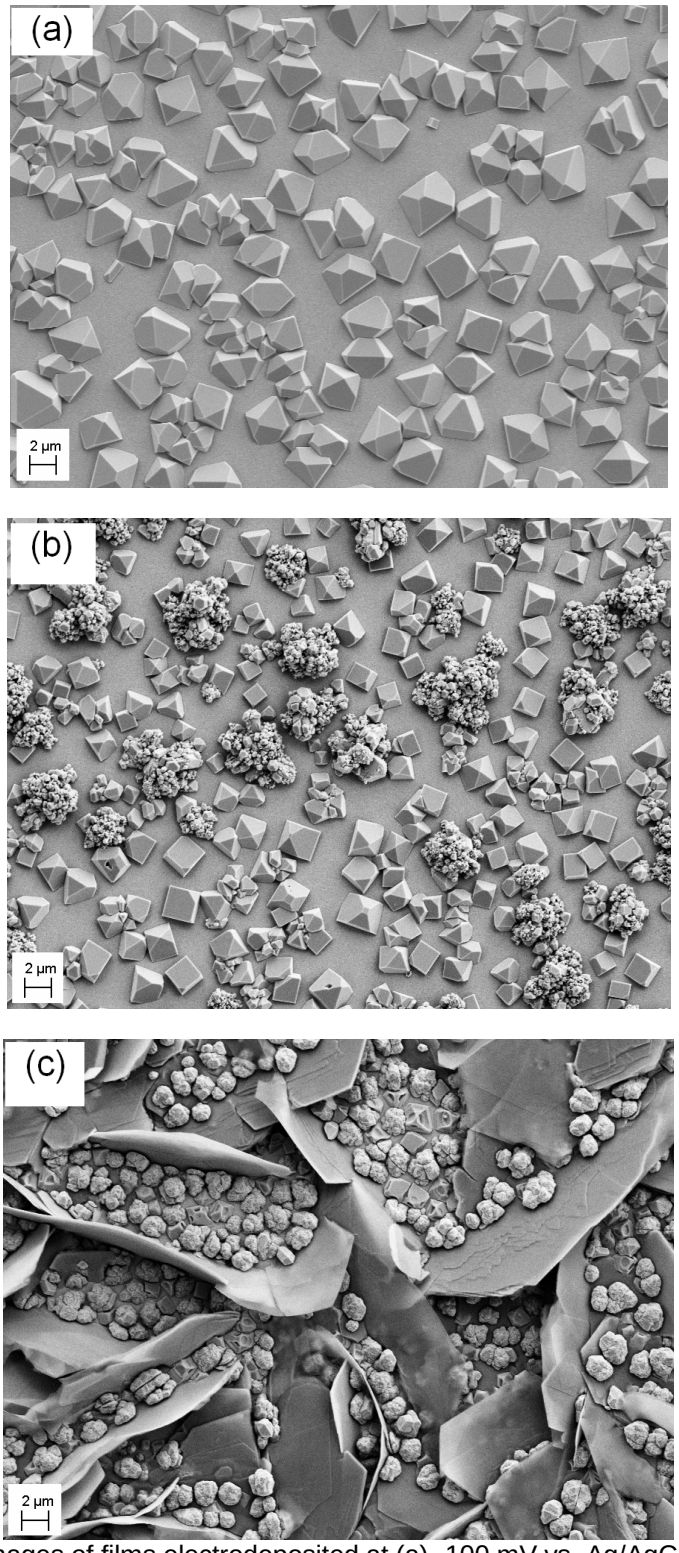

Figure 5.8 SEM images of films electrodeposited at (a) -100 mV vs. Ag/AgCl/sat. KCl, (b) -200 mV, and (c) -300 mV

5.3.2 Electrochemical N-type Doping in Cu_2O with Br

5.3.2.1 Experimental

Electrodeposition was performed in the three-electrode electrochemical cell included a Pt counter electrode, an Ag/AgCl/saturated NaCl reference electrode, and a ITO coated glass substrate as the working electrode. The thickness of the ITO film was 300 nm. It was deposited in an AJA RF sputter. After the sputtering deposition, as-grown ITO films were annealed in a vacuum atmosphere of under 10^{-5} torr at 400 ^{o}C for 40 minutes in order to achieve minimum sheet resistance of around 30 Ω/□. Prior to electrodeposition, the ITO coated glass substrates were sonicated with acetone for 15 minutes and then rinsed with deionized water.

The basic deposition solution contained 0.02 M copper acetate, 0.1 M sodium acetate. Solution pH was fixed to 5.2 adjusted by acetic acid. Sodium bromide (NaBr) was used as the Br precursor. Their mole concentration was changed to control the doping level in Cu_2O. The deposition temperature was fixed to 60 ^{o}C. The deposition time was 1.5 hour. All of the chemicals used were reagent grade.

The thickness of the Cu_2O films was measured with a KLA-Tencor Alpha-Step IQ profilometer. The morphology of the Cu_2O films was analyzed with a ZEISS Supra 55 VP scanning electron microscope with a nominal electron beam voltage of 10 kV. Photocurrent characterization was carried out in a three-electrode electrochemical cell with a broad-spectrum 150 W white lamp shining onto the working electrode. A Pt foil, a Ag/AgCl/saturated NaCl, and the Cu_2O film were used as the counter, reference, and working electrode, respectively. For photocurrent measurements, the solution contained 0.1 M sodium acetate.

To measure the resistivity of Br-doped Cu_2O, circular dots of Cu were deposited as the top electrode by thermal evaporation through a shadow mask. The area of the electrodes was 3.6×10^{-4} cm^2. Current-voltage (I-V) characterization was performed between the top electrode and the ITO film on the substrate with a HP 4155C semiconductor parameter analyzer. From the slope of the I-V relation, which behaved linearly, the resistance of the Cu_2O film was

determined. The resistivity of the Cu_2O film was calculated with its thickness and the area of Cu top electrode.

5.3.2.2 Material characteristics of Br doped Cu_2O

The mechanism of Br doping in Cu_2O is believed to be two individual precipitation reactions in the solution [8]. Cu^{2+} ions are first electrochemically reduced to Cu^{+} ions, which then react with OH^{-} ions in the solution and produce Cu_2O:

$$2Cu^{+} + 2OH^{-} \rightarrow Cu_2O \downarrow + H_2O \tag{5.8}$$

Also direct deposition of Cu_2O from Cu^{2+} is also possible by reaction (5.3). With the presence of Br^{-} ions in the solution, Cu^{+} ions also react with Br^{-} ions to produce CuBr, which incorporates Br into the Cu_2O film, and thus doping the Cu_2O film:

$$Cu^{+} + Br^{-} \rightarrow CuBr \downarrow \tag{5.9}$$

The solubility product constant of CuBr is 6.27×10^{-9} [100], indicating that even small amounts of Cu^{+} and Br^{-} in the solution will react with each other and precipitate.

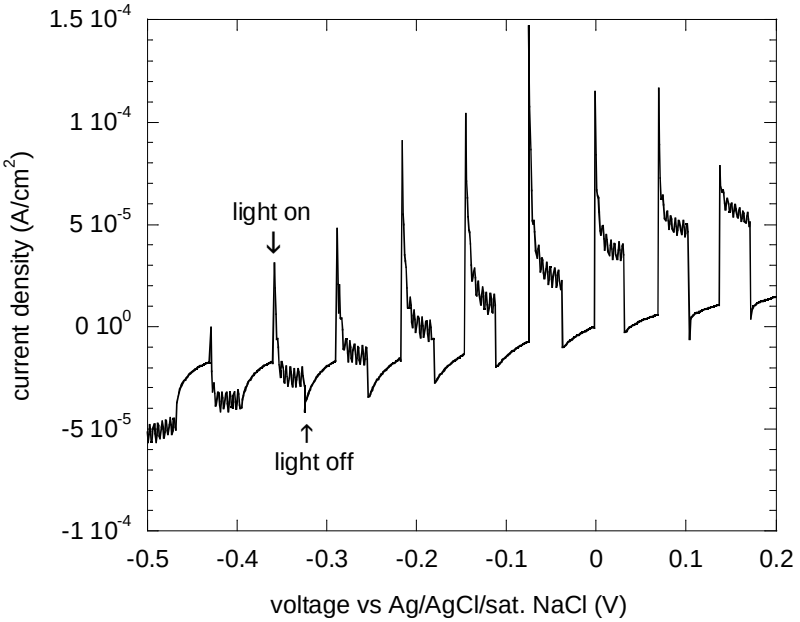

Figure 5.9 Photocurrent of Br doped n-type Cu_2O

In order to confirm the conduction type of the Br-doped Cu_2O samples, photocurrent measurements were performed at voltages between -0.5 and 0.2 V. Photocurrent from Br-doped Cu_2O deposited in the solution with 0.02 M copper acetate, 0.1 M sodium acetate, and 2.5 mM NaBr is presented in Figure 5.9. The anodic current indicated that the film was a n-type semiconductor.

The deposition rate of Br doped Cu_2O depending on Br concentration was examined. As shown in Figure 5.10, the thickness of the Br doped Cu_2O films increased with increasing Br concentration. Basically, crystal growth takes place in two steps: nucleation and growth of grain, which are mainly affected by growth temperature and concentration of electroactive species. At a given temperature and pH, the film thickness is mainly determined by the concentration of electroactive species: Cu^{2+} and Br^-. As the concentration of Cu^{2+} is kept constant for all deposition, the concentration of Br^- is the dominant factor. Hence, film thickness is proportional to the concentration of Br^- ion.

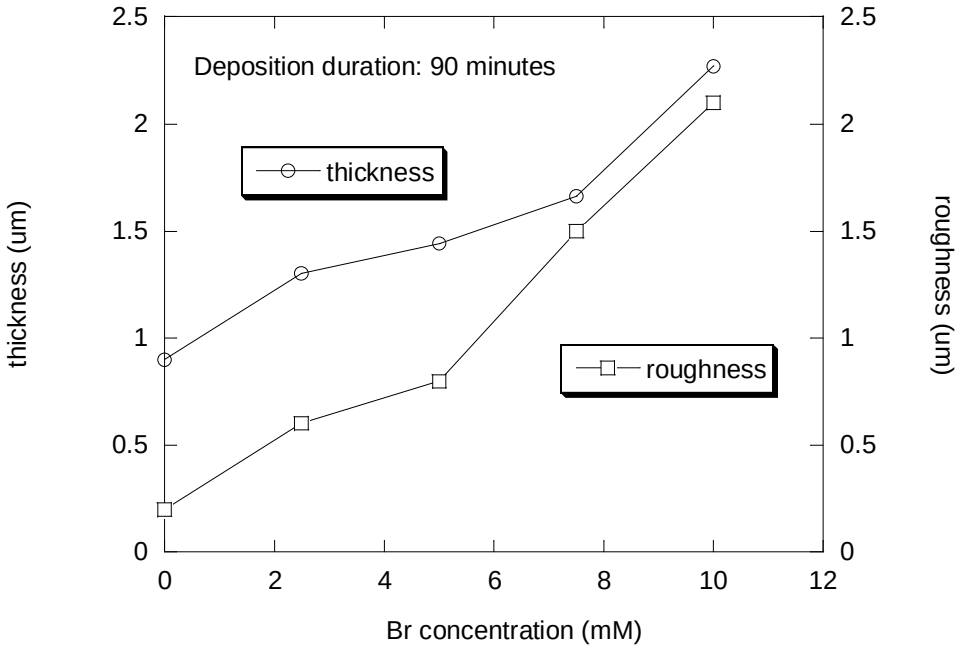

Figure 5.10 Dependency of thickness and roughness of Br doped Cu_2O on Br concentration in the solution

Interestingly, surface roughness of Br doped Cu_2O film also increased with increasing Br concentration. It was found that the roughness of Br doped Cu_2O was caused by the formation of the dendrite crystal in the films.

Generally, the dendritic branching growth in electrodeposition can take place when the deposition rate is increased to form a depletion zone of the reactive ions around a growing crystal [101]. Once the depletion zone is formed, the apexes of a polyhedral crystal, which protrude into the region of higher concentration, grow faster than the central parts of facets. Hence, dendritic branches are formed [102]. Usually, the depletion zone can be formed by increasing either potential or current to the electrode.

The crystal morphology of Cu_2O deposited in solution without Br was shown in figure 5.11. In this medium, there was no sign of dendritic growth. Also, it was found that dendrite of Cu_2O was not formed even when the applied potential was increased to a point that triggers deposition of metallic copper. Instead, cubic crystal with a grain size of ~1.5 um was obtained in this medium. This film showed the surface roughness of ~0.2 um.

When the deposition was performed in the solution with 2.5 mM NaBr, the deposition current density was increased, and dendritic crystals of Cu_2O, shown in Figure 5.12, were produced. No Cu_2O with cubic shapes was observed. This result indicates that the initial deposition rate obtained with 2.5mM Br^- is enough to induce the dendrite growth. From the SEM picture of Figure 5.12, an overall grain size of ~3 um was obtained for the Cu_2O dendrite branch (nucleated site at the beginning of deposition), grown out of the substrate. That caused the roughness of this film to be 0.5 um. As the mol concentration of Br^- increased, the size of the dendritic crystal increased and the nucleation density decreased, as shown in Figure 5.13. The increased crystal size contributes to the larger surface roughness of 1.5 um.

Normally, nucleation density increases when overpotential increases. This overpotential is defined as the difference between the applied potential and the reduction potential of Cu^{2+} to Cu^+. In other words, nucleation density can be increased with increasing current density.

However, in Cu_2O deposition in the solution with Br, nucleation density increased with decreasing current density (decreasing Br^- concentration). It is believed that in the beginning of a nucleation process, the growth rate of the lateral branch increases with increasing Br^- concentration, which hinders more nucleation of Cu_2O on the substrate. Thus, higher Br concentration produces less nucleation density, which causes larger grain size.

One of the most interesting aspects of dendritic crystal growth in Br doped Cu_2O is its anisotropic development of branches. Figure 5.13 shows that the branches grown on the substrate are longer than the branches grown out of the substrate, although four main branches, which are developed from the apexes of a polyhedron, are symmetrical. This is because the ITO substrate is more conductive than Cu_2O crystals, making branches on the substrate grow faster than those growing out of the substrate.

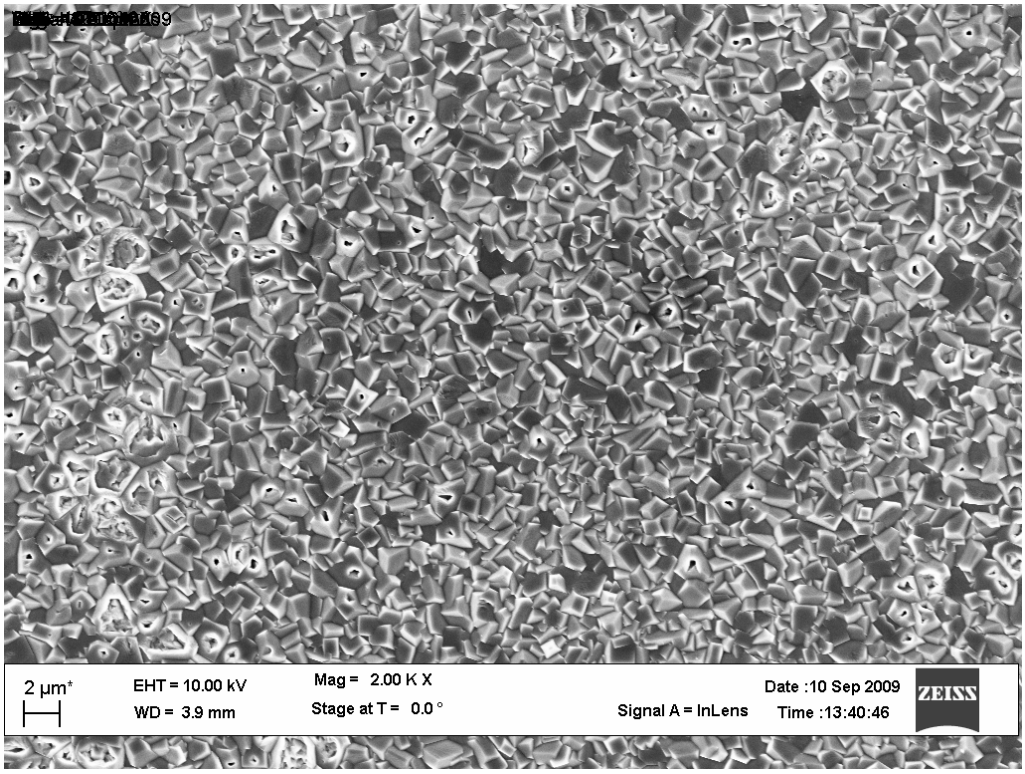

Figure 5.11 Surface morphology of Cu_2O deposited in the solution without NaBr

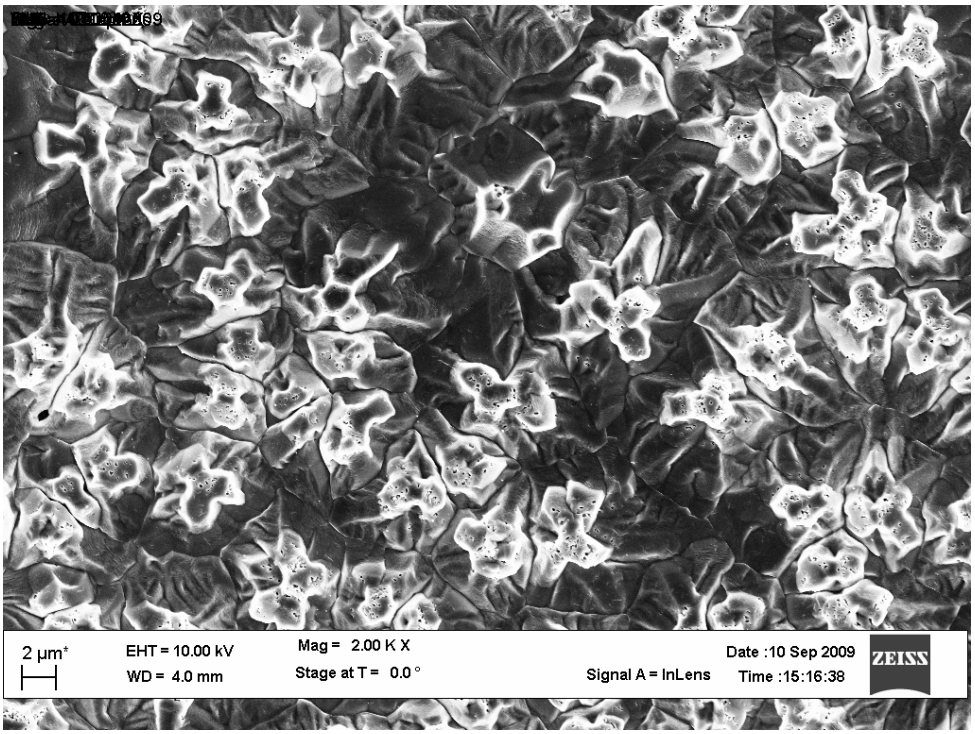

Figure 5.12 Surface morphology of Cu_2O deposited in the solution with 2.5 mM NaBr

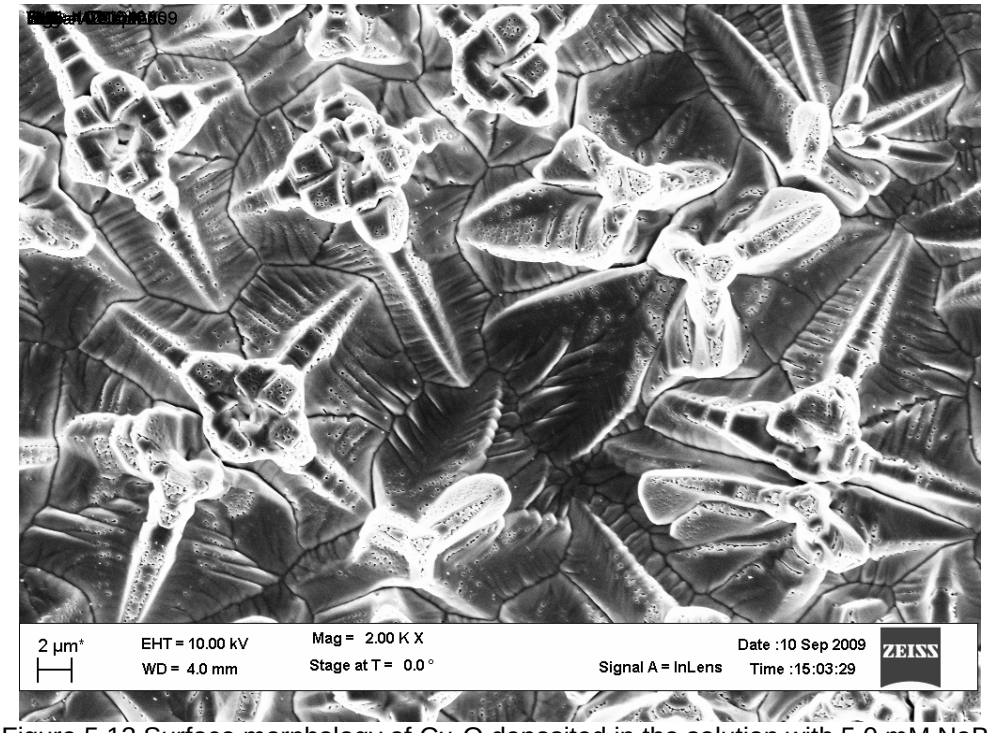

Figure 5.13 Surface morphology of Cu_2O deposited in the solution with 5.0 mM NaBr

Figure 5.14 shows the resistivity of Br-doped Cu_2O as a function of Br concentration in the solution. The solution pH and temperature were 5.2 and 60 °C, and the deposition potential was -0.1 V. It is noticed that the resistivity decreases while the Br concentration increases. This indicates that a higher Br concentration produces more free carriers in the film and leads to a lower resistivity. With 10 mM NaBr, the lowest resistivity of ~225 Ω-cm was obtained in Br doped Cu_2O.

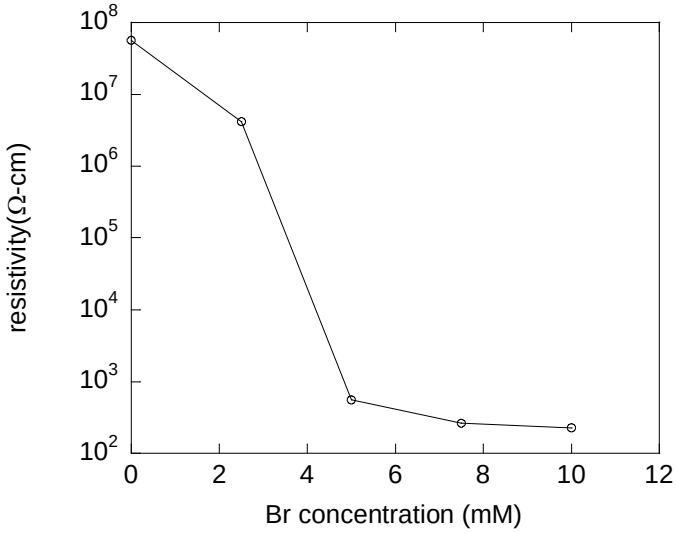

Figure 5.14 Dependency of resistivity of Br doped Cu_2O on Br- concentration in deposition solution

5.3.2.3 Solar cell fabrication with Br doped n-Cu_2O

The superstrate structure Cu_2O solar cell with Br doped n-Cu_2O was fabricated. It is thought that a rougher surface of Br doped n-Cu_2O would contribute more to the formation of the shunt path in the device. Thus, in order to have less surface roughness and a high conductivity of the n-Cu_2O film, the Br concentration of 5 mM was chosen. Thickness of Br doped n-Cu_2O was fixed to ~1um, which resulted in a roughness of ~ 0.5 um. The n-type Cu_2O films were first electrochemically deposited on ITO/glass substrate in an aqueous solution containing 0.02 M copper acetate, 0.1 M sodium acetate, and 5 mM sodium bromide at a solution of pH 5.2, a deposition potential of -0.1 V and a deposition temperature of 60 ℃. Then

3 um p-Cu_2O films were directly deposited on Br doped n-Cu_2O in an aqueous solution containing 0.4 M copper sulfate and 3 M sodium lactate at a solution of pH 13.0, a deposition potential of -0.5 V and a deposition temperature of 60 ℃. Finally, 100 nm thick Au with area of 0.282 cm^2 was deposited on the p-type Cu_2O for back contact.

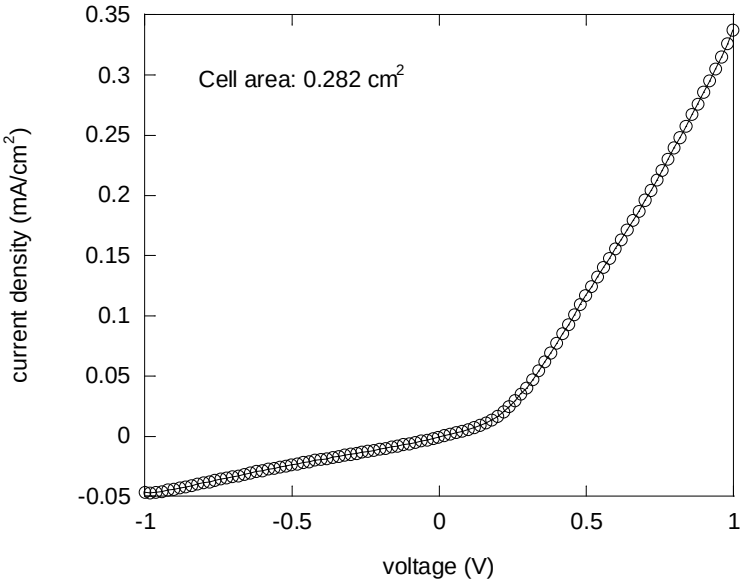

Figure 5.15 Dark I-V of superstrate Cu_2O p-n homojuncrion solar cell with Br doped n-Cu_2O

The Dark I-V characteristic of the Cu_2O superstrate solar cell with Br doped n-Cu_2O is shown in Figure 5.15. The forward current density of the cell at 1V is still below 0.5 mA/cm^2 because of the very resistive p-Cu_2O layer. The solarcell performance of superstrate Cu_2O cell is shown in Figure 5.16. Compared to the Cu_2O superstrate cell without Br doped n-Cu_2O, the overall solar cell performance was improved. Especially, I_{sc} was most improved, and the highest V_{oc} of 165 mV was obtained in the superstrate cell with Br doped n-Cu_2O. It is believed that the Br doped n-Cu_2O layer reduces bulk resistance in the device, which results in higher I_{sc} than that in the undoped Cu_2O superstrate cell.

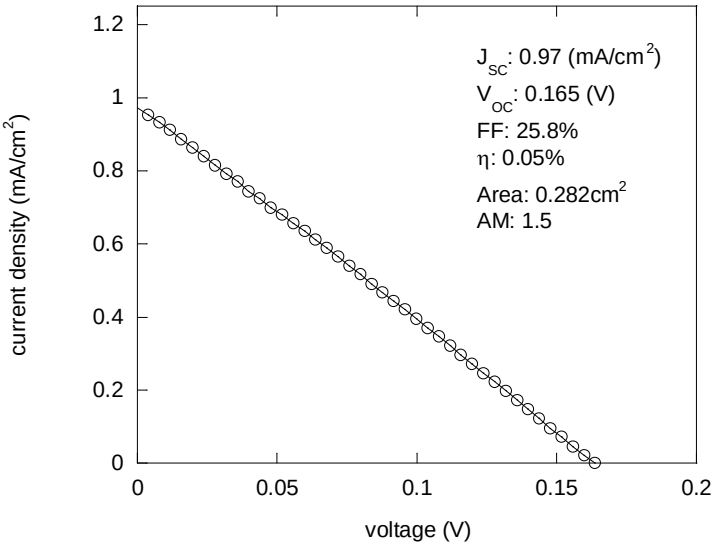

Figure 5.16 Photo I-V of superstrate Cu_2O p-n homojuncrion solar cell with Br doped n-Cu_2O

5.4 Summery

Two different n-type doping techniques, thermal diffusion doping and electro doping, were discussed, and their effects on electrical and structural properties of electrodeposited Cu_2O were investigated.

Based on the idea that the density of intrinsic point defects in Cu_2O, such as copper vacancy and oxygen vacancy, can be controlled by external Cu diffusion sources, the resistivity of Cu_2O was successfully controlled by Cu thermal diffusion temperature and duration. Scanning electron microscopy indicates that the grain size of Cu_2O is increased from 25 nm for undoped Cu_2O to 35 nm for Cu_2O annealed at 400 ℃. The resistivity of Cu_2O decreases from ~5.71×10^{8} to ~28 Ω-cm by Cu diffusion. The diffusion coefficient of Cu in Cu_2O is found to be 1.91×10^{-16} m^2/sec at annealing temperature of 325 ℃. It is spec ulated that Cu diffusion in Cu_2O takes place mainly along grain boundaries (100) at the beginning of the annealing process, and then lattice diffusion follows along the (111) planes. Photocurrent measurements verify the n-type conductivity of Cu-diffused Cu_2O, and the n-type behavior is improved as the annealing temperature increases.

Preliminary study of cation substitutional electrodoping in Cu_2O suggested that the goal of Zn-doped n-type Cu_2O may be difficult to accomplish by cathodic electrodeposition from an O_2-saturated aqueous $CuSO_4$ and $ZnSO_4$ solution due to the reduction of Cu^{2+} to Cu before OH^- generation.

However, anion substitutional electrodoping in Cu_2O was successfully demonstrated with Br ion. Br ion in the plating solution contributed to the formation of a dendritic crystal of Cu_2O and caused a reduction in the resistivity of Cu_2O to ~ 225 Ω-cm. It is believed that this doping is accomplished by co-deposition of the n-type dopant with Cu_2O.

CHAPTER 6

CONCLUSIONS AND FUTURE WORK

6.1 Conclusions

In this dissertation, electrodeposited cuprous oxide (Cu_2O) as a photovoltaic absorber material was introduced. The electrical, structural, and optical characteristics of electrodeposited Cu_2O were well investigated. With the optimized deposition parameters, electrodeposited Cu_2O p-n homojunction solar cells were fabricated, and its device characteristics were investigated. Two different n-type doping techniques were introduced in order to reduce the resistivity of the Cu_2O.

First, it was discovered that deposition conditions such as the deposition pH, potential, temperature, and solute concentration affect the electrical, structural, and optical properties of Cu_2O. Especially, the deposition pH has a significant effect in controlling the electrical and structural properties of Cu_2O. Flat band voltage of the Cu_2O increased positively as the pH of the deposition solution increased. It seems that the variation of the flat band voltage by solution pH is related to the oxygen incorporation in the film, which is controlled by the amount of the oxygen precursor, OH^-, in the solution. Hence, the high pH in the solution is more preferable in producing a p-type Cu_2O with copper vacancy, while the low pH in the solution is more preferable in producing an n-type Cu_2O with oxygen vacancy or copper interstitial. The resistivity of Cu_2O is controlled by a solution pH. As the pH of the solution increased, the resistivity of p-type Cu_2O decreased. At the pH 13.0, Cu_2O showed the lowest resistivity, which was 3.2×10^5 ohm-cm. The crystal orientation and the grain size are suggested to have significant roles in controlling the resistivity of p-type Cu_2O. At a pH above 11.0, Cu_2O with crystal orientation of (111) is obtained. It was believed that Cu_2O with (111) orientation has more intrinsic point defects, i.e., Cu vacancies that determine the carrier concentration.

Depending on the deposition condition, the band gap of Cu_2O of approximately 2.06 ~ 2.1 eV was obtained. The band gap of Cu_2O was not as sensitive as the resistivity to the deposition conditions, such as the solution pH and the deposition voltage.

Second, Cu_2O p-n homojunction solar cells with two different structures were successfully fabricated by a solution based method. The highest efficiency of 0.15 % was achieved in an electrodeposited Cu_2O substrate solar cell with size of 0.01 cm^2. The open circuit voltage of 321 mV, a short circuit current of 1.228 mA, and a fill factor of 35.33 % were obtained in the cell. The solution bath pH of n-Cu_2O controlled the open circuit voltage of the device. The Cu_2O substrate solar cell with a size of 0.4 cm^2 showed an efficiency of 0.016 % and a open circuit voltage of 107 mV. The SEM picture of the n- Cu_2O surface in the device revealed that several pin holes were formed in the n-Cu_2O layer. This contributed to the formation of shunt paths in the device, thus lowering the open circuit voltage of the solar cell. The thermal reliability test shows that the device performance of the Cu_2O solar cell is not stable above the temperature of 150 ^oC. The Cu_2O superstrate solar cell exhibited better device performance than the Cu_2O substrate cell with a size of 0.4 cm^2. The efficiency of 0.025 % was obtained from the 0.282 cm^2 size of superstrate Cu_2O solar cell, which has 3 um p-Cu_2O and 0.8 um n-Cu_2O. The efficiency of the superstrate cell was related to the thickness of the p-layer, and the superstrate cell with 3 um p-Cu_2O showed a minimal shunt effect. It was realized that the low short circuit current and the device efficiency of the Cu_2O solar cells resulted mainly from the high resistivity of both p and n-Cu_2O. Thus, doping to both the p and n-Cu_2O should be accomplished in order to have more efficient Cu_2O solar cells.

Third, two different n-type doping techniques, thermal diffusion doping and electro doping, were successfully demonstrated. The resistivity of Cu_2O was successfully controlled by Cu thermal diffusion. The lowest resistivity of 28 Ω-cm was obtained at the diffusion temperature of 400 ℃. The calculated diffusion coe fficient of Cu in Cu_2O was found to be 1.91×10^{-16} m^2/sec at the annealing temperature of 325 ℃. It is speculated that Cu diffusion in

Cu_2O takes place mainly along grain boundaries (100) at the beginning of the annealing process, and then lattice diffusion follows along the (111) planes due to its lower lattice distortion. The photocurrent experiment revealed that the Fermi energy of Cu_2O was shifted and the n type property of Cu_2O was enhanced by Cu diffusion. It is concluded that the intrinsic point defects in Cu_2O, such as copper vacancy and oxygen vacancy, were controlled by external copper diffusioin sources. N type electrodoping in Cu_2O was successfully achieved with Br ion. The deposition current increased with increasing Br concentration in the deposition solution. The increased deposition current contributed to the formation of dendritic crystals of Cu_2O. The lowest resistivity of 225 Ω-cm was obtained at the Br concentration of 10 mM in the solution. It is believed that the doping mechanism is the co-deposition of the n-type dopant with Cu_2O. The superstrate cell with Br doped n-Cu_2O showed a short circuit current of approximately 1mA. It is believed that the Br doped n-Cu_2O layer reduces bulk resistance in the device, which results in higher I_{sc} than in an undoped Cu_2O superstrate cell.

6.2 Future work

The obtained results of the Cu_2O p-n homojunction solar cell study left some questions unresolved. Several issues which were observed in Cu_2O solar cells should be investigated in order to achieve a highly efficient Cu_2O solar cell.

First, the obtained energy band gap of electrodeposited Cu2O, ~2.06 eV, is not an deal value for the photovoltaic devices. As known, a direct band gap semiconductor with a band gap of ~1.4 eV is ideal to use in the solar spectrum for maximum efficiency. It was reported that electrodeposited cupric oxide (CuO) has the band gap of ~1.5 eV [103]. One way to control the energy band gap of Cu_2O is to control the stoichiometric ratio x in Cu_XO by mixing the Cu_2O and CuO. Another way to control the energy band gap of Cu_2O is to change the lattice constant of Cu_2O by putting a different type of atom in the lattice.

Second, the resistivity of p-Cu_2O is too high to have an efficient Cu_2O p-n homojunction solar cell. Thus, the electrical properties of p-Cu_2O should be improved. The way to reduce the

resistivity of p-Cu_2O is also by doping. The suggested p-type dopants in Cu_2O are group V elements such as N and As. The resistivity of Cu_2O will be controlled if N and As can replace the anion site, O^{2-}, in Cu_2O.

Third, a different structure of solar cell with doped n-Cu_2O is suggested. With successful n type doping in Cu_2O, a high short circuit current is expected in a Schottky junction solar cell with metal / doped n-Cu_2O because of the low resistivity of n-Cu_2O. With a TCO layer on top of n-Cu_2O, the photocurrent will increase to a greater degree, since there is no shading effect due to absence of a metal grid on the illuminated surface. The selection of a metal for the junction formation is considered to be the most important factor. High work function metals, such as Ni and Pt, are considered to be candidates for the n-Cu_2O Schottky junction solar cells.

REFERENCES

1. U.S. Department of Energy, Energy Information Administration , http://www.eia.doe.gov
2. International Energy Agency (IEA), Renewables in global energy supply, IEA Press, 3-11 (2007)
3. U.S. Department of Energy, Energy Information Administration (EIA), International energy outlook, 7-20 (2009)
4. Intergovernmental Panel on Climate Change (IPCC), The Fourth Assessment Report-Climate Change 2007, http://www.ipcc.ch
5. Nathan S. Lewis, http://nsl.caltech.edu/energy.ppt
6. U.S. Department of Energy, Basic Research needs for solar energy utilization, (2005)
7. Paul D. Maycock, Refocus, **6**, 18 (2005)
8. http://www.solarbuzz.com
9. M. Tao, The Electrochem. Soc. Interface, **17**, #4, 30 (2008)
10. S. M. Sze, Physics of Semiconductor Devices. 2nd ed. New York: Wiley (1981)
11. A. Goetzberger, C. Hebling, H. W. Schock, Mater. Sci. and Eng., R, **40**, 1 (2003)
12. L.C. Olsen, R.C. Bohara and M.W. Urie, Appl. Phys. Lett., **34**, 47 (1979)
13. J. Herion, E.A. Niekisch and G. Scharl, Sol. Energy Mater., **4**, 101, (1980)
14. L. Papadimitriou, N.A. Economou and D. Trivich, Sol. Cells, **3**, 73 (1981)
15. J. Katayama, K. Ito, M. Matsuoka and J. Tamaki, J. Appl. Electrochem., **34**, 687 (2004)
16. A. Mittiga, E. Salza, F. Sarto, M. Tucci and R. Vasanthi, Appl. Phys. Lett., **88**, 163502 (2006)
17. C.H. Henry, J. Appl. Phys., **51**, 4494 (1980)
18. L.C. Olsen, F.W. Addis and W. Miller, Sol. Cells, **7**, 247 (1982)
19. A. E. Becquerel, Comptes Rendus, **9**, 561 (1839)

20. C. E. Fritts, Proc. Am. Assoc. Adv. Sci., **33**, 97 (1983)
21. L. O. Grondahl, Rev. Mod. Phys., **5**,141 (1933)
22. D. Chapin, C. Fuller, and G. pearson, J. Appl. Phys., **25**, 676 (1954)
23. M. P. Thekaekara, Suppl. Proc. 20th Annu. Meet. Inst. Environ. Sci., 21 (1974)
24. D. Bouhafs, A. Moussi, A. Chikouche, and J. M. Ruiz, Sol. Energy Mater. Sol. Cells, **52**, 79 (1998)
25. J. Haynos, J. Allison, R. Arndt, and A. Meulenberg, Int. Conf. on Photovoltaic Power Generation, 487 (1974)
26. J. E. Cotter, R. B. Hall, M. G. Mauk, and A. M. Barnett, Progr. Photovoltaics, **7**, 261 (1999)
27. M. F. Lamorte, and D. Abbott, Solid State Electron., **22**, 467 (1979)
28. A. J. Nozik, C. A. Parsons, D. J. Dunlary, B. M. Keyes, and R.K. Ahrenkiel, Solid State Commun., **75**, 297 (1990)
29. A. Luque, and A. Marti, Phys. Rev. Lett., 78, 5014 (1997)
30. A. W. Blakers, and M. A. Green, Appl, Phys. Lett., **48**, 215 (1986)
31. M. P. R. Panicker, M. Knaster and F.A. Krfger, J. Electrochem. Soc., **125**, 566 (1978)
32. C. Sella, P. Boncorps and J. Vedel, J. Electrochem. Soc., **133**, 2043 (1986)
33. A. Saraby-Reintjes, L. M. Peter, M. E. Ozsan, S. Dennison and S. Webster, J. Electrochem. Soc., **140**, 2880 (1993)
34. D. Lincot, A. Kampmann, B. Mokili, J. Vedel, R. Cortes and M. Froment, Appl. Phys. Lett., **67**, 2355 (1995)
35. R. N. Bhattacharya, J. Electrochem. Soc., **130**, 2040 (1983)
36. R. N. Bhattacharya and K. Rajeshwar, Solar cells, **16**, 237 (1986)
37. J. F. Guillemoles, P. Cowache, A. Lusson, K. Fezzaa, F. Boisivon, J. Vedel and D. Lincot, J. Appl. Phys., **79**, 7293 (1996)
38. Izaki, M.; Omi, T. *J. Electrochem. Soc*., **143**, L53 (1996)

39. Peulon, S.; Lincot, D. *Adv. Mater*., **8**, 166 (1996)
40. Yao, J. N.; Chen, P.; Fujishima, A. *J. Electroanal. Chem*., **406**, 223 (1996)
41. Meulenkamp, E. A. *J. Electrochem. Soc*., **144**, 1664 (1997)
42. Baesa, R. R.; Rutsch, G.; Dougherty, J. P. *J. Mater. Res*., **11**, 194 (1996)
43. A. J. Bard, and L. R. Faulkner, Electrochemical methods Fundamentals and Applications. 2nd ed. Wiley (2001)
44. H. F. Wolf, Semiconductors, Wiley, New York (1971)
45. W. Schottky and F. Waibel, Phys. Z., **36**, 912 (1935)
46. H. Dünwald and C. Wagner, Z. Phys. Chem. **B14**, 467 (1932)
47. C. Wagner and K. Grünewald, Z. Phys. Chem. **B40**,455 (1938)
48. M. O'Keeffe and W. J. Moore, J. Chem. Phys., **36**, 3009 (1962)
49. R. S. Toth, R. Kilkson, and D. Trivich, J. Appl. Phys., **31**,1117 (1960)
50. H. L. Mckinzie and M. O'Keeffe, Phys. Lett., **24A**, 137 (1967)
51. A. P. Young and C. M. Schwartz, J. Phys. Chem. Solids, **30**, 249 (1969)
52. R. Kuzel and F. L. Weichman, J. Appl. Phys., **41**, 271 (1970)
53. A.E. Rakhshani, Solid-State Electron., **29**, 7 (1986)
54. F. L. Weichman, Phys. Rev., **117**, 998 (1960)
55. A. Roos and B. Karlsson, Sol. Energy Mater., **7**, 467 (1983)
56. A. A. Berezin and F. L. Weichman, Solid State Commun., **37**, 157 (1981)
57. M. T. S. Nair, L. Guerrero, O. L. Arenas and P. K. Nair, Appl. Surf. Sci., **150**, 143 (1999)
58. T. Mahalingam, J. S. P. Chitra, S. Rajendran, M. Jayachandran and M. J. Chockalingam, J. Cryst. Growth, **216**, 304 (2000)
59. B. balamurugan and B. R. Mehta, Thin Solid Films, **396**, 90 (2001)
60. A. E. Rakhshani, Y. Makdisi, and X. Mathew, J. Mater. Sci. Mater. in Electronics, **8**, 207 (1997)
61. J. Xue and R. Dieckmann, J. Phys. Chem. Solids, **51**, 1263 (1990)

62. G. P. Pollack and D. Trivich, J. Appl. Phys., **46**, 163 (1975)
63. T. Ito, H. Yamaguchi, K. Okabe and T. Masumi, J. Mater. Sci., **33**, 3555 (1998)
64. D. Tench and L. F. Warren, *J. Electrochem. Soc.*, **130**, 869 (1983)
65. V. F. Drobny and D. L. Pulfrey, Thin Solid Films, **61**, 89-98 (1979)
66. A. E. Rakhshani, A. A. Al-Jassar, and J. Varghese, Thin Solid Films, **148**, 191 (1987)
67. A. E. Rakhshani and J. Varghese, Thin Solid Films, **157**, 87 (1988)
68. A. E. Rakhshani and J. Varchese, J. Mater. Sci., **23**, 3847 (1988)
69. Y. Zhou and J. A. Switzer, Scripta Mater., **38**, 1731 (1998)
70. T. D. Golden, M. G. Shumsky, Y. Zhou, R. A. VanderWerf, R. A. Van Leeuwen and J. A. Switzer, Chem. Mater., **8**, 2499 (1996)
71. Y. Zhou and J. A. Switzer, Mat. Res. Innovat., **2**, 22 (1998)
72. R. P. Wijesundera, M. Hidaka, K. Koga, M. Sakai and W. Siripala, Thin Solid Films, **500**, 241 (2006)
73. T. Mahalingam, J. S. P. Chitra, S. Rajendran, and P. J. Sebastian, Semicond. Sci. Technol., **17**, 565 (2002)
74. W. H. Brattain, Rev. Mod. Pys, **23**, 203 (1951)
75. W. Siripala and J. R. P. Jayakody, Sol. Energy Mater., **14**, 23 (1986)
76. L. C. Wang, N. R. de Tacconi, C. R. Chenthamarakshan, K. Rajechwar, M. Tao, Thin Solid Films, **515**, 3090 (2007)
77. L. C. Wang, M. Tao, Electrochem. Solid-State Lett., **10**, H248 (2007)
78. L. F. Lou, W. H. Frye, J. Appl. Phys., **56**, 2253 (1984)
79. K. Mizuno, M. Izaki, K. Murase, T. Shinagawa, M. Chigane, M, Inaba, A. Tasaka, and Y. Awakura, J. Electrochem. Soc., **152**, C179 (2005)
80. R. H. Bube, Photoelectronic properties of semiconductor, Cambridge (1992)
81. M. Fox, Optical properties of solids, Oxford (2003)
82. R. H. Bube, K. W. Mitchell, J. Electron. Mater., **22**, 12 (1993)

83. I. Hamberg, C. G. Granqvist, J. Appl. Phys., **60**, R123 (1986)
84. W. A. Badway, H. H. Afifiand, and E. M. Elgair, J. Electrochem. Soc., **137**, 1592 (1990)
85. K. L. Chopre, S. Major, and D. K. Pandya, Thin Solid Films, **102**, 1 (1983)
86. J. C. Manifacier, Thin Solid Films, **90** (1982) 297
87. S. Takaki, K. Matsumoto, and K. Suzuki, Appl. Surf. Sci., **33**, 919 (1988)
88. G. Frank, and H. Kostlin, Appl. Phys., **A27**, 197 (1982)
89. T. Maruyama, and T. Kitamura, Jpn. J. Appl. Phys., **28**, 1096 (1989)
90. H. Dislich, J. Non-Cryst. Solids, **57**, 371 (1988)
91. W. H. Bloss, F. Pfisterer, M. Schubert, and T. Walter, Progress in Photovoltaics, **3**, 3 (1995)
92. S. Ishizuka, S. Kato, T. Maruyama, and K. Akimoto, Jap. J. Appl. Phys., **40**, 2765 (2001)
93. A.O. Musa, T. Akomolafe and M.J. Carter, Sol. Energy Mater. Sol. Cells, **51**, 305 (1998)
94. X. Han, K. Han and M. Tao, Electrochem. Solid-State Lett., **12**, H89 (2009)
95. W. Siripala, L. D. R. D. Perera, K. T. L. de Silva, J. K. D. S. Jayanetti and I. M. Dharmadasa, Sol. Energy Mater. Sol. Cells, **44**, 251 (1996)
96. P. Shewmon, Diffusion in Solids, TMS (1989)
97. J. Crank, The Mathematics of Diffusion, Oxford (1975)
98. M.L. Narula, V.B. Tare and W.L. Worrell, Metal. Trans. B, **14**, 673 (1983)
99. P. E. de Jongh, D. Vanmaekelbergh and J. J. Kelly, J. Electrochem. Soc., **147**, 486 (2000)
100. D. R. Lide, in Handbook of Chemistry and Physics 84th Ed., CRC Press (2004)
101. R. M. Brandy and R. C. Ball, Nature, **309***,* 225 (1984)
102. C. M. Lopez and K. S. Choi, Langmuir, **22**, 10625 (2006)
103. K. Santra, C. K. Sarkar, M. K. Mukherjee and B. Ghosh, Thin Solid Films, **213**, 226 (1992)

BIOGRAPHICAL INFORMATION

Kunhee Han was born in Seoul, South Korea. He received a B.S degree from the electronic engineering department of Sejong University, Seoul, South Korea in 2002. He began his graduate study at the University of Texas at Arlington, USA, in 2003. He joined the Giga-Nano Semiconductors group as a graduate research assistant under the guidance of Dr. Meng Tao in 2004 and he obtained a M.S in 2006. In the same year he began his pursuit of a Ph.D. degree, which he earned from the University of Texas at Arlington, USA in 2009. His research interests include solution based metal oxide deposition, electrochemical doping in semiconductors and solar cell fabrication by the wet chemical method.